

Universiteit
Leiden
The Netherlands

The sky is made of lava: how lava worlds reveal their interiors through their atmospheres

Buchem, C.P.A. van

Citation

Buchem, C. P. A. van. (2025, September 5). *The sky is made of lava: how lava worlds reveal their interiors through their atmospheres*. Retrieved from https://hdl.handle.net/1887/4259796

Version:	Publisher's Version
License:	Licence agreement concerning inclusion of doctoral thesis in the Institutional Repository of the University of Leiden
Downloaded from:	https://hdl.handle.net/1887/4259796

Note: To cite this publication please use the final published version (if applicable).

The Sky is Made of Lava

How lava worlds reveal their interiors through their atmospheres

Proefschrift

ter verkrijging van
de graad van doctor aan de Universiteit Leiden
op gezag van rector magnificus prof.dr.ir. H. Bijl,
volgens besluit van het college voor promoties
te verdedigen op vrijdag 5 september 2025
klokke 11:30
door

Christiaan Pieter Augustijn van Buchem

geboren te Parijs, Frankrijk
in 1995

Promotores:	Prof.dr. I.A.G. Snellen	
	Prof.dr. W. van Westrenen	Vrije Universiteit Amsterdam
Copromotor:		
	Dr. Y. Miguel	
Promotiecommissie:		
	Prof.dr. A. Vidotto	
	Prof.dr. E. F. van Dishoeck	
	Prof.dr. M. Hogerheijde	
	Dr. T. Lichtenberg	Rijksuniversiteit Groningen
	Dr. M. Min	Netherlands Institute for Space Research

ISBN: 978-94-6473-883-4

Cover: Reinier Cedric van Buchem

Printed by: Proefschriften.nl

"La seule chose que nous ayons à craindre,
c'est que le ciel nous tombe sur la tête!"

"The only thing we have to fear
is that the sky will fall on our heads!"

– *Asterix et Obelix*, René Goscinny

Contents

1 Introduction **1**
- 1.1 Hell on (super-) Earth . . . 1
- 1.2 Why do we care? . . . 4
  - 1.2.1 (exo)Planets . . . 4
  - 1.2.2 Lava Planets . . . 7
- 1.3 How did we do it? . . . 9
  - 1.3.1 Observing hot-rocky exoplanets . . . 9
  - 1.3.2 Modelling hot-rocky exoplanets . . . 13
- 1.4 What did we find? . . . 17

2 LavAtmos: An open-source chemical equilibrium vaporization code for lava worlds **23**
- 2.1 Introduction . . . 24
- 2.2 Methodology . . . 26
- 2.3 Validation . . . 31
- 2.4 Discussion . . . 39
- 2.5 Conclusion . . . 41
- Appendices . . . 42
- 2.A Deriving the partial pressure equation . . . 42

3 Sensitivity of Dry Lava Planet Atmospheric Emission Spectra to Changes in Lava Compositions **45**
- 3.1 Introduction . . . 46
- 3.2 Method . . . 47
  - 3.2.1 Melt compositions . . . 48
  - 3.2.2 Equilibrium chemistry . . . 50
  - 3.2.3 Star-planet systems . . . 52
  - 3.2.4 Radiative transfer . . . 53
  - 3.2.5 Pseudo-2D model . . . 55
- 3.3 Results . . . 55
  - 3.3.1 The anatomy of a BSE vapour atmosphere . . . 57
  - 3.3.2 TiO_2 variation . . . 58
  - 3.3.3 SiO_2 variation . . . 62
  - 3.3.4 Alkali variation . . . 65
  - 3.3.5 Observability of potential targets . . . 69
- 3.4 Discussion . . . 71
  - 3.4.1 Melt compositions . . . 71
  - 3.4.2 Assumptions made in our model . . . 71
  - 3.4.3 Surface temperature degeneracy . . . 73
- 3.5 Conclusion . . . 73
- Appendices . . . 75
- 3.A Melt compositions . . . 75

3.B Opacity data . . . 77
3.C Stellar spectra . . . 77
3.D Pseudo-2D atmosphere . . . 77
3.E SiO_2 activity changing with alkali abundances . . . 77

4 LavAtmos 2.0: Incorporating volatile species in vaporisation models 83
4.1 Introduction . . . 84
4.2 Methods . . . 87
4.2.1 Workflow . . . 87
4.2.2 Model validation . . . 89
4.3 Results . . . 90
4.3.1 Effect of pure volatile atmospheres . . . 90
4.3.2 Effects of a complex volatile atmosphere . . . 96
4.4 Implications for a 55-Cnc e-like atmosphere . . . 97
4.4.1 Vaporised partial pressure comparison between LavAtmos 2.0 and the volatile-free vaporisation method . . . 102
4.4.2 The effect of lava oceans on atmospheric volatile species 105
4.5 Discussion . . . 108
4.5.1 Effect of water on melt activities . . . 108
4.5.2 Water in melt as a source of oxygen . . . 110
4.5.3 How to identify a surface lava ocean from atmospheric composition . . . 110
4.6 Conclusion . . . 111
Appendices . . . 112
4.A Effect of complex volatile atmospheres on vaporised species . . . 112

5 The effect of H^- continuum on Lava Planet Emission Spectra 119
5.1 Introduction . . . 120
5.2 Methods . . . 121
5.2.1 Forward model . . . 121
5.2.2 H^- opacity . . . 122
5.3 Results . . . 123
5.3.1 Adding H to a lava planet atmosphere . . . 128
5.3.2 Sensitivity to temperature . . . 131
5.4 Discussion . . . 134
5.5 Conclusion . . . 135
Appendices . . . 136
5.A Opacities . . . 136

English summary 151

Nederlandse samenvatting 155

Publications 159

Curriculum Vitae **161**

Acknowledgements **163**

1 Introduction

1.1 Hell on (super-) Earth

You are a photon. A light particle released from the core of a star during the nuclear fusion of two hydrogen atoms forming a helium atom. You have spent the last one hundred thousand years[1] bouncing your way around the tightly packed interior of the star, slowly making your way towards the surface. A hundred thousand years to cover seven hundred thousand kilometres. Suddenly, you are free. Out into space. Moving at an unimaginable speed - the speed of light in a vacuum. The next seven hundred thousand kilometres take you a bit more than two seconds to cover.

Unlike the large majority of your fellow photons, however, your freedom is short-lived. Just under eight seconds after your escape from the surface of the star from which you were born, you reach a hellish place. As you approach what at first appears to be nothing more than a tiny glowing rock in the distance, quickly reveals itself to be a dramatic world.

Your progenitor, the star, is shining down unbiddingly from behind you upon the eternal day-side of this planet, appearing sixty times larger in the sky than the sun does on earth (see Figure 1.1). This has turned the entire dayside of the planet into a huge, churning, and bubbling ocean of lava. The centre of this ocean is so hot that even the heaviest of elements melt. Enormous amounts of vaporized rock and metal are carried up into the atmosphere and blown outward toward the planet's night side by super-sonic winds. As the star drops towards the horizon and you near the night side, clouds start to form. Clouds of molten glass that rain down onto cliffs made of metal.

Suddenly, you bounce off of a silicon monoxide molecule that is floating in the atmosphere of the planet. Before you know it, you are leaving the inferno behind you. You skim the surface of the star to say goodbye one final time, and then you are truly on your way. Free, out into interstellar space.

Forty years later, you notice that a star, very similar to the one you were born in, is growing in size. You also notice a tiny blue speck appearing next to it. Growing ever larger, but right as you think you might hit it, you suddenly bounce off of a golden mirror instead, into a dizzying network of countless other tiny mirrors, until you reach your final resting place in one of the charge-coupled detectors of the James Webb Space Telescope. Do not worry though, your legacy does not end here.

The energy that you release as you are absorbed by the charged-coupled detector is turned into an electric current. This current is used to magnetically charge a tiny component of a solid-state drive. About twenty-four hours later,

[1] Although technically everything happens simultaneously from the perspective of a photon, let's say that you understand the passing of time.



Figure 1.1: Apparent size comparison of the Sun and 55 Cnc A: As seen from Earth and 55 Cnc e respectively. 55 Cnc A appears about sixty times larger in the sky of 55 Cnc e than the Sun appears on Earth. The left side image was taken by the author. The right side image is composed of an image of the sun (taken by instagram.com/cosmic_background/) and an image generated using ChatGPT by OpenAI.

this magnetic charge is read out and emitted as a radio signal. The radio photon takes five seconds to travel to the nearby blueish planet. There, on its surface, it is caught by a large antenna.

Finally, after months of being sent around, copied, merged, and sent around again across a network of fibre optical cables spanning the entire planet, the evidence of your existence as a photon enters a worn down laptop on ten percent charge. After all this, the fact of your existence and the journey that you have made caused a chain of events that is now telling a few of the pixels on an LCD screen to emit less light than the neighbouring pixels (making it appear black). Photons emitted from this screen reach the eyes of a highly caffeinated bipedal primate - whose digestive system is sending signals that a far greater range of nutrients are required than the "boterham" with peanut butter and bean juice that have been offered to it in the past twenty four hours.

“There is no way that this data is real, this doesn’t look anything like my models!”

You did your best. Maybe one of the other quadrillions of photons that have made the same journey as you will manage to convince this hangry monkey of your existence.

Much of modern (exoplanet) astronomy relies on maximizing the amount of information that we can draw from a single point of unresolved light. As the (somewhat dramatized) story above aims to illustrate, a great number of different things happen to a photon before it reaches the Earth, and once it has, a great many steps must be taken to draw information from it. In order to be able to appropriately interpret this information, we must understand the journey which the photon has taken and the subsequent steps taken to analyse the information from this photon as best as we can.

This is achieved by making models. Broadly speaking, astronomers that work on theoretical modelling focus on the physical and chemical processes that influence the photons before reaching a telescope. Astronomers that are more oriented towards observations model the physical processes that influence photons once they have reached the telescope and pass through all the detection instruments. In short, you could say that one focuses on what you "should" see (according to models of astronomical objects) and the other focuses on what you "do" see (according to models of telescopes and their constituent parts). It is at the conjunction of these two disciplines[2] that we try and decipher the truth behind what is out there in the universe. The work presented in this

[2]It should be noted here that none of this would be possible without the monumental amount of work done by astronomers, physicists, and engineers to ensure that working telescopes exist in the first place.

thesis starts off from a theoretical basis and then attempts to build a bridge towards what we could potentially observe.

We apply this to the niche field of hot rocky exoplanets, which are planets so close to their host star that they have a molten surface - as illustrated in the opening of this chapter and shown in Figure 1.1. Through the modelling done for this work, we try to answer one question:

"What do lava planet atmospheres tell us about their interiors?"

This introduction serves to give context as to why this is a relevant question and to provide the knowledge necessary to understand the work done in the following chapters. We end this chapter with a broad overview of the main conclusions that we draw from the work presented in this thesis.

1.2 Why do we care?

1.2.1 (exo)Planets

If you dig down to the core of astronomical research, most of it boils down to some variation of the following questions: "Why do we exist?" and "Are we alone?". Within the niche of (exo)planet astronomy, these questions lead us to ask: "How did the Earth form?" and "Are there other planets like it?". For the majority of the history of modern astronomy, the solar system bodies were the only (non-stellar) worlds besides Earth that we could observe. At first glance, this may not seem problematic. We have a large moon in our backyard, three nearby rocky planets, further out we have four gas giants with plenty of large moons, and if studying those would not suffice, we could visit the huge number of other tiny planetoids orbiting the Sun. In the grand scheme of the universe, however, this is a trivially small sample size that leaves many questions unanswered. Do planets outside the solar system exist? If so, are they similar to the planets we have here? What about their size and distance from their host stars? Are they made of similar material? Could they support life? And so on. It wasn't until a bit over 30 years ago that we could start answering some of these questions.

In 1992, Wolszczan & Frail (1992) discovered two planets orbiting the Pulsar PSR B1257+12. Their discovery was confirmed two years later along with the discovery of a third planet in the same system (Wolszczan 1994). The exact timing of the pulses coming from this millisecond radio pulsar could only be explained with the presence of these planets. However, these systems are thought to be quite rare. At the time of writing of this thesis, only eight confirmed exoplanet detections were made through pulsar timing variations[3]. Furthermore, besides their mass, it is hard to derive any other properties of these planets

[3] exoplanetarchive.ipac.caltech.edu

using this observational technique. Hence, the discovery of the first exoplanet around a main-sequence star by Mayor & Queloz (1995) is generally considered to be the true starting shot of the era of exoplanets.

By measuring variations in the radial velocity of the sun-like star 51-Peg, Mayor & Queloz (1995) were able to derive the existence of a Jupiter-mass planet: 51-Peg b. This immediately conflicted with the classical view of planetary systems that existed based on our solar system. A Jupiter sized planet was located at a distance from its star smaller than the distance from Mercury to the Sun. This was only the start. In the three decades that followed, the number of discovered exoplanets grew exponentially, especially with the advent of dedicated exoplanet space-telescopes such as Kepler and the Transiting Exoplanet Survey Satellite (TESS) (see top panel in Figure 1.2). As of the 28th of November 2024, 5788 exoplanets have been discovered[4]. A number which will continue to increase in the foreseeable future, especially with new dedicated space missions that are already online or soon will be such as Plato, Ariel, and Cheops, the promise of exoplanet discoveries in Gaia data (Panahi et al. 2022), and a long list of ongoing and planned ground-based observing programs (e.g. CARMENES, HARPS, WASP, and TRAPPIST).

As of today, one thing has become clear: the diversity of star-planet system configurations is enormous. The bottom panel of Figure 1.2 illustrates the broad range of masses and orbital periods for all confirmed planet discoveries to date. Only a small fraction of these planets have masses and orbital periods comparable to those of the planets in our solar system (marked in purple). This is because planets are easier to detect when they are closer to their host star and have greater mass. As a result, there is a strong observational bias favouring larger, close-in planets.

If most planetary systems were analogous to our solar system - with smaller rocky planets near the star and larger gas giants farther out - we would expect to detect mostly smaller rocky planets close to their star. Instead, there is a dizzying array of different systems, sometimes referred to as the "exoplanet zoo" (Naeye 2017). Rather than conforming to the traditional binary classification of rocky planets and gas giants, many planets fall into intermediate categories, such as super-Earths and mini-Neptunes (Bean et al. 2021).

As was clear early on, thanks to 51-Peg b, gas giants are not confined to the outer parts of planetary systems. These ‘hot Jupiters’ - broadly defined as gas giants with an orbital period of less than 10 days - have become some of the most well-studied objects in exoplanet astronomy (Dawson & Johnson 2018). Beyond that, we’ve uncovered planets with highly eccentric orbits, planets around binary- (Armstrong et al. 2014) and triple-star systems (Busetti et al. 2018), and even planets orbiting stellar remains such as neutron stars (as we saw above) and white dwarfs (Vanderburg et al. 2020; Blackman et al. 2021; Mullally et al. 2024).

These discoveries make one thing increasingly apparent: planets are ubiq-

[4] https://exoplanetarchive.ipac.caltech.edu/

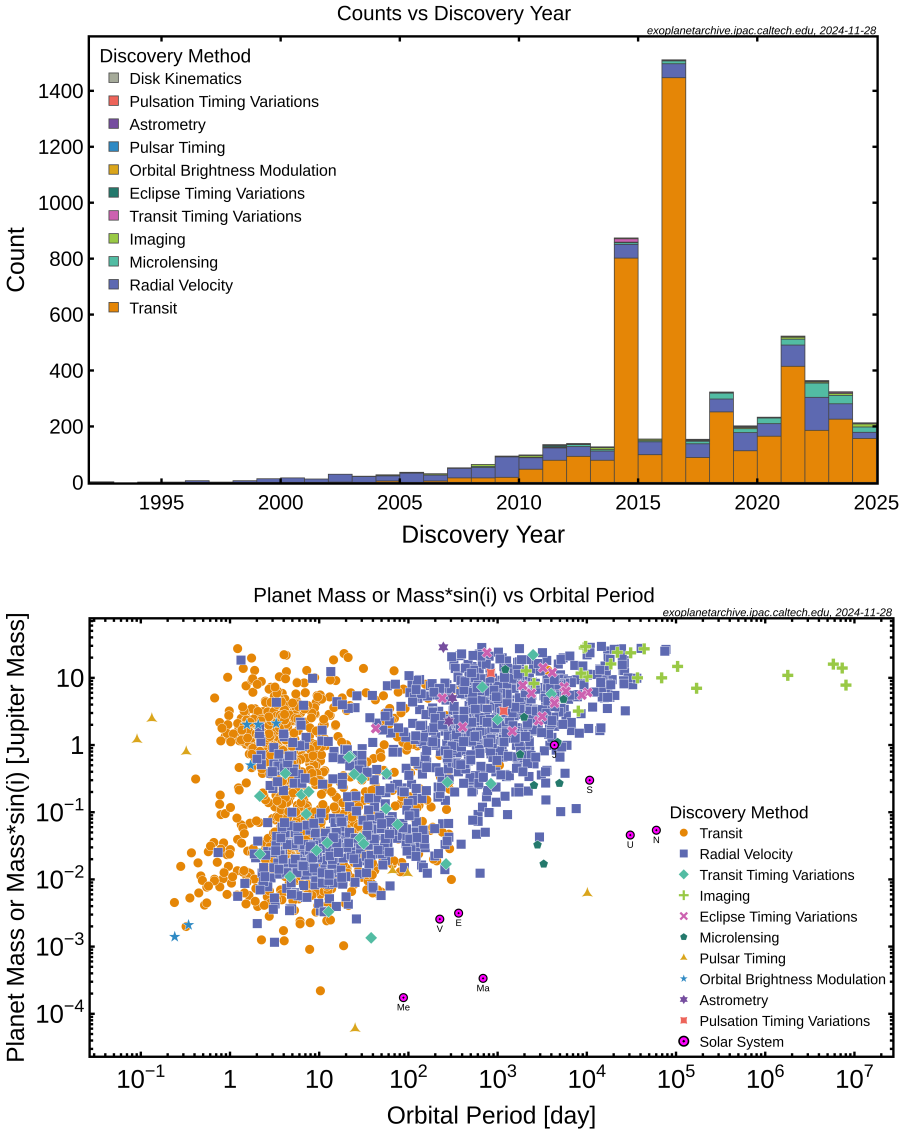


Figure 1.2: Exoplanet archive statistics as of 28th of November 2024: The top panel shows the discovered planet count per year since the first discovery in 1992. The bottom panel plots all discovered exoplanets as a function of mass and orbital period. Figures were made using the pre-generated exoplanet plots available on: exoplanetarchive.ipac.caltech.edu/exoplanetplots/

uitous. As detection methods become more sophisticated, pushing the limits of detection out to longer periods and down to smaller masses, the diversity of planetary systems will likely continue to expand, revealing even more of the remarkable variety in the universe.

What exoplanets lack in resolution and possibilities for in situ measurements, they make up for in sheer numbers. As mentioned earlier, we are already up to 5788 confirmed exoplanet detections, enabling the first statistical studies of their properties. One of the more straightforward properties to derive with current detection methods is planet mass, which has been the focus of early studies on occurrence rates (e.g. Wittenmyer et al. 2011a,b). By combining mass and orbital distance as selection criteria, studies have been able to look at the frequency of hot Jupiters (Wright et al. 2012) and the likelihood of finding Earth-like rocky planets in the habitable zone of their star (Dressing & Charbonneau 2015; Bryson et al. 2021).

As the catalogue of discovered exoplanets grows and our knowledge of their properties becomes increasingly detailed, the scope of statistical studies continues to expand. For example, the ongoing ESO SupJup Survey (Regt et al. 2024; Picos et al. 2024; Zhang et al. 2024a; Gandhi et al. 2025) leverages recent advancements in high-resolution spectroscopic instrumentation, such as CRIRES$^+$, to measure $^{12}C/^{13}C$ isotope ratios in super-Jupiters. These measurements provide new insights into the formation pathways that can lead to the birth of this class of giant exoplanets.

Among the many unanswered questions in exoplanet science is the bulk composition of rocky planets. These planets are both harder to detect than gas giants and, due to them having a surface, have atmospheres that may or may not be connected to their interior compositions. This makes it challenging to infer their bulk compositions from the composition of their atmospheres. However, there is one type of rocky planet that might hold the key to unravelling this mystery.

1.2.2 Lava Planets

'Hot rocky exoplanets' (HREs), interchangeably called 'lava planets', are rocky planets (typically defined as having a radius $\lesssim 2R_\oplus$), that orbit their host star at such a short distance that their day-side surface temperature reaches beyond the melting point of rock ($\gtrsim$ 1500 K). Due to the proximity to their host-star, these planets experience strong tidal forces leading to a decrease in their rotation speed down to the point that they become tidally locked. This means that the time it takes for a planet to rotate about itself once is equal to the orbital period of the planet around the star (analogous to the Moon with respect to Earth), effectively creating a permanent day and night side (Barnes 2017; Pierrehumbert & Hammond 2019). Due to this and the extremely high surface temperatures, it is likely that HREs support large lava oceans on their daysides (e.g. Miguel et al. 2011; Demory et al. 2011; Kite et al. 2016). If

these planets are able to support a volatile atmosphere or some other effective medium through which to transport heat over to the night-side, they might even be able to support global lava oceans (Zilinskas et al. 2023; Meier et al. 2023).

Observing these planets offers several significant advantages compared to their more distant and colder rocky counterparts. First, they are easier to detect and study. Their short orbital radii result in extremely short orbital periods, sometimes just a few hours. The most extreme example currently known is K2-137 b with an orbital period of only 4.3 hours (Smith et al. 2018). Such short periods greatly increase the likelihood of observing a planet during a transit (when it passes in front of its host star from Earth's perspective) or an eclipse (when it passes behind the star). Additionally, the high surface temperature of these close-in planets results in stronger infrared emission compared to colder planets. This increased emission leads to a more pronounced dip in the system's apparent brightness during eclipses (more on this later).

Another unique advantage of HREs is that their lava oceans may provide a direct interface between the interior and atmosphere of these planets (Léger et al. 2009; Henning et al. 2018; Boukaré et al. 2022). The temperature and chemical composition of the surface lava determine the composition of the vapour released into the atmosphere (Fegley & Cameron 1987; Schaefer & Fegley Jr. 2004; van Buchem et al. 2023; Wolf et al. 2023; Seidler et al. 2024). This rock vapour, in turn, fully or partially governs the atmospheric composition, depending on the abundance of atmospheric volatile elements (such as hydrogen). The composition of the surface lava is likely closely related to the composition of the planet's mantle (Kite et al. 2016; Boukaré et al. 2023; Lichtenberg & Miguel 2024). As a result, analysing the chemical makeup of an HRE's atmosphere could provide valuable insights into the planet's interior composition, information that is difficult to obtain even for solar system planets.

Gaining a novel approach to derive rocky-planet interior compositions, even if limited to a specific population type, would see a wide range of applications. To name but a few, it could help break the degeneracy currently faced when deriving interior compositions based on the mass and radius of a planet (Rogers & Seager 2010), provide insight into the relation between the composition of rocky planets and that of their host star (Bond et al. 2010; Dorn et al. 2017; Putirka & Rarick 2019; Wang et al. 2019; Putirka et al. 2021), and help constrain how differentiation within the interior of rocky planets affects the composition of the crust and mantle (Dyck et al. 2021). Furthermore, there is mounting evidence that most, if not all, rocky bodies such as planetoids, moons, and rocky planets had a lava ocean phase at some point in their evolutionary history (Greenwood et al. 2005; Elkins-Tanton 2012; Hin et al. 2017; Norris & Wood 2017; Schaefer & Elkins-Tanton 2018). Being able to constrain the composition of atmospheric products of a lava ocean may therefore also inform us about what the atmosphere of early Earth may have looked like.

Until recently, the study of HRE atmospheres was mostly confined to the

realm of theory. Observational data were limited, with the best results coming from the Spitzer Space Telescope observations of 55-Cnc e[5] (Demory et al. 2016a,b) and K2-141 b (Zieba et al. 2022). However, Spitzer was not specifically designed for the observation of exoplanets, and reducing the data for these objects was notoriously difficult. This has now changed with the advent of JWST.

In the past year, Hu et al. (2024) have found signs pointing toward 55-Cnc e hosting a volatile atmosphere, potentially containing CO. In addition to this work, many currently ongoing studies are working on extracting chemical compositions from HRE atmospheres using JWST data. Although many uncertainties and degeneracies remain, JWST is now bringing us tantalizingly close to being able to characterize the chemistry of HREs. As reduction techniques improve (thanks to a growing understanding of JWST's instruments), as new observations accumulate, and as new telescopes such as Ariel, the Habitable World Observatory, and the Extremely Large Telescope (ELT) join the ranks, it is likely that we can start characterizing the atmospheric composition of these planets in the near future.

To interpret these observations and make progress towards deriving interior compositions from atmospheric data, comprehensive and self-consistent models are essential. In the following section of this introduction, we provide the necessary context for understanding our approach to this challenge.

1.3 How did we do it?

Having gained a better understanding of *why* we are interested in modelling and observing HREs, we will now take a look at *how* HREs are modelled and observed. Although the work presented in this thesis is mainly focussed on the modelling of HREs, we start by explaining how HREs are observed so as to have a clear idea of what model spectra aim to replicate. We then give an overview of the modelling approach that we took.

1.3.1 Observing hot-rocky exoplanets

The majority of star-planet systems are too small to be able to spatially resolve with current telescope resolution, especially if one is observing close in exoplanets such as HREs. Therefore, to observe the flux being emitted from an exoplanet one needs to make use of the geometry of star planet systems.

When observing a star that hosts a planet which is aligned with our line of sight as seen from Earth, the planet appears to pass in front of and behind the star as it moves through its orbit (as illustrated in Figure 1.3). When a planet passes in front of the star, it is called a transit, and when it passes behind the star, it is called an eclipse. These events affect the amount of light that we

[5] Officially also named 'Janssen' in honour of the Dutch spectacle maker Zacharias Janssen.

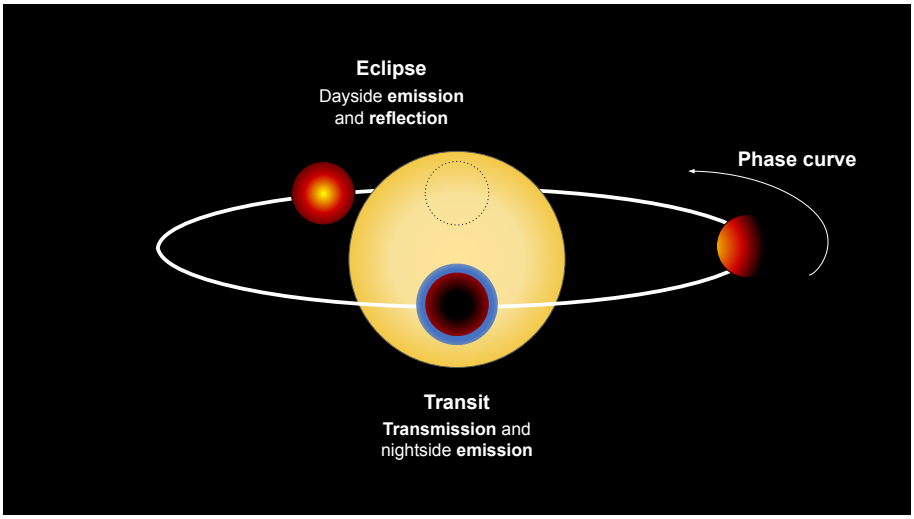


Figure 1.3: Different views of a planet: Depending on its position relative to its host star, we observe different aspects of a planet. HRE spectra produced in Chapters 3 and 5 represent what we may observe during an eclipse.

receive from the system due to the fact that when the planet passes behind the star, no light from the planet reaches us, and when the planet passes in front of the star, less light from the system reaches us. An example of an observation where this is very clearly visible is shown in Figure 1.4, where the light curve of the hot-Jupiter WASP-43 b is shown as observed with JWST (Bell et al. 2023, 2024). When the planet passes behind the star during the eclipse we see a small dip in the light received from the star and when the planet passes in front of the star we see a relatively larger dip in the amount of starlight. Both of these events have different advantages and drawbacks when trying to characterize an exoplanet atmosphere.

Transit spectroscopy, which was used to characterize solar systems bodies before the era of exoplanets (Smith & Hunten 1990), allows for the analysis of light after it has passed through the atmosphere of a planet. Depending on the composition, temperature, and size of the atmosphere, varying amounts of light are let through at different wavelengths, essentially providing a fingerprint of the planet's atmosphere. This has enabled the detection of a wide range of different chemical species such as H_2, H_2O, CO, CO_2, NH_3, Na, Fe, and many more[6].

This approach works best for large gaseous planets that support large atmospheres, such as WASP-43 b. For smaller planets with less prominent atmospheres, however, transit spectroscopy is harder to apply effectively. Heavy

[6] A fairly recent and comprehensive list including all sources is given in Guillot et al. (2022) in Table 4 of their appendix.

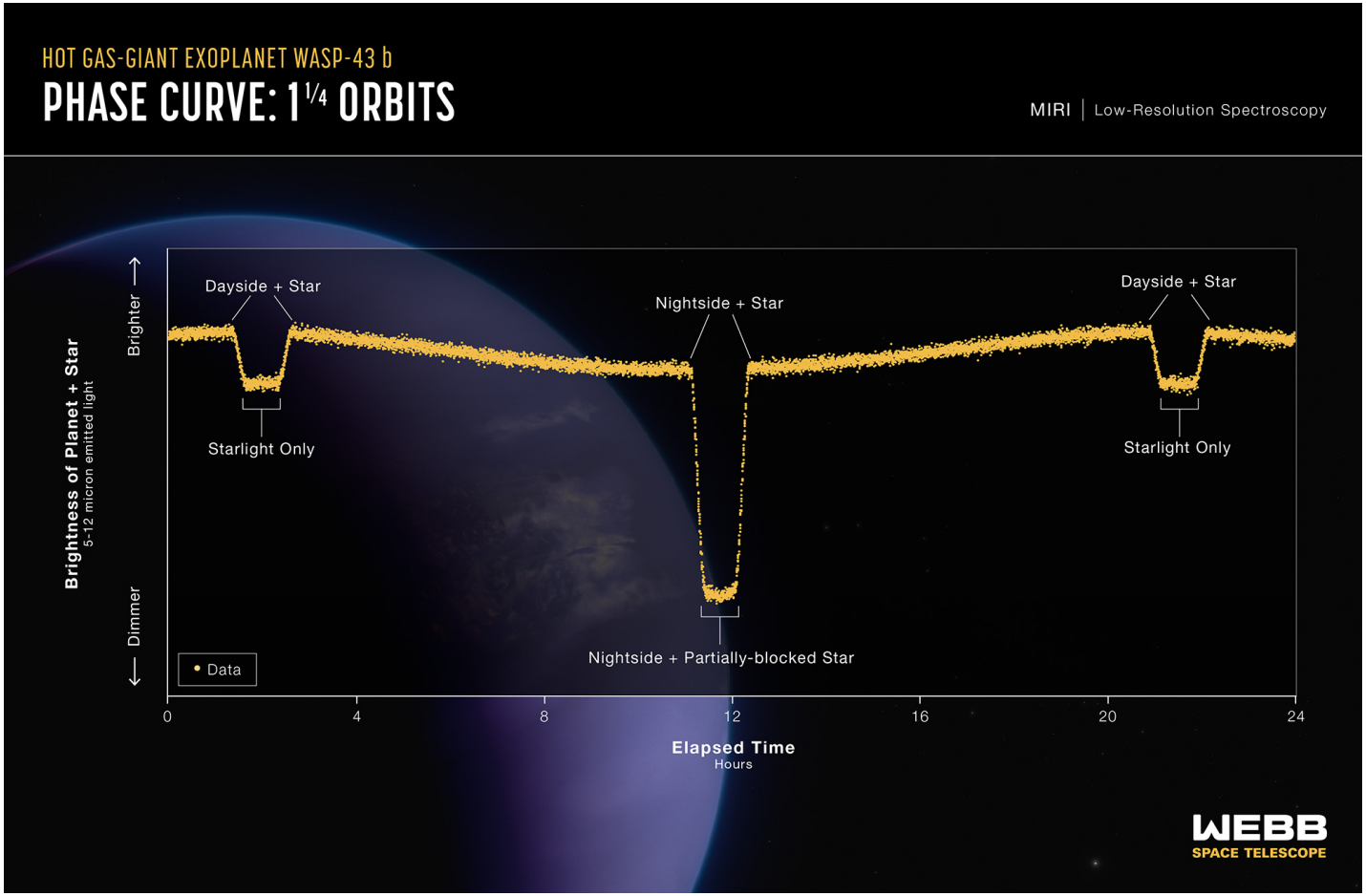


Figure 1.4: Phase Curve of WASP-43b: A clear example of how the flux received from a star changes with a function of time as a planet passes behind it during the eclipse (small dips at the beginning and end) and as the planet passes in front of the star (large dip in the middle). Data published in Bell et al. (2023, 2024). Source: NASA, ESA, CSA, Ralf Crawford (STScI).

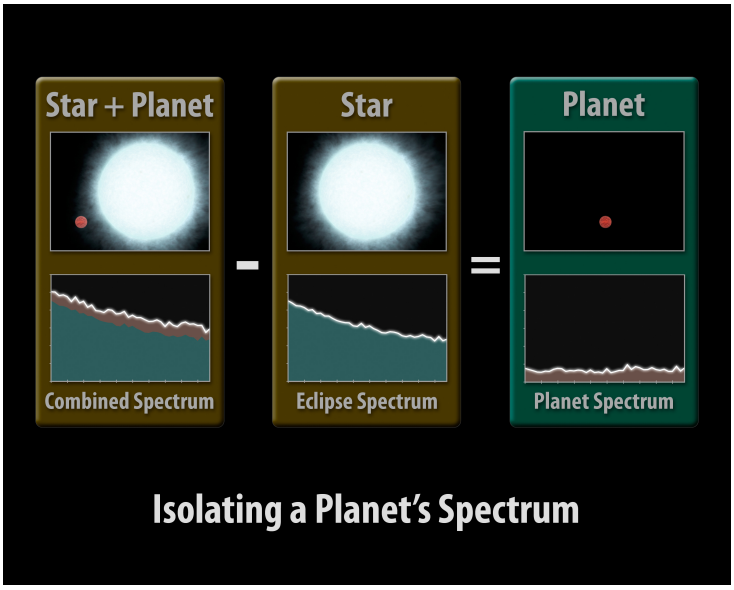


Figure 1.5: Isolating a planet's spectrum: The emission spectrum of an exoplanet can be extracted by subtracting the light received from the star only (during an eclipse) from that of the combined light of both the star and the planet (before and after the eclipse). Source: ESA

lava-vapour rich atmospheres, such as we expect to be present on HREs, could potentially have the additional issues of clouds and hazes potentially blocking light, leading to flat featureless spectra.

That is why for rocky planets (including HREs) one of the most common ways to analyse their atmospheres is by taking eclipse observations. One of the advantages of eclipses is that it allows for the isolation of the light radiated by the planet. As illustrated in Figure 1.5, subtracting the light from the star (gathered during the eclipse, when the planet is behind the star with respect to Earth) from the combined star and planet light, allows for the isolation of the planetary light.

Emission spectra are most easily taken for systems where the ratio of the flux from the planet to the flux from the star is as high as possible. This flux ratio is determined by the relative areas of the star and planet and their respective temperatures. This makes planets orbiting smaller stars from K-down to M-type more desirable targets (as shown in Chapter 3). Another way to increase the ratio of planet to star light is by observing in the infrared, a wavelength range in which planets are relatively bright thanks to thermal radiation. Hot planets, such as HREs, especially so.

Even when leveraging these advantages, extremely high photometric sensitivity is required to be able to discern the thermal emission of an exoplanet

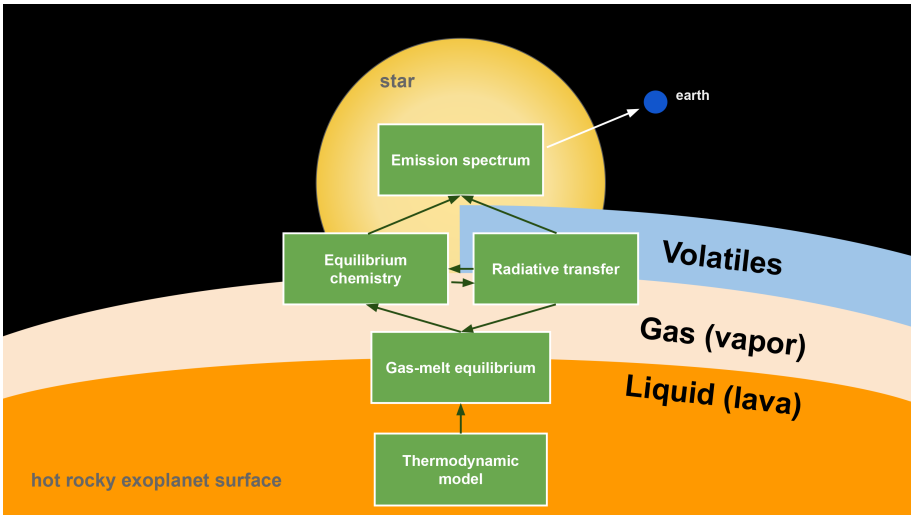


Figure 1.6: Overview of a forward model structure: Used for the self-consistent modelling of emission spectra for HREs.

from the light of its host star (planet to star flux ratios are most commonly denoted in parts per million). Hence, it wasn't until the advent of JWST that infrared emission spectra of HREs have been observed at a sensitivity high enough to start attempting to effectively characterise their atmospheres. This entails that the models of HRE atmospheres can finally be put to the test.

1.3.2 Modelling hot-rocky exoplanets

In Figure 1.6 we show a schematic that broadly outlines the way in which we have structured our models. Starting at the bottom, we use a thermodynamic model to calculate the thermodynamic properties of silicate melts. Using these properties, we then model the lava-atmosphere interaction using the LavAtmos code. The development of this code played a central role in the work done for this thesis, as can be read in Chapters 2 and 4. This code allows us to calculate the composition of rock vapour coming from lava at a given temperature, pressure, melt composition, and (optionally) with the presence of given volatile elements.

Once we know the composition of the vapour, we use this to determine the chemical composition of our atmosphere - including any volatile elements if needed. This information is then passed on to a code that determines the temperature pressure structure of the atmosphere. Finally we used a code that uses all this information to calculate the emission spectrum of the planet. This section is structured in such a way that we follow the model upward, explaining each step along the way.

Interior-atmosphere interactions

Throughout this work, we assume that the size of the lava oceans present on HREs are such that they dominate the atmosphere in terms of reservoir size. This is a common assumption made by most work that concerns itself with lava oceans on HREs (e.g. Schaefer & Fegley Jr. 2004; Zilinskas et al. 2022; Wolf et al. 2023; Seidler et al. 2024). This allows us to treat the interior-atmosphere interactions as one directional, with the lava ocean affecting the atmosphere and not vice versa.

The way in which a lava ocean affects atmospheric compositions is through vaporization reactions through which melt oxide species, which the lava is made of, transition from the liquid to the gas phase. Analogous to water evaporation at room temperature. To understand how we can calculate the partial pressure of different gas species due to this process, we have to understand the following equation derived from the law of mass action[7]:

$$P_{ij} = K_{r_{ij}}(T, P) a_j^{c_{ij}} P_{\mathrm{O_2}}^{d_{ij}} \tag{1.1}$$

P_{ij} is the partial pressure of a vapour species i resulting from the vaporization reaction of melt species j. To calculate this value we need to know the value of the chemical equilibrium constant of reaction ij $K_{r_{ij}}$, the activity of the melt oxide j a_j, and the O_2 partial pressure in the atmosphere P_{O_2}. The exponents $c_{i,j}$ and $d_{i,j}$ are the stoichiometric coefficients which ensure that the reaction is balanced. Taking the vaporization of SiO_2 (liquid) in the melt to SiO (gas) in the atmosphere as an example, equation 1.1 would be re-written as follows:

$$P_{\mathrm{SiO}} = K_r a_{\mathrm{SiO_2}} P_{\mathrm{O_2}}^{-1/2} \tag{1.2}$$

We start by finding the value of the chemical equilibrium constant of this reaction. Although named a constant, this value is dependent on both temperature and pressure. It being named a constant refers to the fact that it relates the concentration of a reactant to the concentration of a product at chemical equilibrium - this relation being constant at a given temperature and pressure. The value of K_r for each reaction ij can be derived from tabulated values of thermochemical properties of chemical species. The most widely used of these are the JANAF-NIST tables (Chase 1998), which is what we use throughout the majority of this work.

The next variable that we need to know is a_{SiO_2}, which is the activity of the melt oxide SiO_2. In essence, this value indicates how much of the SiO_2 in the melt is "available" for taking part in the vaporization reaction. The activity of melt oxide j is given by

$$a_j = y_j X_j \tag{1.3}$$

Where y_j is the so-called Raoultian activity coefficient, and X_j is the mole fraction of the given melt oxide. Using SiO_2 again as an example, if it were an

[7] The full derivation of this equation is given in section 2.2.

ideal system where all of the SiO_2 in the melt was available, y would equal 1 and hence the activity would be equal to the mole fraction X of SiO_2 in the melt. For non-ideal systems, the y may have any value greater than 0.

Due to the complexity of the behaviour of oxide species in melts, there are currently no comprehensive analytical models derived from first principles that are able to accurately calculate the activities of oxide species in complex melts (melts containing more than two different oxides). Instead, models are built based on empirical measurements of melt-oxide activities. In Chapter 2 we detail how we use the thermochemical code MELTS developed by Ghiorso & Sack (1995) to calculate the activity of melt oxides for vaporization reactions - which is what we use for the work done throughout the rest of the chapters as well.

When the work for this thesis was originally started, most studies of HREs assumed that they were too hot to support any volatile elements (such as H, C, N, S, and P) in their atmospheres. However, theoretical models have since shown that HREs could potentially host large amounts of water in their lava oceans (Hirschmann 2012; Lebrun et al. 2013; Dorn & Lichtenberg 2021; Kite & Schaefer 2021) and that volatile atmospheres could be supported even when considering the extremely strong irradiation from their host stars (Herbort et al. 2022; Charnoz et al. 2023; Maurice et al. 2024). This has prompted modelling work on what the emission spectra of HREs with volatile species in their atmospheres could look like (Piette et al. 2023; Zilinskas et al. 2023; Falco et al. 2024). In addition, the recent JWST observations of the HRE 55-Cnc e indicate the possibility of the presence of a significant volatile atmosphere, based on a significantly lower probed temperature than expected as well as strong infrared absorption features (possibly due to CO or CO_2). This amounts to a growing body of work pointing at the importance of including volatile elements when modelling HREs.

The first order approach to including volatile elements in forward models of HREs, is to calculate the vapour composition coming from a melt while assuming no volatile elements are involved and to then add the abundances of the vaporised elements (Si, Al, Ti, Fe, Mg, Ca, Na, K, and depending on the approach also O) to predetermined abundances of volatile elements. This is the approach taken in Piette et al. (2023) and (Zilinskas et al. 2023) and gives a good initial idea of how volatile species in an HRE atmosphere affect the emission spectrum. However, this approach does not take into account what the effect is of volatile elements on the vaporisation process itself.

In Charnoz et al. (2023), it is shown how even low H abundances can have a significant effect on the vaporisation of species from the surface lava ocean, leading to higher abundances of the vaporised elements than previously thought. Based on this work and with a similar approach, we expanded LavAtmos (the vaporisation model from chapter 2) to also include H, C, N, S, and P in the vaporisation reactions, leading to the development of LavAtmos 2.0. This work is covered in detail in chapter 4.

With these vaporisation codes, we are able to calculate the elemental composition of the vapour released into the atmosphere of an HRE based on the surface temperature, pressure, and composition of the surface lava ocean. The next step in building a full model of the atmosphere is to calculate the atmospheric gas chemistry.

Atmospheric chemistry

We make use of vaporisation codes to calculate the composition of an HRE atmosphere at the surface of the lava ocean. Although the output of these codes is in terms of chemical species, we tend to convert this to abundances and pass it on to a dedicated gas-chemistry code to calculate the chemical speciation of the atmosphere. This is because 1. dedicated gas-equilibrium chemistry codes often include a greater number of gas species than our vaporisation and 2. we want to know the speciation throughout the entire atmosphere (at varying temperatures and pressures) and not just at the surface of the planet.

Due to the high temperatures of HREs, it is common to assume chemical equilibrium throughout the entirety of the atmosphere. This allows the problem of chemical speciation to be approached through the method of minimizing the Gibbs free energy of a system (e.g. Denbigh 1955; Aris 1969), an approach through which it is possible to calculate the equilibrium composition of a system without needing to write out every possible equilibrium reaction. To do this, we make use of the code FastChem (Stock et al. 2018, 2022; Kitzmann et al. 2024) which is semi-analytical code which is able to quickly and accurately calculate chemical speciation over a wide range of pressures and temperatures.

Radiative Transfer

Once we have a grid of chemical species for a range of temperatures and pressures, we can use this to build a model of how light propagates through the atmosphere. This is done through the use of 1-D radiative transfer climate models. Initially developed for the modelling of atmospheres of solar-system bodies, these are now also commonly applied to exoplanet atmospheres (Manabe & Strickler 1964; Sudarsky et al. 2003; Fortney et al. 2005). The aim of these models is to solve the propagation of stellar flux through the planetary atmosphere and, in doing so, derive its temperature-pressure structure.

One of the most influential factors in this process is the chemical composition of the atmosphere. Since different species absorb and emit radiation differently depending on their abundance, temperature, and pressure, an accurate representation of the chemical makeup across a broad temperature-pressure (TP) grid is essential. Once the composition is known, opacities of each chemical species dictate how radiation interacts with the atmosphere. The absorption properties of various atomic, ionic, and molecular species vary across wavelengths, making opacity calculations a key ingredient in atmospheric modelling.

Determining these opacities is an entire research field of its own, with dedicated collaborations (such as DACE[8] and ExoMol[9]) for the compiling and refining of spectroscopic line lists based on both experimental measurements and theoretical calculations. Table 5.2 in the appendix of Chapter 5 illustrates the vast number of species required for accurate modelling and the collaborative effort behind acquiring the data necessary to calculate opacities.

Due to the complexity of solving radiative transfer from first principles, an approximation was developed to enable more efficient computations. The two-stream approximation, first introduced by Schuster (1905), simplifies the radiative transfer equation by considering only two directional fluxes: upward from the atmosphere's base and downward from the top. To achieve radiative equilibrium, the atmospheric temperature structure is iteratively adjusted until the net energy flux at each layer is zero, ensuring a balance between incoming and outgoing radiation. In this work, we utilize the HELIOS code (Malik et al. 2017), which implements this approach with additional optimizations for exoplanetary atmospheres.

Once the radiative code converges on a temperature-pressure (TP) profile of the atmosphere, the chemical equilibrium code is used one more time to determine the chemical composition throughout the atmosphere[10], providing us with all of the information that we need to produce an emission spectrum. This last step is done using a different radiative transfer code called petitRADTRANS (Mollière et al. 2019), the output of which we can then compare to real observed emission spectra of HREs.

Even with this simplified 1-D approach, constructing a self-consistent model of an exoplanet atmosphere requires integrating diverse datasets, including chemical abundances, opacity sources, and radiative transfer methods. The complexity of these models highlights the extensive groundwork necessary to accurately simulate (exo)planetary atmospheres and interpret observational data.

1.4 What did we find?

The overarching goal of the work presented in this thesis is to understand how the surface lava oceans of HREs influence their atmospheric composition and how this in turn affects their emission spectra. The forward modelling technique that we use is based on combining a range of different numerical models which each simulate a different aspect of an HRE atmosphere. A large part of this thesis is focussed on improving and expanding the code dealing with one specific aspect of the forward modelling: the vaporisation from a lava ocean surface. As a result of this, the chapters included in this thesis can be broadly

[8] https://dace.unige.ch/opacityDatabase/

[9] https://www.exomol.com/

[10] We also include an additional iteration to ensure that the surface temperature derived from the TP profile is consistent with the temperature used for the vaporisation calculations. See Chapters 3 a 5 for a detailed explanation.

categorized in two types of works: 1. the development of vaporisation codes (Chapters 2 and 4) and 2. the integration of these codes into the greater forward modelling framework to assess their impact on synthetic emission spectra of HREs (Chapters 3 and 5).

In short, we start in Chapter 2 with the development of a melt-vaporisation code (LavAtmos) that assumes that no volatile elements are present. In Chapter 3, we then apply this code within the greater forward modelling framework to understand how varying melt compositions affects HRE temperature-pressure structures and emission spectra. Chapter 4 focusses on expanding the vaporisation model to also include volatile elements in the vaporisation reactions (LavAtmos 2) and on understanding how this affects the abundance of certain melt-vapour species. Finally, Chapter 5 uses this expanded version of the melt-vaporisation code within the full forward modelling framework to investigate what the emission spectra of HREs may look like if they support an atmosphere containing volatile elements. Below is a concise overview of the approach we took for each chapter and the most important findings.

Chapter 2: Developing LavAtmos

The first challenge of this project was to develop a melt-vaporisation mode. When we started there were two melt-vaporisation codes in use in literature. The first of these - called MAGMA - was a code originally developed for the study of lava-vaporisation on solar system bodies (Fegley & Cameron 1987; Schaefer & Fegley Jr. 2004), but was subsequently applied to the study of exoplanets (Schaefer & Fegley 2009; Miguel et al. 2011; Kite et al. 2016). The reasons that an alternative to this code was desirable were that it is not open source, so it had limited availability, and it used a (potentially) outdated model for calculating melt activities[11] called 'ideal mixing of complex components' (IMCC) developed by Hastie et al. (1982b); Hastie & Bonnell (1985, 1986).

The second available code was VapoRock (Wolf et al. 2023). This code is open-source and uses a more comprehensive model for estimating melt activities called MELTS (Ghiorso & Sack 1995; Asimow & Ghiorso 1998; Ghiorso et al. 2002; Gualda et al. 2012; Ghiorso & Gualda 2015). The reason we opted to still develop our own melt-vaporisation code was because VapoRock treats O_2 partial pressure as a user input instead of calculating it self-consistently, which was being done by MAGMA, a feature that we desired as well.

As such, we wrote a new open-source melt-vaporisation code called LavAtmos which combined the (in our opinion) best aspects of the two other existing codes: making use of the MELTS thermochemical model for calculating the activities of the melt species (as used by VapoRock) and using the mass-balance and mass-action constraints for calculating the O_2 partial pressure of the system (as used by MAGMA).

[11] See section 1.3.2 for an explanation of the role of melt activities.

Chapter 3: Applying LavAtmos to different melt compositions

Having developed a melt-vaporisation code, the next logical step was to apply it. One of the key questions of HREs is whether or not variation in the composition of surface lava oceans could have an observable effect on their emission spectra. As of yet, we have little information on what compositions we should expect for rocky exoplanets and so the majority of work done on HREs assumes that the composition of the surface lava ocean is equivalent to that of the bulk silicate earth (BSE) (Palme & O'Neill 2003).

Using this standard composition as a starting point, we investigated how deviating from this composition for each of the main melt oxides would affect the emission spectra of HREs. We found that HRE emission spectra are sensitive to the amounts of TiO_2, SiO_2, and to a lesser extent Na_2O and K_2O in their surface lava oceans. The resulting changes in the emission spectra due to varying TiO_2 and SiO_2 melt abundances may potentially be large enough to be detectable on the some of the brightest HREs given sufficient JWST observing time.

Chapter 4: Developing LavAtmos 2.0

A key question to answer when modelling melt-vaporisation is how the process is affected by the presence of volatile elements such as H, C, N, S, and P. In Charnoz et al. (2023) it was shown how including H in vaporisation reactions could have a significant impact on the abundances of melt-vapour species. We realised that with some work we could expand the capabilities of LavAtmos to also include volatile elements using a similar approach. In addition tos adding H, we were also able to include C, N, S, and P.

Unlike the first version of LavAtmos, which was an iteration upon other codes with output that was generally well understood, LavAtmos 2 required a much more in-depth exploration of how including volatile elements could affect the chemistry of a melt-vapour system. We found that the increase in vapour-species abundance due to the presence of volatile elements varies depending on the abundance of the different volatile elements, with elements that are prone to forming oxidised molecules such as C having a stronger effect on the vaporisation than N for example.

Since the O abundance in the atmosphere is also dictated by the vaporisation reactions and the presence of volatile elements increases the abundance of vaporised species, we find that this leads to a more oxidised atmospheric composition. As such, we find that a low C/O ratio in an HRE atmosphere could potentially serve as an indication that a surface lava ocean is present.

Chapter 5: Applying LavAtmos 2 to volatile HRE atmospheres

After developing LavAtmos 2, we integrated it into the full forward model, allowing for a more self-consistent approach to modelling the thermal emission

spectra of volatile bearing atmospheres of HREs.

We found that the presence of both a surface lava ocean and atmospheric volatiles leads to very strong H^- continuum opacity. Melt-vapour from the lava ocean enriches the atmosphere with metals, which, when ionized, provides an abundance of free-electrons. Adding but a small amount of H to the atmosphere ($\simeq$ 1e-6 bar) yields a H^- continuum that is so strong that the spectral features of other major atmospheric species are no longer detectable.

Additionally, we found that H^- continuum opacity shifts the photosphere of an HRE to higher altitudes compared to an atmosphere without H^- continuum. In the inverted atmospheres typical of most HREs, this means the photosphere radiates from a much hotter region, making the emission spectrum significantly brighter.

Based on these findings, we conclude that if an H^- continuum is detected in an HRE, it could potentially point to the presence of a surface lava ocean.

Future work

It lies in the nature of scientific research to never truly be done. There is always something more to look into, one last thing to check, or a different direction from which to approach an issue. This is especially true in the field of exoplanet research. As our research methods improve, more and more different scientific disciplines need to be involved to gain a comprehensive understanding of the objects we study. Taking this single thesis as an example, we need to understand: geochemistry, gas-chemistry, thermodynamics and radiative transfer, each of which are fully fledged research fields of their own. However, to quote a professor from our institute "The best thesis, is a finished thesis".

Although the work for this thesis may be done, the work in this field is anything but. We are only at the very start of being able to characterise exoplanet atmospheres. Besides the promising results already coming in from JWST, there is a whole suite of telescopes under development that will push the sensitivity of our observational data to new limits. Increasingly information rich data will also force the theoretical aspects of exoplanet research to be greatly expanded. Something which is also already happening with the development of increasingly efficient numerical methods, ever more computation power, and the promise of the effective applications of artificial intelligence.

I am very excited to see what the future holds and grateful that I've had the chance to play a small part in furthering our understanding of these neighbouring yet terribly far off worlds.

2 LavAtmos: An open-source chemical equilibrium vaporization code for lava worlds

Work published in **C. P. A. van Buchem**, Y. Miguel, M. Zilinskas, and W. van Westrenen 2023, *Meteoritics & Planetary Science*, 58, Nr 8, 1149–1161 (2023). Reprinted here in its entirety.

Abstract

To date, over 500 short-period rocky planets with equilibrium temperatures above 1500 K have been discovered. Such planets are expected to support magma oceans, providing a direct interface between the interior and the atmosphere. This provides a unique opportunity to gain insight into their interior compositions through atmospheric observations. A key process in doing such work is the vapor outgassing from the lava surface. LavAtmos is an open-source code that calculates the equilibrium chemical composition of vapor above a dry melt for a given composition and temperature. Results show that the produced output is in good agreement with the partial pressures obtained from experimental laboratory data as well as with other similar codes from literature. LavAtmos allows for the modeling of vaporization of a wide range of different mantle compositions of hot rocky exoplanets. In combination with atmospheric chemistry codes, this enables the characterization of interior compositions through atmospheric signatures.

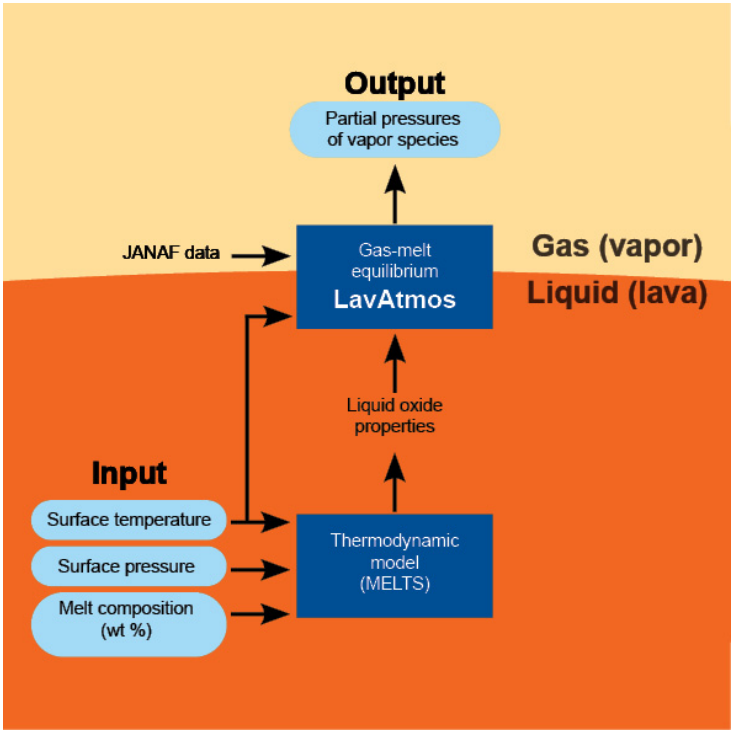


Figure 2.1: LavAtmos schematic: LavAtmos is a code that calculates the composition of the gas above lava at certain surface temperature, pressure, and composition. The MELTS code developed by Ghiorso and co-authors is used to calculated liquid oxide properties for the given input. This is then used alongside data from the JANAF tables in order to perform gas-melt equilibrium calculations. The final output is partial pressure for each of the included vapor species. *Graphical abstract included in publication.*

2.1 Introduction

With an ever-growing catalog of newly discovered exoplanets, we have moved from the discovery phase well into the characterization phase. An emerging category of specific interest is that of the so-called hot rocky exoplanets.

These planets are exposed to extreme stellar irradiation that leads to surface temperatures hot enough to prevent the planet from cooling and creating a crust (Boukaré et al. 2022; Henning et al. 2018), exposing the silicate mantle directly to the atmosphere. Furthermore, since the atmosphere is a direct product of the outgassing from the magma ocean and is in equilibrium with it, the atmospheric compositions of these planets are directly influenced by the interior composition (Dorn & Lichtenberg 2021; Ito et al. 2015; Kite et al.

2016, 2020; Miguel et al. 2011; Nguyen et al. 2020). This provides a unique opportunity to derive interior properties from atmospheric observations. In addition, there is growing evidence that planetesimals, as well as the rocky planets and moons that form from their accretion, were covered by magma early in their evolution (Elkins-Tanton 2012; Greenwood et al. 2005; Hin et al. 2017; Norris & Wood 2017; Schaefer & Elkins-Tanton 2018). Therefore, constraints on the atmospheric products of interior-atmosphere interactions on hot rocky exoplanets might also provide us with a window to the conditions in the early solar system and early Earth (Hirschmann 2012).

Hot rocky planets have been the targets of several observing programs throughout the past several years on a range of different ground- and space-based telescopes (Deibert et al. 2021; Demory et al. 2011; Esteves et al. 2017; Keles et al. 2022). Conclusions drawn from these observations remain uncertain and have yet to give definitive proof of an atmosphere. However, some tentative evidence has been given for K2-141 b (Zieba et al. 2022) and 55 Cnc e (Angelo & Hu 2017; Demory et al. 2016b; Zilinskas et al. 2020, 2021), and the advent of the new generation of telescopes, such as JWST and Ariel, may allow for the characterization of the chemical composition of hot rocky-exoplanet atmospheres in the near future (Ito et al. 2021; Zilinskas et al. 2022).

To know what to look for in such observations and to interpret the data once it arrives, accurate atmospheric models are required. For atmospheres on hot rocky exoplanets, this involves modeling the degassing from lava at the surface of the planet. Since we yet have to gain a good understanding of the possible types of rocky-exoplanet compositions, we do not yet know what kind of compositions we should expect for these melts. Recent work (Brugman et al. 2021; Putirka et al. 2021; Putirka & Rarick 2019) indicates that we should expect a wide range of different possible silicate compositions. Hence, open-source vaporization codes that can work with a wide range of compositions are necessary to enable modeling potential atmospheres as our understanding of hot rocky planets develops.

To date, a limited number of codes have been used to calculate the chemical composition of vapors degassing from lava at a given temperature and the composition of an atmosphere in equilibrium with lava of a given temperature. The MAGMA code (Fegley & Cameron 1987) was written to study the fractional vaporization of Mercury. The same code was used for the study of other solar system bodies (Schaefer & Fegley 2007; Schaefer & Fegley Jr. 2004) and exoplanets (Kite et al. 2016; Miguel et al. 2011; Schaefer & Fegley 2009; Schaefer et al. 2012; Visscher & Fegley 2013). This code makes use of the Ideal Mixing of Complex Components (IMCC) model, developed by Hastie and co-authors (Hastie & Bonnell 1985, 1986; Hastie et al. 1982b), to calculate the activity of the oxide components in the melt.

In more recent years, the MELTS code (Ghiorso & Sack 1995) has seen increased use for modeling the thermodynamics for outgassing codes (Ito et al. 2015, 2021; Jäggi et al. 2021; Wolf et al. 2023). Wolf and coauthors have devel-

oped the code named VapoRock which has been used to model the early atmosphere of Mercury (Jäggi et al. 2021) and to explore how relative abundances of SiO and SiO_2 could be used to infer the O_2 fugacity of a volatile-depleted mantle (Wolf et al. 2023). The main difference between VapoRock and LavAtmos is the manner in which the O_2 partial pressure is determined. In the discussion ("Discussion" Section), we include a more in-depth comparison of the two codes. Other approaches that calculate the condensate compositions from an initial gas composition, as opposed to calculating vaporization reactions from an existing melt reservoir, have also been developed in the literature (Herbort et al. 2020, 2022).

In this paper, we present a new open-source code, which we named LavAtmos, that calculates the equilibrium composition of a vapor above a melt of a given composition, at a given temperature and at a given melt–vapor interface pressure. As shown in the graphical table of contents, a general overview of the workflow of the code is presented. Just as the abovementioned previous works (Ito et al. 2015, 2021; Wolf et al. 2023), we use MELTS to calculate the oxide component properties of a melt. These properties are then combined with thermochemical data available in the JANAF tables (Chase 1998) to perform gas–melt equilibrium calculations. The oxygen fugacity (fO_2) is derived from the law of mass action, similarly to the approach used for thermodynamic calculations for pure silica and alumina (Krieger 1965) and for the MAGMA code Fegley & Cameron (1987). LavAtmos currently takes 9 oxide species into account (SiO_2, MgO, Al_2O_3, TiO_2, Fe_2O_3, FeO, CaO, Na_2O, and K_2O), 31 different vapor species with corresponding vaporization reactions (shown in Table 1) and is suitable for calculations between 1500 and 4000 K. LavAtmos is written in Python for ease of use and integration with the MELTS Python wrapper named Thermoengine.1 It is released as an open-source code under the GNU General Public License version 3.2 LavAtmos is available on `https://github.com/cvbuchem/LavAtmos`.

In this paper, we provide an in-depth look at the methods used in "Methodology" Section. We compare its performance to laboratory data and the results calculated by other similar codes where those are available in the public domain in "Validation" Section. Finally, we discuss assumptions made in the method, the advantages and limitations of the code, and highlight a set of potential applications in "Discussion" Section, rounding off with a conclusion in "Conclusion" Section.

2.2 Methodology

In this section, we cover how the partial pressures of included species are calculated. Consider the generalized form of a vaporization reaction of a liquid oxide j, gaseous O_2, and the resulting vapor species i:

$$c_{ij}\mathrm{X}_{x_j}\mathrm{O}_{y_j}(\mathrm{l}) + d_{ij}\mathrm{O}_2(\mathrm{g}) \Leftrightarrow \mathrm{X}_{x_j c_{ij}}\mathrm{O}_{y_j c_{ij}+2d_{ij}}(\mathrm{g}) \tag{2.1}$$

X is the cation of the species, x_j the number of cation atoms, y_j the number of oxygen atoms, and c_{ij} and d_{ij} are the stoichiometric coefficients for this reaction. The gaseous species (atmosphere) are indicated using (g) and the liquid species (melt) using (l). As an example, the vaporisation reaction of liquid SiO_2 to form gaseous SiO can be written as:

$$SiO_2(l) - \frac{1}{2}O_2(g) \Leftrightarrow SiO(g) \tag{2.2}$$

Assuming that the reaction is in equilibrium, the partial pressure of the vapor species i can be calculated by adhering to the law of mass action as follows:

$$P_{ij} = K_{r_{ij}} a_j^{c_{ij}} P_{O_2}^{d_{ij}} \tag{2.3}$$

where P_{ij} is the partial pressure of vapor species i as formed from liquid species j, $K_{r_{ij}}$ is the chemical equilibrium constant of the reaction, a_j is the activity of liquid oxide j, and P_{O_2} is the partial pressure of O_2 (also known as the oxygen fugacity fO_2). Some more elaboration on the derivation is shown in the appendix (section 2.A). For the example reaction shown in equation 2.2, the partial pressure of SiO can be determined using:

$$P_{SiO} = K_r a_{SiO_2} P_{O_2}^{-1/2} \tag{2.4}$$

The variables that must be known to calculate the partial pressure of a vapor species are the stoichiometric coefficients c_i and d_i, the chemical equilibrium constant of reaction $K_{r_{i,j}}$ for the vapor species i and the melt oxide j, the chemical activity a_j of the melt oxide j involved in the reaction, and the oxygen partial pressure P_{O2}. Stoichiometric coefficients are determined by writing out balanced reaction equations (see Table 2.1). The chemical equilibrium constant of each reaction $K_{r_{ij}}$ is determined using the data available in the JANAF tables (Chase 1998).

The activity of the oxides in the melt is determined using the MELTS code. Developed over the course of the past two and a half decades, MELTS has been consistently updated and expanded (Asimow & Ghiorso 1998; Ghiorso & Gualda 2015; Ghiorso et al. 2002; Ghiorso & Sack 1995; Gualda et al. 2012). It performs internally consistent modeling of liquid–solid equilibria in magmatic systems at elevated temperatures and pressures. For a given temperature, pressure, and composition (in terms of oxide weight percentages, see Table 2.2 for example compositions), MELTS is able to calculate the thermochemical properties of the end-member component species that it accounts for in each included phase (Ghiorso & Sack 1995). In the current version of LavAtmos, only the liquid phase is used. Hence, as of yet, partial melting is not taken into account. The properties, specifically the activities, of these end-member components are used by LavAtmos to calculate the energetics of the vaporization reactions of the oxides in the melt. The end-member species included in our MELTS calculations are SiO_2, Al_2O_3, TiO_2, Fe_2O_3, Fe_2SiO_4, Mg_2SiO_4, $CaSiO_3$, Na_2SiO_3,

and $KAlSiO_4$[1]. Due to the fact that some of these species include more than one cation, we write vaporisation reactions that produce a vapor species for one of the cations and liquid species for the others, similarly to the approach taken in work done on condensates from impacts between silicate-rich bodiesFedkin et al. (2006). Using $KAlSiO_4$ as example, the equilibrium vaporisation reaction may be written as:

$$KAlSiO_4(l) - \frac{1}{4}O_2(g) - \frac{1}{2}Al_2O_3(l) - SiO_2(l) \Leftrightarrow K(g) \tag{2.5}$$

Therefore, the partial pressure for K is calculated using:

$$P_K = K_r a_{KAlSiO_4} P_{O_2}^{-1/4} a_{Al_2O_3}^{-1/4} a_{SiO_2}^{-1} \tag{2.6}$$

Since Al_2O_3 and SiO_2 are also end-member species, their activities are known. In the cases where a gas species has more than one reaction producing it, such as for Fe (reactions 16 and 18 in Table 2.1) and FeO (reactions 17 and 19 in Table 2.1), the total partial pressure of the species is equal to the sum of the partial pressures calculated for each reaction.

MELTS also requires a pressure as input. For the results shown in this paper, we assume a surface pressure of 0.1 bar. When testing the results for a range of pressure from 10^{-4} up to 100 bar there were no significant differences in the resulting partial pressures. This pressure range includes the atmospheric pressures expected at the lava-atmosphere interface on hot rocky exoplanets (Zilinskas et al. 2022). We assume the silicate compositions are fully molten and for this reason only include the liquid phase in the MELTS calculations. The Python wrapper named Thermoengine is used to interact with the MELTS code (written in C). At the moment of submission of this manuscript, LavAtmos works with MELTS version 1.0.2. This version includes rhyolites-MELTS (Gualda et al. 2012) allowing for the modeling of hydrous silicic systems which may become relevant in future iterations of LavAtmos.

Looking back at equation 2.3, we still need to determine the O_2 partial pressure (P_2). For this, we assume that the metal to oxygen ratio in the vapor is the same as the stoichiometries of the melt oxides, as is also done in the vapor calculations done by Krieger (1965). This gives us a mass balance equation in the form of:

$$n_{O_2} = -\sum_i \sum_j d_{ij} n_{ij} \tag{2.7}$$

The definition of partial pressure ($P_{ij} = \frac{n_{ij} P}{n}$ for vapor species i produced from liquid species j) can be applied in order to rewrite equation 2.7 as:

$$P_{O_2} = -\sum_i \sum_j d_{ij} P_{ij} \tag{2.8}$$

[1]The mole fraction of each of these end-member species is derived by MELTS from the melt composition given in terms of weight percentages of SiO_2, MgO, Al_2O_3, TiO_2, Fe_2O_3, FeO, CaO, Na_2O, and K_2O.

Table 2.1: Overview of the 31 vaporization reactions included in LavAtmos - Reaction 1 is the gas to gas reaction of O_2 to O. The rest of the reactions (2-31) describe the vaporization reactions. Each vapor species has a unique reaction that includes a MELTS end-member species, O_2, and (if necessary) residue liquid metal oxides.

End-member	#	**Reactants**		**Vapor**
–	1	1/2 O_2(g)	⇆	O(g)
SiO_2	2	SiO_2(l) + O_2(g)	⇆	Si(g)
	3	2SiO_2(l) + 2O_2(g)	⇆	Si_2(g)
	4	3SiO_2(l) + 3O_2(g)	⇆	Si_3(g)
	5	SiO_2(l) + 1/2 O_2(g)	⇆	SiO(g)
	6	SiO_2(l)	⇆	SiO_2(g)
Al_2O_3	7	1/2 Al_2O_3(l) + 3/4 O_2(g)	⇆	Al(g)
	8	Al_2O_3(l) + 3/2 O_2(g)	⇆	Al_2(g)
	9	1/2 Al_2O_3(l) + 1/4 O_2(g)	⇆	AlO(g)
	10	Al_2O_3(l) + O_2(g)	⇆	Al_2O(g)
	11	1/2 Al_2O_3(l) + 1/2 O_2(g)	⇆	AlO_2(g)
	12	Al_2O_3(l) + 1/2 O_2(g)	⇆	Al_2O_2(g)
TiO_2	13	TiO_2(l) + O_2(g)	⇆	Ti(g)
	14	TiO_2(l) + 1/2 O_2(g)	⇆	TiO(g)
	15	TiO_2(l)	⇆	TiO_2(g)
Fe_2O_3	16	1/2 Fe_2O_3(l) + 3/4 O_2(g)	⇆	Fe(g)
	17	1/2 Fe_2O_3(l) + 1/4 O_2(g)	⇆	FeO(g)
Fe_2SiO_4	18	1/2 Fe_2SiO_4(l) + 1/2 O_2(g) + 1/2 SiO_2(l)	⇆	Fe(g)
	19	1/2 Fe_2SiO_4(l) + 1/2 SiO_2(l)	⇆	FeO(g)
Mg_2SiO_4	20	1/2 Mg_2SiO_4(l) + 1/2 O_2(g) + 1/2 SiO_2(l)	⇆	Mg(g)
	21	Mg_2SiO_4(l) + O_2(g) + SiO_2(l)	⇆	Mg_2(g)
	22	1/2 Mg_2SiO_4(l) + 1/2 SiO_2(l)	⇆	MgO(g)
$CaSiO_3$	23	$CaSiO_3$(l) + 1/2 O_2(g) + SiO_2(l)	⇆	Ca(g)
	24	2$CaSiO_3$(l) + O_2(g) + 2SiO_2(l)	⇆	Ca_2(g)
	25	$CaSiO_3$(l) + SiO_2(l)	⇆	CaO(g)
Na_2SiO_3	26	1/2 Na_2SiO_3(l) + 1/4 O_2(g) + 1/2 SiO_2(l)	⇆	Na(g)
	27	Na_2SiO_3(l) + 1/2 O_2(g) + SiO_2(l)	⇆	Na_2(g)
	28	1/2 Na_2SiO_3(l) + 1/4 O_2(g) + 1/2 SiO_2(l)	⇆	NaO(g)
$KAlSiO_4$	29	$KAlSiO_4$(l) + 1/4 O_2(g) + 1/2 Al_2O_3(l) + SiO_2(l)	⇆	K(g)
	30	2$KAlSiO_4$(l) + 1/2 O_2(g) + Al_2O_3(l) + 2SiO_2(l)	⇆	K_2(g)
	31	$KAlSiO_4$(l) + 1/4 O_2(g) + 1/2 Al_2O_3(l) + SiO_2(l)	⇆	KO(g)

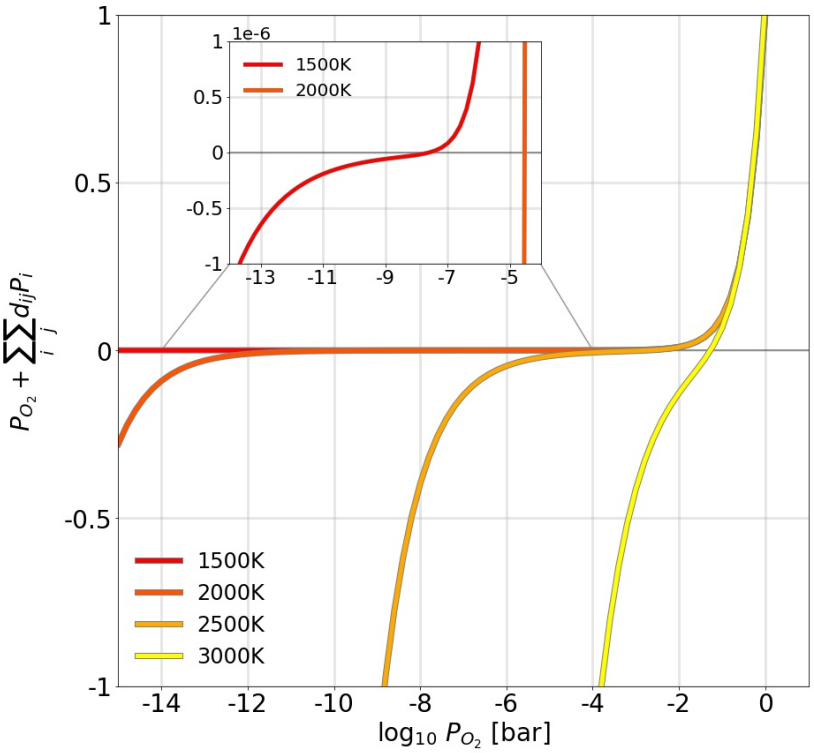


Figure 2.2: Behavior of the mass law function as a function of P_{O_2} at different temperatures - LavAtmos determines the P_{O_2} value by solving the mass law function shown in 2.9. Here we see the behavior of the function for different P_{O_2} values and at different temperatures. An inset is used to show the behavior of the function at a melt temperature of 1500 K due to the difference in scale within which the changes occur relative to higher temperatures.

It is here that we see the importance of tracking the partial pressure of a vapor species i released from a specific reaction with a liquid oxide j. For vapor species that have more than one reaction producing them, such as the aforementioned Fe and FeO, it is necessary to couple the corresponding partial pressures of released Fe/FeO (P_{ij}) to the right stoichiometry (d_{ij}). Substituting equation 2.3 and setting one side to 0 gives:

$$0 = P_{O_2} + \sum_i \sum_j d_{ij} K_{r_{ij}} a_j^{c_{ij}} P_{O_2}^{d_{ij}} \tag{2.9}$$

Finding the P_{O_2} for which equation 2.9 holds, allows one to calculate the partial pressures of all other vapor species (using equation 2.3) while ensuring that the mass action law is being upheld. In Figure 2.2, the behavior of the right side of equation 2.9 as a function of P_{O_2} is shown for different melt temperatures. The

higher the melt temperature, the greater the P_{O_2} value at which equation 2.9 holds true (where the y-axis is zero in Figure 2.2). If a P_{O_2} value is used that corresponds to a (non-zero) negative value on the y-axis at a given temperature, this implies that not all of the O_2 released during vaporization reactions is included in the vapor. If a P_{O_2} value is used that corresponds to a (non-zero) positive value on the y-axis at a given temperature, this implies that extra oxygen would have to be added to the system in order to reach the calculated equilibrium.

In LavAtmos, equation 2.9 is solved for P_{O_2} using the Scipy optimization function `fsolve`[2]. A vaporization reaction is defined for each vapor species included in LavAtmos (as shown in Table 2.1).

2.3 Validation

Table 2.2: Melt compositions used for Figures REFERENCE - The compositions given are for SRM glass (Hastie & Bonnell 1985), Illite (Hastie et al. 1982b), bulk silicate earth (BSE) (Palme & O'Neill 2003), a CB chondrite chondrule with bulk Na and K mass balanced for chondrules to fit bulk meteorite iron-silicate ratio (Weisberg et al. 1990, 2001), an analog to enstatite chondrites (EH4) (Wiik 1956), and Northern Smooth Planes (NSP) lava for both source and lava (Namur et al. 2016; Nittler & Weider 2019).

Oxide wt%	SRM glass	Illite	BSE	CB	EH4	NSP source	NSP lava
SiO_2	71.390	60.200	45.400	50.700	62.730	53.670	58.700
MgO	0.270	2.100	36.760	36.900	30.240	36.890	13.900
Al_2O_3	2.780	26.000	4.480	4.600	2.580	4.750	13.800
TiO_2	–	–	0.210	–	–	–	–
Fe_2O_3	0.040	4.400	–	–	–	–	–
FeO	–	–	8.100	3.500	–	0.020	0.040
CaO	10.750	–	3.650	3.300	1.990	2.260	5.810
Na_2O	12.750	0.200	0.349	0.190	1.710	1.970	7.000
K_2O	2.020	7.400	0.031	0.050	0.200	0.050	0.200
Total	100.000	100.300	98.980	99.240	99.450	99.610	99.450

In this section LavAtmos results are compared to both experimental data and the results of other similar codes. In Figure 2.3 we compare the output of the LavAtmos code to that of the data gathered by Hastie and co-authors(Hastie et al. 1982a; Hastie & Bonnell 1985), with output from MAGMA (Schaefer & Fegley Jr. 2004), and output from VapoRock (Wolf et al. 2023) where available. Note that for the laboratory data no uncertainties were provided by the authors.

[2] `https://docs.scipy.org/doc/scipy/reference/generated/scipy.optimize.fsolve.html`

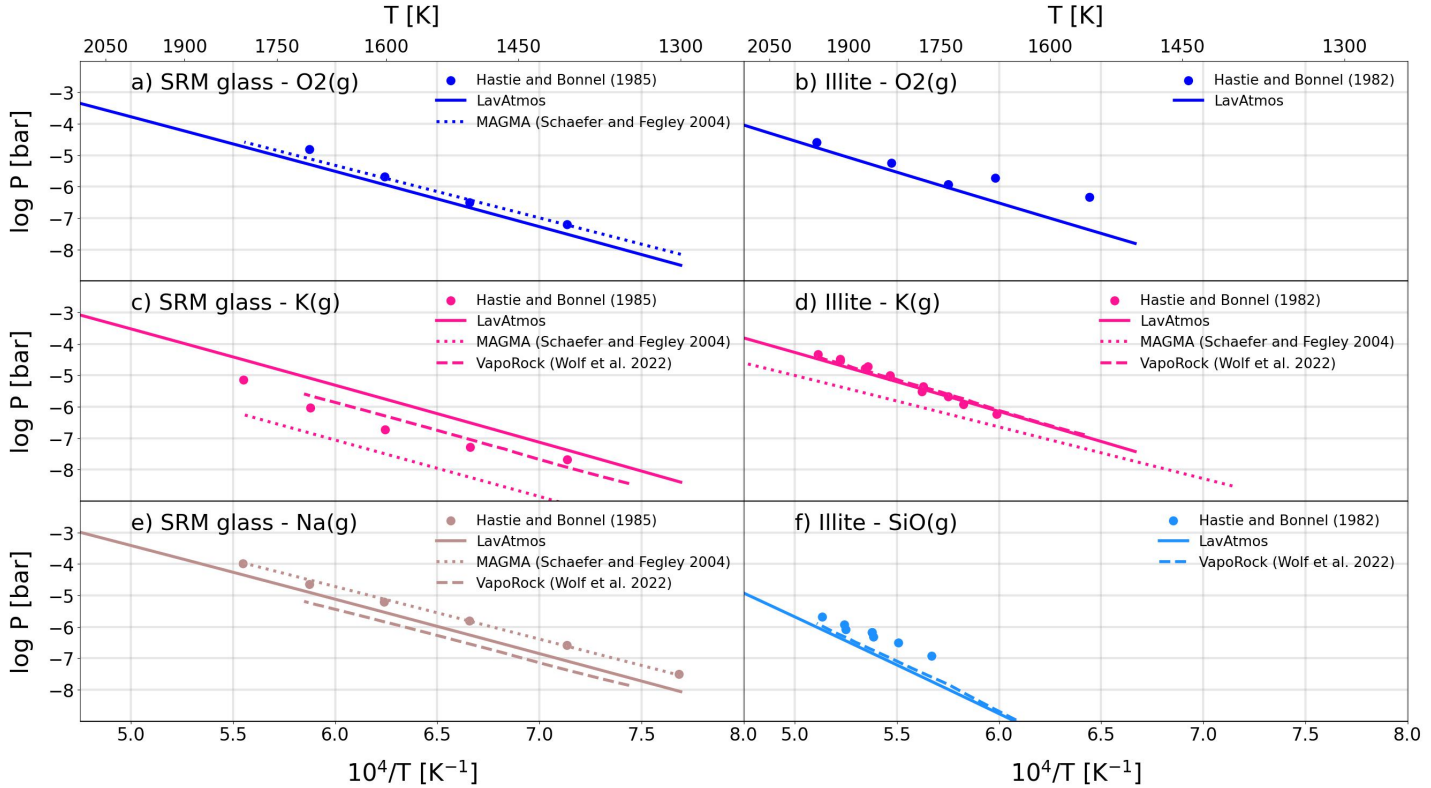


Figure 2.3: Comparison between data from Hastie and co-authors and code output - Each plot shows the partial pressure of a vapor species as experimentally measured by Hastie and co-authors Hastie et al. (1982b); Hastie & Bonnell (1985) (dots), calculated using LavAtmos (solid line), calculated using MAGMA (dotted line)Schaefer & Fegley Jr. (2004), and as calculated using VapoRock (dashed line)**?**. Plots a, c, show the results for SRM glass, while plots b, d, and f show the results for illite. The compositions of the melts are shown in Table **??**. Not all species had available data from all codes, hence some of the codes are missing in some of the plots.

In the panels on the left side of the figure (a, c, and e), the partial pressures of O_2, K, and Na above a synthetic (SRM) glass are shown. The bulk composition of this glass is given in Table 2.2. For O_2 we see that the results of both MAGMA and LavAtmos align well with the laboratory data. VapoRock is not compared in the O_2 plots due to it requiring fO_2 as an input (more on this below), for the calculation of the partial pressures of the other species VapoRock used the values given by Hastie and co-authors as input. For K the partial pressure predicted by LavAtmos and VapoRock differ by about a factor 2, with VapoRock lying closer to the experimental data. The partial pressures predicted by MAGMA lie about one order of magnitude below that of VapoRock. For Na it appears that MAGMA output falls closer to the laboratory data while LavAtmos and VapoRock slightly underestimate the Na partial pressures.

For Illite (see Table 2.2 for its bulk composition), on the right side of Figure 2.3 (b, d, and f), we see that the predicted partial pressure for O_2 is in agreement with the data at temperatures of 1750 K and above. We also see a much better agreement between the LavAtmos output and the data for K than we did for SRM glass, with VapoRock giving almost identical values while MAGMA tends to underestimate the K partial pressure by about a factor two at lower temperatures ($\tilde{1}$550K) and about an order of magnitude at higher temperatures (above 2000K). The partial pressure for SiO predicted by LavAtmos and VapoRock is very similar with both underestimating the experimental data by about a factor two.

Overall we find good agreement between the calculated partial pressures and the experimental data. We do recognize that this is a limited amount of data to which we are able to compare our output and that the lack of experimental uncertainties makes it difficult to quantify the results. The difference in the values predicted for the K partial pressures by MAGMA and LavAtmos is due to the difference in the thermodynamic models used by the two codes. As explained in previous work (Ito et al. 2015) where similar discrepancies with the MAGMA code were found in their MELTS-based calculations, the IMCC model (used by MAGMA to calculate activity values) is calibrated by experimental results on synthetic high-K_2O melts. This differs from MELTS, which is calibrated on experimental data drawn from natural, low-K_2O melts. This could also help explain why the K partial pressures predicted by LavAtmos appear to be closer to the experimental data for Illite (a naturally occurring composition) than for the SRM glass (synthetic composition). Another reason for the difference in partial pressures could be the much higher percentage of CaO and Na_2O in synthetic melts than in natural compositions. This would also explain why VapoRock is showing similar behavior to that of LavAtmos. The difference between the values calculated by LavAtmos and VapoRock are likely due to the different treatments of fO_2. We will elaborate further upon this below.

To illustrate the use of LavAtmos and compare with other codes, we mod-

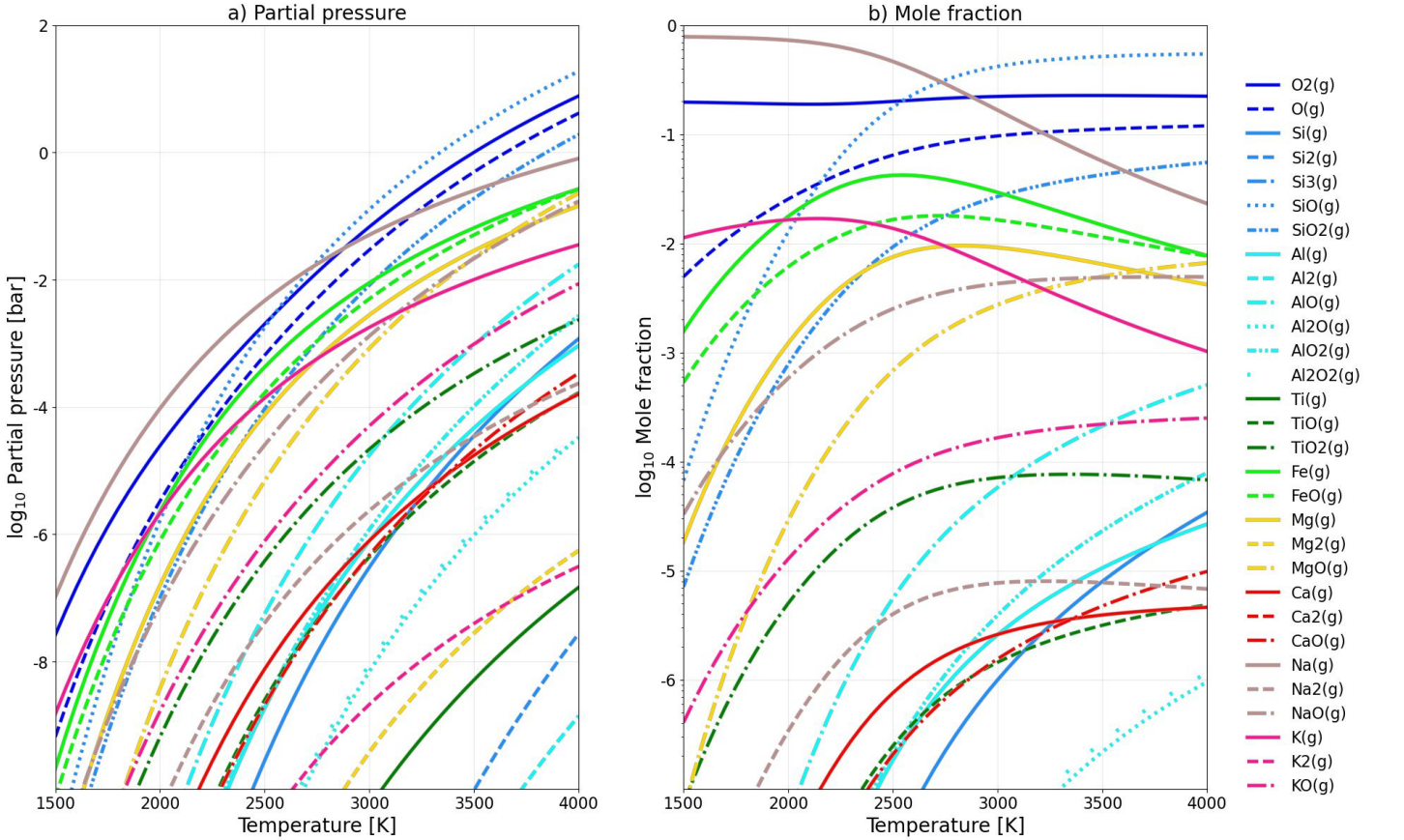


Figure 2.4: LavAtmos output for BSE composition between 1500 and 4000K - The left panel (a) shows the partial pressures and the right panel (b) shows the mole fractions (partial pressure divided by the total pressure) of the included vapor species. These calculations were done for a BSE composition (see Table 2.2). A surface pressure of 0.01 bar was assumed.

eled the vapour output for a bulk silicate earth (BSE) composition (see Table 2.2) at temperatures between 1500 K and 4000 K. The resulting partial pressures and mole fractions are shown in Figure 2.4. The dominant species up to about 2700 K is Na vapor, at which point SiO vapor takes over as the dominant species. O_2 and O have a strong presence as well throughout the majority of this temperature range. The general trend is that the more volatile species, such as Na, K, Fe, and Mg make up a larger fraction of the total gas pressure at lower temperatures than they do at higher temperatures. The opposite is true for the less volatile species, such as Si, Al, and Ti.

In Figure 2.5 we can see a comparison of a selection of the calculated mole fractions for a BSE composition (Table 2.2) as calculated by LavAtmos, Ito et al. (2015), and MAGMA (Visscher & Fegley 2013). The BSE composition used for the Ito et al. (2015) results differs slightly (a few decimal percentages) from the BSE composition used for the other calculations. Tests using LavAtmos however show that the difference is so small that the effects are negligible. Due to lack of details on the Ito et al. (2015) gas-melt equilibrium calculations we are not able to comment on differences in methodology. In Figure 2.6 we also show the corresponding total pressures. The partial pressures calculated by Ito et al. (2015) (a in Figure 2.5) are very close to the partial pressures calculated by LavAtmos. This is likely due to the fact that both codes make use of MELTS (Ghiorso & Sack 1995) to calculate the thermodynamic properties of the melt. In addition to potential differences in the approach, our calculations include a wider range of vapor species. When comparing LavAtmos to the MAGMA code (Fegley & Cameron 1987) data in recently published work (Visscher & Fegley 2013) (c in Figure 2.5) the most significant difference is between the calculated K partial pressures, as we also saw in Figure 2.3. As explained earlier in this section, this is due to the difference in calibration of the thermodynamic models used for the modeling of the liquid oxide activities (MELTS for LavAtmos and IMCC for MAGMA).

The total vapor pressures calculated for each code (Figure 2.6) show similar results. At lower temperatures it appears that LavAtmos and Ito et al. (2015) predict a lower total pressure than MAGMA. For higher temperatures MAGMA predicts a lower total pressure compared to the other two codes. Note that the mole fractions of the vapor species are calculated by normalizing the partial pressures by the total pressure calculated by the codes. Hence, if two codes have the same mole fractions as output for certain vapor species, this may not translate to the same partial pressure values depending on if the calculated total pressures are the same or not.

In Figure 2.7 we compare the output of LavAtmos (solid lines) with that of VapoRock (dashed lines) for 4 different compositions (see Table 2.2) as published in the work by Jäggi et al. (2021). VapoRock is a gas-melt equilibrium code that is also based on the thermodynamics calculated by MELTS. One of the ways in which this is apparent is the similar values calculated for the K partial pressures (pink) for all compositions. The greatest difference between

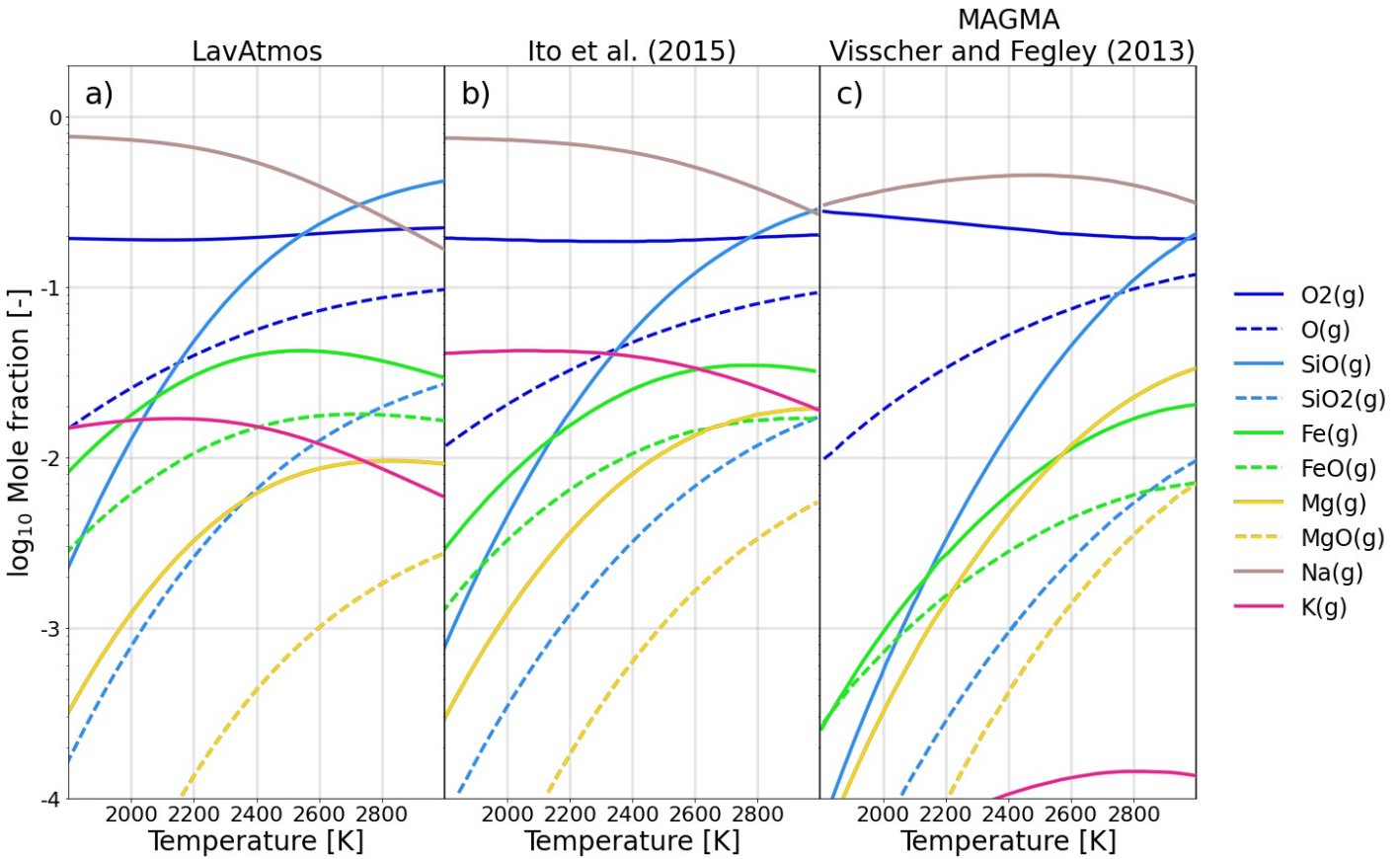


Figure 2.5: Comparison of mole fractions above a BSE melt as calculated by different codes - A selection of vapor species was made based on the data available in other works. The results shown are from LavAtmos (a), Ito et al. (2015) (b) and MAGMA as published in Visscher & Fegley (2013) (c).

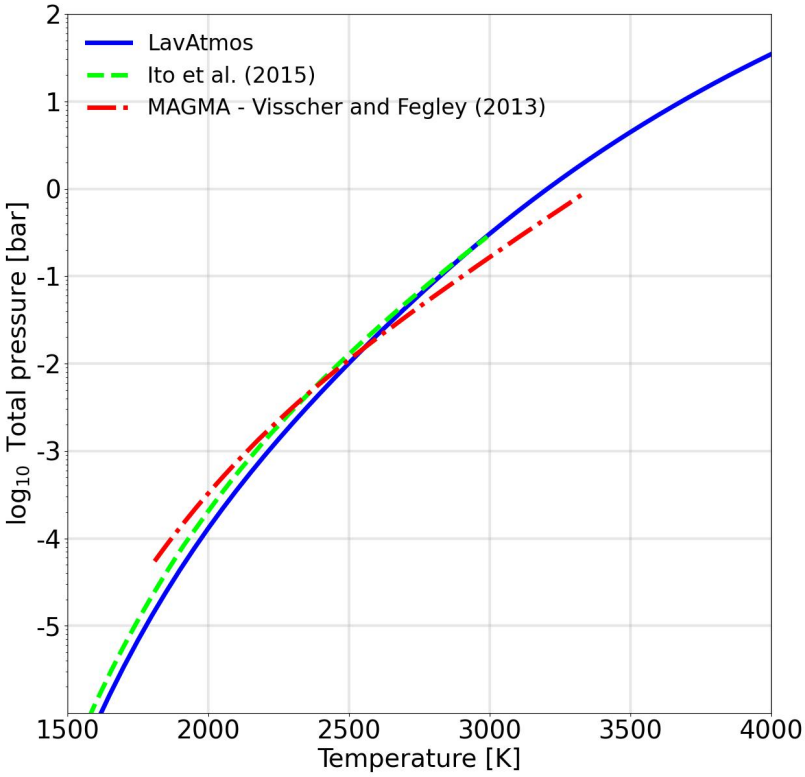


Figure 2.6: Total vapor pressures above a BSE melt as calculated by different codes - LavAtmos (solid dark-blue line), Ito et al. (2015) (dashed lime line), and MAGMA as published in Visscher & Fegley (2013) (dash dotted red line)

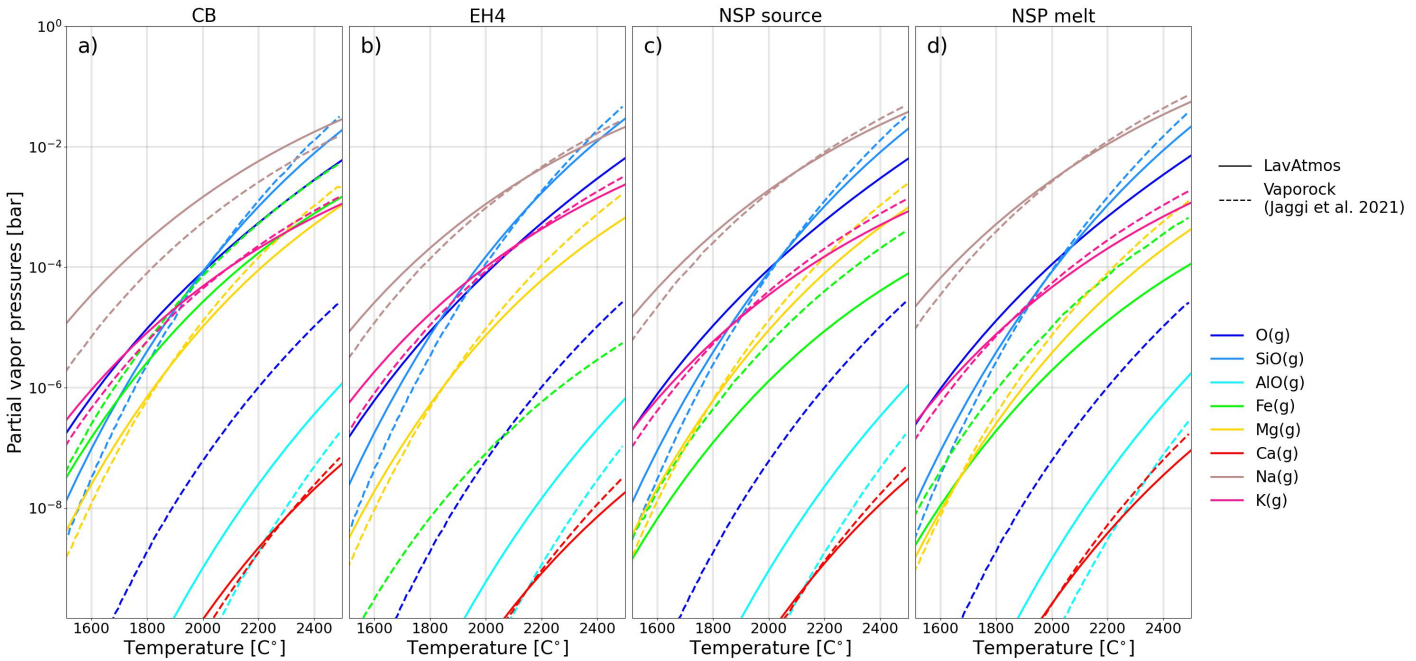


Figure 2.7: LavAtmos and VapoRock comparison - LavAtmos (solid lines) and VapoRock (Jäggi et al. 2021) (dashed lines) partial pressure output for a selection of species for melt compositions CB (a), EH4 (b), NSP source (c), and NSP melt (d). See Table 2.2 for the compositions.

the results of the two codes is seen in the values calculated for oxygen partial pressure. This can be attributed to the main difference in the approach taken by VapoRock and LavAtmos: the manner in which the oxygen fugacity of the system is determined.

For VapoRock, the oxygen fugacity of the melt is one of the user inputs (alongside temperature, pressure, and melt composition). For the results shown in Figure 2.7, and oxygen fugacity of IW-1 was used (Jäggi et al. 2021) (1 log unit less than the oxygen fugacity of the known iron-wustite buffer). This provides the user the option to fix the oxygen fugacity value to a certain value, or to test the influence of different oxygen fugacity values on the outgassing of the other species.

LavAtmos, however, does not take oxygen fugacity as an input and instead calculates it internally through the dual constraints of mass action and mass balance, similarly to MAGMA (Fegley & Cameron 1987; Schaefer & Fegley Jr. 2004), as shown in section 2.2 (equations 2.3 and 2.7). This allows the user to calculate a value for the oxygen fugacity based on the assumed congruent vaporization of the oxide species in the melt. As shown in Figure 2.3, this method is able to reproduce the oxygen fugacity values seen in experimental data. The same has been shown repeatedly for MAGMA (Fegley & Cameron 1987; Schaefer & Fegley Jr. 2004; Sossi & Fegley 2018).

VapoRock makes use of the thermodynamic data from the work done by Lamoreaux and co-authors (Lamoreaux & Hildenbrand 1984; Lamoreaux et al. 1987) and from the JANAF tables (Chase 1998), while LavAtmos sources its thermodynamic data from the JANAF tables only. Lamoreaux and co-authors found that the thermodynamic values that they found were in good agreement with those found in the JANAF database. Hence, we expect that this difference in approach does not have a significant impact on the results. VapoRock includes degassing of chromium species (Cr), while LavAtmos does not. We expect that future iterations of LavAtmos will also include this species.

2.4 Discussion

LavAtmos assumes that thermochemical equilibrium is reached. Hence, whenever applying this code to a system one should keep in mind whether or not the timescales of the system allow for chemical equilibrium to be reached (at least on a local level). Due to the high temperatures (> 1500 K) for which the code is meant, it can generally be safely assumed that an equilibrium state is reached at the surface of hot rocky exoplanets (Miguel et al. 2011; Ito et al. 2015).

The value of the oxygen fugacity is derived from the law of mass balance (see section 2.2). This assumes that the ratio of O atoms to cations must be the same in the out-gassed vapor as in the melt. This is a valid assumption if we assume that the system is dominated by the melt and that besides the vapor released from the lava, no other atmosphere is present. Figure 2.3 shows

that P_{O_2} values calculated using this method are in agreement with laboratory data.

The temperature range within which it is advised to use LavAtmos is between 1500 and 4000 K. For our method we assume that the planetary surface is fully molten (above liquidus temperature). The temperature at which a surface rock composition is fully molten varies strongly with composition and pressure as shown in the work by Hirschmann and co-authors (Hirschmann 2000) who illustrate the effects on melting behavior of typical terrestrial peridotitic mantle compositions by changing the alkali content or Mg/Fe ratio of the composition. It is estimated that the liquidus of terrestrial mantle peridotite at 1 atmosphere is around 1700 K based on extrapolation of higher pressure data (Zhang & Herzberg 1994). The liquidus temperature for the Earth's mantle at 1 atmosphere is estimated to be around 2000 K (Andrault et al. 2011). The liquidus of a basalt is down at around 1500 K (Cohen et al. 1967). Recently, it has been shown that elevated oxygen partial pressure can lower the basalt liquidus further (Lin et al. 2021). We therefore advise future users of LavAtmos to look into the estimated liquidus temperature of the composition for which to calculate degassing if a temperature below 2000 K is used. Below the liquidus temperature, crystals will form changing the composition of the magma away from the initial bulk composition. Thanks to the possibility of including mineral phases in MELTS (Ghiorso & Sack 1995), this limit may be removed in future work, with LavAtmos incorporating information about the thermodynamic properties of the melt as it cools, and changes in melt composition due to the crystallization of minerals.

As mentioned in section 2.2, the output of LavAtmos is pressure independent up to about 100 bar. Therefore, if the vaporization calculations are performed for a lava surface pressure below 100 bar, the default value of 0.1 bar can be used. If a surface pressure higher than 100 bar is expected, this should be specified to when calling LavAtmos. As mentioned before, higher pressures may change the liquidus temperature of the melt, something which should be kept in mind when selecting the temperature range for which the code is run.

The validation (section 2.3) with respect to laboratory data relies entirely on the data gathered by Hastie and co-authors (Hastie et al. 1982b; Hastie & Bonnell 1985). The first issue with this is the fact that no uncertainties were included in the published lab data. This has as consequence that the comparisons are mostly qualitative in nature. This makes it difficult to judge which of the tested codes is more representative of the experimental data. There are also only a limited number of vapor species for which partial pressure data is available. Besides the species for which data was published by Hastie and colleagues (O_2, K, Na and SiO), no suitable experimental data appears to be available for the remaining species to be compared to. We are aware of experimental data on the vaporization of two lunar basalt samples (de Maria et al. 1971). Nevertheless, due to uncertainties about changes in the bulk composition of these samples during the evaporation measurements, as well as the presence of iron

metal and reported interaction of oxygen with the capsule used to hold the samples (de Maria et al. 1971), we do not consider it appropriate to include these data in our comparison. This makes it difficult to judge the accuracy of the code in predicting partial pressures for which we do not have vaporization data.

Another source of uncertainty is that we are only able to compare our data to two different types of melt compositions (SRM glass and illite, see Table 2.2). More extensive lab measurements of gas partial pressures above complex melts of natural compositions are sorely needed.

2.5 Conclusion

We developed a open-source code for gas-melt equilibrium calculations that can be used to predict the composition of a vapor above a melt of a given composition and temperature. Thermochemical values are drawn from the JANAF tables (Chase 1998). The geothermodynamic code MELTS (Ghiorso & Sack 1995) is employed to model the thermodynamic activities of oxide species in the melt, which provides an approach based on more recent work than the IMCC model used by the MAGMA code. The P_{O_2}, necessary for determining the partial pressures of all other species, is determined self-consistently using the dual constraints of the laws of mass-action and mass-balance, which sets this code apart from VapoRock, which takes P_{O_2} as an input. We have shown that the output of the code is in line with the available lab data as well as other commonly used codes from literature. LavAtmos is applicable under the condition that one can assume that chemical equilibrium is reached, that no volatiles (e.g. H_2O, CO_2, N_2) are included in the melt, and within a temperature range of 1500 K and 4000 K.

With the new generation of telescopes allowing exoplanet research to push towards observations of the atmospheres of smaller planets (JWST, Ariel, ELTs), we hope that an open source lava-degassing code will be of use when interpreting spectra of planets potentially supporting lava oceans. Future work will involve including more volatile species so as to be applicable to a wider range of possible exoplanets.

Acknowledgements

This work was supported financially through a Dutch Science Foundation (NWO) Planetary and Exoplanetary Science (PEPSci) grant awarded to Yamila Miguel and Wim van Westrenen. We would like to thank Mark Ghiorso and Larry Grossman for discussions on the inner workings of the MELTS code, and the anonymous reviewers for their constructive comments on a prior version.

Data Availabilty

The code presented in this work is openly available on Github at https://github.com/cvbuchem/LavAtmos.git.

Appendix

2.A Deriving the partial pressure equation

For an equilibrium reaction of the type shown in equation 2.1, the relation between the chemical potentials (μ) of the liquid oxide species (j) and vapor species (i) involved can be written as:

$$c_{ij}\mu_j + d_{ij}\mu_{O_2} = \mu_i \tag{2.10}$$

The chemical potential of a species is given by:

$$\mu = \mu^\circ + RT\ln(a) \tag{2.11}$$

Where μ° is the standard chemical potential of the species, a is the activity[3], and R the gas constant. For ideal gasses at low pressures we assume that the activity is equal to the partial pressure of the gas. The chemical equilibrium constant for a reaction r at temperature T is given by:

$$\ln K_r = -\frac{\Delta_r G^\circ(T)}{RT} \tag{2.12}$$

Where $\Delta_f G^\circ$ is the difference in standard chemical potentials of the products and the reactants. Using this, equation 2.10 can be rewritten as:

$$c_{ij}\left(\mu_j^\circ + RT\ln(a)\right) + d_{ij}\left(\mu_{O_2}^\circ + RT\ln(P_{O_2})\right) = \mu_i^\circ + RT\ln(P_i)$$

Equation 2.12 can be rewritten as:

$$-\Delta G^\circ = \mu_i^\circ - c_{ij}\mu_j^\circ - d_{ij}\mu_{O_2} = RT\ln(K_{r_{ij}})$$

Which can then be substituted into the previous equation, giving us:

$$RT\ln(P_i) = RT\ln(K_{r_{ij}}) + c_{ij}RT\ln(a_j) + d_{ij}RT\ln(P_{O_2})$$

Which simplifies to equation 2.3.

[3] Activity is a term that indicates the effective concentration of a species. One can consider it as a measure of "how much" of a certain species is available for reaction.

3 Sensitivity of Dry Lava Planet Atmospheric Emission Spectra to Changes in Lava Compositions

Work in review **C. P. A. van Buchem**, R. Buddhacharya, M. Zilinskas, S. Zieba, Y. Miguel, W. van Westrenen, *Monthly Notices of the Royal Astronomical Society.* Reprinted here in its entirety.

Abstract

The atmospheres of hot rocky exoplanets are among the first primary targets of the JWST. Interpreting their atmospheric spectra requires understanding the link between silicate lava compositions and overlying atmospheres. We investigate the sensitivity of simulated emission spectra of dry lava planets to variations in oxide abundances in silicate melt. Our goal is to determine which molten surface features could be distinguishable with future observations. We combine our vaporisation code with gas chemical equilibrium and radiative transfer codes to self-consistently compute atmospheric chemistry and thermal structure. Alongside varying lava compositions, we assess the impact of host star spectral type on emission spectra. TiO_2 melt abundance dictates atmospheric TiO, which strongly influences surface temperature and emission spectra due to its short-wave opacity. This creates a degeneracy with heat redistribution efficiency, potentially broken by observing the optical TiO emission feature. Atmospheric SiO and SiO_2 abundances depend on melt SiO_2 content, with stronger SiO and SiO_2 emission features at higher melt abundances. For TiO_2 and SiO_2, these effects are at JWST's detection limit with six eclipses. Variations in alkali abundances could cause large surface pressure changes and influence the abundance of atmospheric SiO and SiO_2. Overall, melt composition has a limited impact on emission spectra, but some observable changes exist. TiO_2 and SiO_2 are the most influential species, with alkalis playing a minor role.

3.1 Introduction

Hot rocky exoplanets (HREs) serve as potential windows into rocky planet compositions and interiors. Their highly irradiated molten surfaces partially vaporise, significantly influencing the thickness and composition of the overlying atmosphere, providing a direct connection between their interior and their atmosphere (Léger et al. 2009; Henning et al. 2018; Boukaré et al. 2022). The composition of the atmosphere should therefore be strongly linked to the composition of the surface melt, an idea that has been the premise of a quickly growing body of theoretical and modelling work over the past years (e.g. Schaefer & Fegley Jr. 2004; Miguel et al. 2011; Ito et al. 2015; Kite et al. 2016; Nguyen et al. 2020; Zilinskas et al. 2022; Wolf et al. 2023; van Buchem et al. 2023; Seidler et al. 2024).

JWST has brought us from theory and modelling into an era where we can start inferring atmospheric compositions of rocky planets (Zieba et al. 2023; Hu et al. 2024). With many new observations on the way and the prospect on the horizon of additional measurements by the ELT and Ariel, it is key to understand how the compositions of lava oceans influence the atmospheric properties of HREs and the impact this has on the emission spectra we may observe.

To date, most previous work has assumed that the composition of day-side lava oceans is either equal to that of the bulk silicate Earth (BSE) (Palme & O'Neill 2003), or to a range of silicate melt compositions typically erupted on the surface of the Earth (e.g. Hans Wedepohl 1995; Schaefer & Fegley 2009; Miguel et al. 2011; Gale et al. 2013). Although this is certainly justifiable as a starting point, it is becoming increasingly clear that the compositional variability of rocky planetary crusts and mantles can be significantly larger than the range covered by these initial assumptions. Estimating the bulk composition of rocky exoplanets (Guimond et al. 2024) is an active area of research with estimates being made based on their measured density (Rogers & Seager 2010; Swift et al. 2011; Dorn et al. 2015), the compositions of their host-stars (Carter-Bond et al. 2012; Santos et al. 2017; Putirka & Rarick 2019; Putirka et al. 2021; Wang et al. 2022) and by analysing polluted white dwarfs (Klein et al. 2011; Bonsor et al. 2021; Putirka & Xu 2021; Xu & Bonsor 2021).

In addition, the bulk composition of a rocky exoplanet can only be assumed to be equal to the composition of surface lava if no interior differentiation has taken place - which is unlikely based on observations from our own solar system. Metallic core formation significantly depletes the silicate reservoirs of rocky bodies in iron and siderophile (iron-loving) elements (e.g. Hinkel & Unterborn 2018; Seidler et al. 2024). Subsequent crust-mantle differentiation can lead to surface compositions that differ substantially from mantle compositions (e.g. Lin et al. 2017; Hakim et al. 2019b,a). Temporal changes in melt composition can also take place due to chemical evolution of the melt as a result of the depletion of volatile melt species (Schaefer & Fegley Jr. 2004; Kite et al. 2016)

or due to crystal formation during lava cooling (Iezzi et al. 2008; Lichtenberg et al. 2021; Payacán et al. 2023).

Due to the large number of uncertainties and degeneracies surrounding the potential compositions of a surface melt, we investigate how deviations from the canonical BSE composition (Palme & O'Neill 2003) affect the atmospheres and spectral properties of HREs. In this work, we assume the HREs to be 'dry', by which we mean that we do not include any volatile species. Although recent work is pointing towards the possibility of HREs supporting volatile-rich atmospheres (Zilinskas et al. 2023; Piette et al. 2023; Hu et al. 2024), we limit the scope of this study to investigating the effect of varying individual oxide abundances in dry circumstances. This serves as a basis to compare with observations from JWST and other future efforts such as ELT and Ariel, and to identify, where possible, potential fingerprints in atmospheric emission spectra of specific compositional features of the lava underlying these atmospheres.

In the following section, we give a description of how we combined different thermochemical and radiative codes to produce self-consistent pseudo-2D emission spectra for a range of different star-planet system parameters and varying melt compositions. In section 3.3, we show the most relevant results out of the wide range of models that we ran, highlighting the potentially distinguishing features in the emission spectra. In section 3.4, we discuss the caveats and nuances that need to be taken into account when interpreting these results. Finally, we present our conclusions in section 3.5.

3.2 Method

The aim of this paper is to produce emission spectra for volatile-free HREs with a range of different surface melt compositions. In order to achieve this, we took an approach similar to that of Zilinskas et al. (2022):

1. **Determine the melt composition:** Using BSE (Palme & O'Neill 2003) as a starting point, we vary the abundance of each of the oxides in the melt, keeping the relevant abundances of all other melt components the same.

2. **Calculate the composition of the melt vapour:** The melt composition and an initial guess of the equilibrium temperature at the chosen point on the planet surface are given as input to our melt-atmosphere chemical equilibrium code LavAtmos (van Buchem et al. 2023). LavAtmos calculates the equilibrium chemical composition of the vapour coming from the melt. This is then converted to elemental abundances and passed on to the next step.

3. **Calculate the equilibrium gas chemistry over a grid of temperature-pressure (TP) values:** With the elemental abundances calculated in the previous step and a wide TP grid as input, we use the gas-phase chemical equilibrium code FastChem 3 (**?**) to calculate the gas chemistry over the entire grid.

4. **Iteratively determine a TP profile:** Star-planet system parameters and the gas-chemistry over the TP grid from the previous step are given as input to the radiative transfer code `HELIOS` 3 (Malik et al. 2017). `HELIOS` produces an atmospheric temperature-pressure profile.

   We then compare the surface temperature found by `HELIOS` with the initial surface temperature assumed for the melt-vapour calculation done in step **1**. If these values are not consistent with each other, we repeat step **1** using the newly calculated surface temperature as input. This loop is repeated until the surface temperature converges.

5. **Calculate the equilibrium gas chemistry over the final converged TP profile:** FastChem is used once more to calculate the equilibrium gas-chemistry along the final TP profile.

6. **Produce the emission spectrum:** We pass on the output of the chemistry and temperature structure to another radiative transfer code petitRADTRANS (Mollière et al. 2019), which we use to compute the final emission spectrum.

Following these steps allowed us to produce self-consistent 1D models of HRE atmospheres. In the remainder of this section, we explain how we varied the melt composition, the equilibrium chemistry of LavAtmos and FastChem, the radiative transfer codes `HELIOS` and petitRADTRANS, the pseudo-2D model that we used to produce the final spectra, and finally the different star-planet systems we tested.

3.2.1 Melt compositions

As explained in section 3.1, significant uncertainty remains about the extent to which lava compositions on the day-side of HREs can differ from a canonical BSE model. Hence, our aim is not to define likely compositions of the lava oceans of HREs but instead to investigate how deviating from the canonical BSE major element composition (Palme & O'Neill 2003) affects atmospheric composition, thermal structure, and emission spectra.

For each of the eight oxide components included in the canonical melt composition (SiO_2, MgO, Al_2O_3, TiO_2, FeO, CaO, Na_2O, and K_2O) we varied

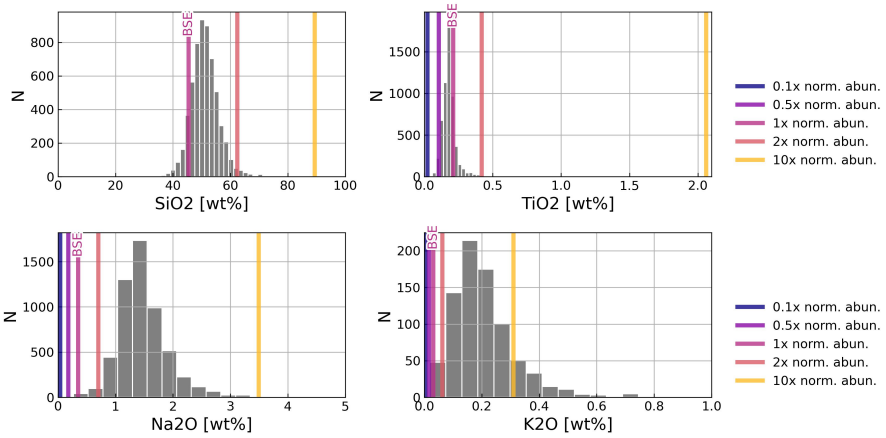


Figure 3.1: Abundance distributions derived from stellar compositions: Based on the work by Putirka & Rarick (2019), we plot the weight percentage distributions of the 4 most impactful melt oxides according to this work. These weight percentages were determined for hypothetical compositions based on the stellar compositions available in the Hypatia catalogue (Hinkel & Burger 2017). The vertical plotted lines represent the abundance ranges in weight percentage that we tested for each oxide, as detailed in the main text.

their original BSE abundance individually by factors 0.1, 0.5, 2, and 10 - spanning two orders of magnitude. The only exception was SiO_2, which was only modelled for x2 and x10 the BSE abundance due to MELTS (the underlying thermodynamics code used by LavAtmos - see section 3.2.2) not being able to run for compositions with low SiO_2 abundance.

Within the vaporisation code, given species abundances are normalized to 100 per cent. For example, when increasing the amount of SiO_2 in BSE by a factor of 10 from 45.4% to 454%, with all other percentages remaining equal to BSE values, the actual bulk composition that is used in the vaporization is renormalized to 89% (with a corresponding decrease of the other oxide species). These final normalised values are reflected in the values plotted in Figure 3.1. In Table 3.2, we provide an overview of the different weight percentages used for the melt oxide species that we tested as well as their normalized counterparts.

In Figure 3.1, we plotted the tested weight percentages for SiO_2, TiO_2, Na_2O, and K_2O alongside the distribution of 'bulk silicate planet'[1] compositions derived by Putirka & Rarick (2019) based on stellar compositions recorded in the Hypatia catalogue (Hinkel & Burger 2017). We selected these oxides due to them being the most impactful on the emission spectrum of HREs (see section 3.3). Figure 3.1 also shows that the tested oxide variations encompass all but a few of the expected edge cases for SiO_2 and K_2O. The biggest outlier is

[1] Bulk composition of a planet that excludes an iron-rich metallic core.

TiO_2, where the 10x abundance is 2.06% while the maximum value calculated by Putirka & Rarick (2019) is around 0.42%. Even so, we consider these abundances to be a conservative estimate of the extremes that could be reached in crust-mantle differentiation and in chemically evolved lava oceans, which we discuss in detail in section 3.4.1.

3.2.2 Equilibrium chemistry

In order to calculate the composition of the vapour above a melt for a given temperature (step **1**), we use our thermochemical equilibrium code LavAtmos (van Buchem et al. 2023)[2]. The partial pressure of any vapour above a melt can be calculated by solving the following equation:

$$P_{ij} = K_{r_{ij}}(T, P) a_j^{c_{ij}} P_{\mathrm{O_2}}^{d_{ij}} \tag{3.1}$$

Where P_{ij} is the partial pressure of vapour species i as formed in the vaporization of melt end-member species j, $K_{r_{ij}}$ is the temperature and pressure dependent chemical equilibrium constant of the corresponding vaporization reaction r, a_j is the activity of the melt end-member species, $P_{\mathrm{O_2}}$ is the O_2 partial pressure, and c_{ij} and d_{ij} are the stoichiometric coefficients necessary to balance the reaction. LavAtmos derives $K_{r_{ij}}$ for each reaction included from the thermodynamic data found in the JANAF database (Chase 1998). The activity a_j of each end-member species in the melt is calculated by using the geochemical code `MELTS` (Ghiorso & Sack 1995; Asimow & Ghiorso 1998; Ghiorso et al. 2002; Gualda et al. 2012; Ghiorso & Gualda 2015) through the ThermoEngine python wrapper[3]. Finally, LavAtmos solves for the O_2 partial pressure ($P_{\mathrm{O_2}}$) using the laws of mass action and mass balance as constraints. The included oxides are SiO_2, MgO, Al_2O_3, TiO_2, FeO, CaO, Na_2O, and K_2O.

Zilinskas et al. (2022) relied on published outputs of the `MAGMA` (Fegley & Cameron 1987; Schaefer & Fegley Jr. 2004) code to determine the vapour compositions above a melt. A key difference in the approach taken in this paper is the fact that using LavAtmos allows for far greater flexibility in testing different surface melt compositions. LavAtmos and `MAGMA` differ from each other mainly in the way in which the activities of the end-member oxide species in the melt are calculated. Instead of `MELTS`, `MAGMA` makes use of the Ideal Mixing of Complex Components (IMCC) model (Hastie et al. 1982b; Hastie & Bonnell 1985, 1986). This leads to some differences in calculated partial pressure (mainly for K); however, they generally agree well with each other, as shown in van Buchem et al. (2023).

Another recently published open-source vaporization code is VapoRock (Wolf et al. 2023). This works very similarly to LavAtmos by using `MELTS`

[2] A recently published update of the code (van Buchem et al. 2024) allows for the inclusion of volatile elements, but we focus the work in this paper on volatile-free atmospheres.

[3] https://gitlab.com/ENKI-portal/ThermoEngine

to calculate the activities of liquid oxide species in the melt and solving equation 3.1 for each included vaporization reaction. However, it treats P_{O_2} as a free parameter given as input by the user instead of constraining it using the laws of mass action and mass balance. A similar approach to this is also taken in the work by Seidler et al. (2024), who use an altered version of the `MAGMA` code that allows the fO_2 to be treated as a free parameter. The drawbacks of not constraining P_{O_2} using mass action and mass balance are twofold. First, imposing a P_{O_2} value other than that which satisfies mass action and mass balance, means that oxygen is being added or removed from the system - depending on if its partial-pressure is higher or lower than the value that satisfies these constraints. Second, it does not allow for P_{O_2} to change self-consistently as the composition of the melt evolves. With LavAtmos, we can consistently account for these changes when testing different compositions.

In Seidler et al. (2024) it is argued that the approach taken to calculate P_{O_2} in `MAGMA` and LavAtmos is only valid if all possible vaporisation reactions that could release O_2 are taken into account and if the set of melt components and their thermodynamic properties is complete and accurate. For the nine included end-member components of the melt, LavAtmos includes 30 of the most important vaporisation reactions, of which 26 involve O_2 (van Buchem et al. 2023). At 4000 K for a BSE melt composition, the partial pressure of the least abundant vapour species (Al_2) is just above 1e-9 bar, while the partial pressure of O_2 is just under 1 bar. At colder temperatures, the difference between these partial pressures grows further. Including the vaporisation reactions of the less abundant vapour species would likely not significantly alter the calculated O_2 partial pressure. Similarly, including a greater number of refractory oxide species in the thermodynamic melt model would likely only have a marginal impact on the O_2 partial pressure. Concerning the accuracy of the thermodynamic properties, we agree that this is something that should be looked into - however, since both Vaporock and `MAGMA` also make extensive use of the JANAF tables, this issue is not unique to LavAtmos. Hence, in our view, LavAtmos provides an approximation of the vapour composition that is accurate enough for the work presented in this paper.

In order to isolate the effect of changing oxide abundances on the atmospheres and resulting emission spectra of HREs, we do not consider the effect that the presence of volatiles in a melt may have on vaporisation. We assume that no volatile elements (eg. H, C, N, S, and P) are present in either the atmosphere or the melt.

As explained prior, the chemical composition of the melt vapor is converted to elemental abundances and passed on to the gas chemical equilibrium code FastChem 3 (Stock et al. 2018, 2022; Kitzmann et al. 2024), which is used to calculate the gas-chemistry of the atmosphere. Initially, this is done over a temperature-pressure grid (step **2**) and then again over the final TP profile (step **4**). The majority of the thermal data used by FastChem 3 for this work is from Chase (1998), see the appendix of Kitzmann et al. (2024) for a full

Table 3.1: Overview of tested star-planet systems: For each spectral type, generic stellar values were used. The orbital distance of each of the planets was determined such that the substellar equilibrium temperature is 3000 K. The planets all have the same assumed radius of 1.5 R_{earth}.

Spectral type	M_{star} [$M_\odot$]	R_{star} [$R_\odot$]	T_{star} [K]	Orbital distance [AU]
F	1.3	1.23	6000	2.29e-2
G	1.0	1.00	5778	1.73e-2
K	0.8	0.84	4500	8.75e-3
M	0.5	0.57	3500	3.64e-3

list of sources. Although included in FastChem 3, we have not made use of the condensation due to the fact that the temperatures at all pressure of our models are above 1900 K - which is greater than the point of condensation for all the included gas species (Kitzmann et al. 2024). If this work were to be repeated for colder planets or non-inverted atmospheres, then condensation would likely start to play a major role.

3.2.3 Star-planet systems

For all of the models, we assume that the planet is $\simeq 1.5$ R_{earth}. We tested four star-planet systems, each with a star of a different spectral type (F, G, K, and M). For each system, we placed the planet at an orbital distance from the star that corresponds to the distance at which the equilibrium temperature at the substellar point is equal to 3000 K. This was determined using:

$$d_{\rm orb} = R_{\rm star} \left(\frac{T_{\rm eq}}{T_{\rm star}} \right)^{0.5} \tag{3.2}$$

Where R_{star} and T_{star} are the radius and temperature of the host star and T_{eq} is the desired equilibrium temperature. For the G type star, we chose to use the equilibrium temperature and mass of the sun, while for the other three, we used representative temperatures and masses of each spectral type. We used a standard mass-radius relationship of $R_{star} \propto M^{0.8}$ (Kippenhahn et al. 2012) to determine the radius of the stars. An overview of the system parameters we used for each spectral type is given in Table 3.1.

Stellar types hotter than F type star ($T_{star} > 7300$ K) are not included in this work. This is due to the apparent rarity of HREs orbiting such stars, with only two detections to date (Charpinet et al. 2011; Morton et al. 2016), and the planet to star flux ratio that is obtained from these systems[4] is too low to

[4] About 2 ppm at 1 μm and 30 ppm at 20 μm for a 1.5 R_{earth} planet at an orbital distance

be able to observe accurately with current generation telescopes.

3.2.4 Radiative transfer

In order to calculate the TP profiles of the tested atmospheres (step **3**), we used the radiative-transfer code HELIOS (Malik et al. 2017, 2019; Whittaker et al. 2022). As in Zilinskas et al. (2023), these TP profiles were self-consistently calculated with the output of FastChem and LavAtmos, such that the final surface temperature is consistent with the overall atmospheric chemistry. As explained in step **4** at the start of the methods section, this is achieved by iterating until the surface temperature used to calculate the vapour composition is the same as the temperature at the bottom of the TP-profile.

In all cases, we used the standard diatomic adiabatic coefficient $\kappa = 2/7$ for convective adjustment. For our opacities, we used all of the atomic and molecular species that are included in our melt compositions. This includes atoms Al, Ca, Fe, K, Mg, Na, Si, Ti, as well as molecular species AlO, CaO, MgO, O_2, SiO, SiO_2, and TiO[5]. The line lists were kept the same as in (Zilinskas et al. 2023), with atomic species using the Vienna Atomic Line Database (VALD3) (Ryabchikova et al. 2015) and the molecular species from a range of sources. All of the line lists that we used and their corresponding sources can be found in Table 3.3. Note that these opacities were sourced from the DACE[6] database or calculated using HELIOS-K (Grimm & Heng 2015; Grimm et al. 2021). In Figure 3.13, we show the unweighted opacities of some of the most important atmospheric species.

We used the `PHOENIX` models (Husser et al. 2013) to calculate the stellar spectra for each of the F, G and K spectral types. Just as in Zilinskas et al. (2023), we combined the `PHOENIX` spectrum for an M type star with scaled shortwave `MUSCLES` spectra (France et al. 2016; Loyd et al. 2016; Youngblood et al. 2016) so as to accurately model the increased shortwave emission seen in cooler stars. See Figure 3.14 for a side by side comparison of the included stellar spectra.

For step **6**, we pass the output of the chemistry and temperature structure to `petitRADTRANS`[7] (Mollière et al. 2019, 2020), which we use to compute the final emission spectrum. Where possible, the opacity line lists were kept the same as in `HELIOS`, but the opacities themselves were obtained from ExoMol[8] pre-packaged correlated-k tables (Chubb et al. 2021). All of the spectra were calculated using the low-resolution mode of $\lambda/\Delta\lambda = 1000$, with a wavelength range of 0.3 – 28 µm.

of 4.44e-2 AU (equivalent to a substellar equilibrium temperature of 3000K) for a BSE vapour only atmosphere.

[5] Although FeO is abundant in lava-vapour atmosphere, there are currently no available line lists for this molecule and is therefore not included in the radiative transfer model.

[6] https://dace.unige.ch/

[7] Version 2.7.6

[8] https://www.exomol.com/

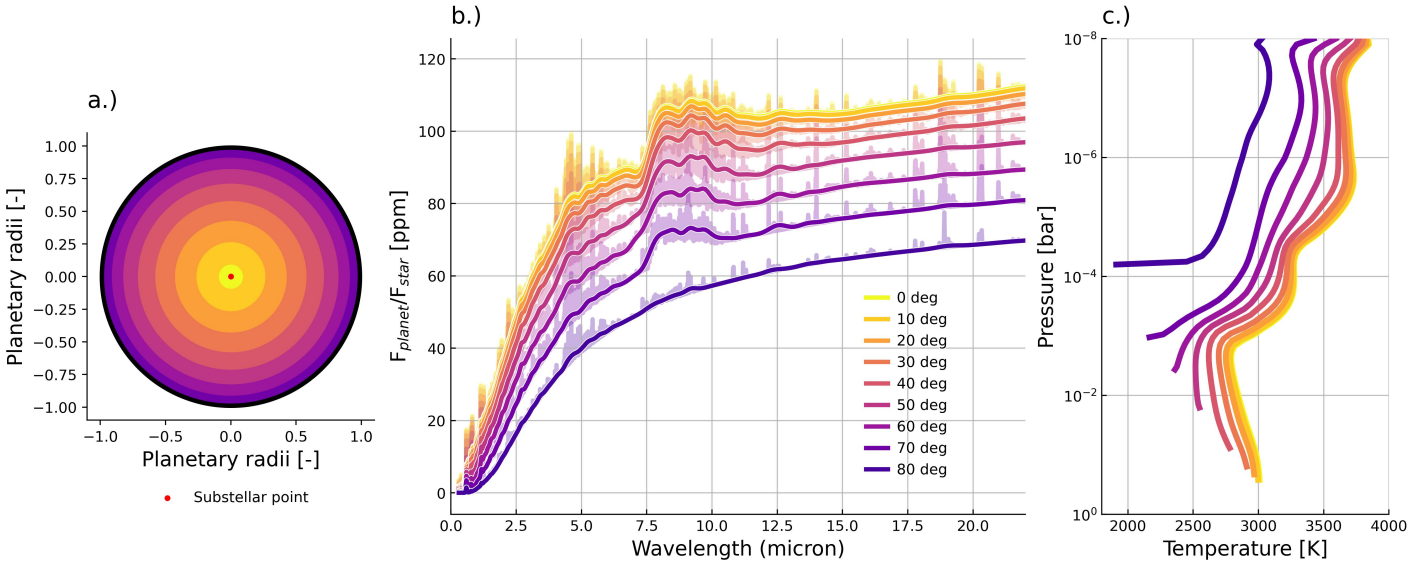


Figure 3.2: Pseudo-2D atmosphere model: Panel a.) shows the area from which light is emitted from different angles of separation from the substellar point (shown using a red dot). In panel b.) we show the different spectra that are calculated for each of the different rings. Panel c.) shows the TP profiles for each ring, illustrating how the surface temperature (the bottom of the profile) decreases with increasing distance from the substellar point.

3.2.5 Pseudo-2D model

In order to alleviate some of the drawbacks of modelling thermal emission from a 3D object using a 1D approach, as previously done in Zilinskas et al. (2022, 2023), we expanded our method to a pseudo-2D approach. This was first used in Zieba et al. (2022) to model the atmosphere of the planet K2-141 b and has since then also been used to rule out a melt vapour-only atmosphere for 55-Cnc e in Hu et al. (2024).

In Figure 3.2, we illustrate how this approach works in detail. We calculate the 1D emission spectrum at 10° intervals moving away from the substellar point (panel *a* in Figure 3.2). Moving away from the sub-stellar point increases the zenith angle, leading to less stellar irradiation hitting the surface of the planet, hence, lowering the surface temperature. This is demonstrated in panel *c*. The spectra calculated at each angle are then weighted according to the surface area covered by each interval and summed, giving a single averaged spectrum of the entire day-side of the planet. This approach allows us to take into account how melt vapour composition changes as a function of surface temperature and the effect that this has on the spectral features in the emission spectrum.

In Figure 3.15, we show a comparison between this approach (shown in light blue) and another commonly used approach of using a day-side averaged temperature estimation (shown in orange). The comparison was made using a bulk silicate earth (BSE) composition (Palme & O'Neill 2003) around a G type star. In this comparison, we can see that the pseudo-2D approach leads to slightly less pronounced features and a slight increase in the continuum spectrum, most notably at wavelengths beyond 5 μm (panel *b*).

3.3 Results

As explained in section 3.2, we produced models for F, G, K, and M type stars, varying the melt oxide abundances of SiO_2, MgO, Al_2O_3, TiO_2, FeO, CaO, Na_2O, and K_2O. We found that the melt species that had the strongest influence on the temperature-pressure profile and emission spectrum of a generic HRE with a substellar temperature of 3000 K are TiO_2 and SiO_2. This is covered in detail in the following subsections of this paper along with some tentative indications that Na and K could also play a potentially observable role in HRE emission spectra and TP profiles. For the remaining species, however, varying their abundance in the melt oxides did not lead to any significant effects on the shape of the emission spectra and TP profiles and are therefore not shown in the results.

Before delving into the results, we first devote a subsection to analysing in detail the temperature-pressure and chemical structure as well as the opacity contributions and the resulting emission spectrum of a BSE atmosphere for a G-type star with an equilibrium temperature of 3000 K. This will help explain and interpret the results in the following sections.

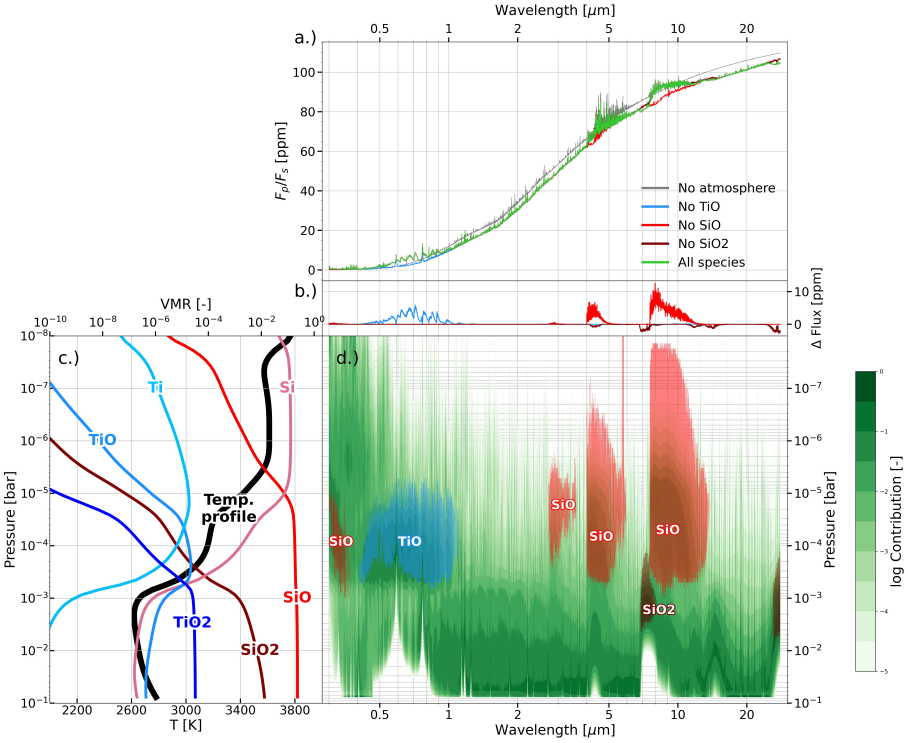


Figure 3.3: Overview of a vapour atmosphere: Each of these panels represent different aspects of a vaporised atmosphere above a BSE melt for a G-type star at 40° from the substellar point. In the top panel (a) we compare the emission spectrum when including all species (green) with cases where a single specified opacity is excluded. The panel below that,(b), shows the difference in ppm between the spectrum containing all species and the ones with the opacity of one species removed. The bottom left panel (c), contains both the temperature-pressure profile of the atmosphere (in black) as well as the VMR of a few keys species in the atmosphere. Finally, in the bottom right panel (d)) the contribution to the emission as function of pressure and wavelength is visualised. We highlighted the regions where the contribution from key species is most prominent.

3.3.1 The anatomy of a BSE vapour atmosphere

To understand how a changing melt and atmosphere composition affects the emission spectrum of an HRE, it is useful to first visualise where the emission originates in the atmosphere. In Figure 3.3, we show the chemistry, the emission spectrum, and the contribution function of a rock vapour atmosphere above a melt with a BSE composition. For this model, we assumed the same parameters as that of a planet orbiting a G-type star (see Table 3.1). We assume incident irradiation equivalent to that at 40° away from the substellar point due to this resulting in similar temperatures as the averaged temperature of a pseudo-2D model (see Section 3.2.5).

In the top panel (*a*) of Figure 3.3, we show the calculated emission spectrum for the case with no atmosphere (grey), an atmosphere containing the full list of species (green, see Table 3.3 for details on each species), and three spectra calculated with a single species omitted - TiO, SiO, and SiO_2 (blue, red, and maroon respectively). In order to highlight the changes in flux when removing these species from the opacities, we added a panel below (*b*) in which we plot the difference in ppm between the spectra. It should be noted that for the spectra with the omitted species, we only left out the opacity of these species when calculating the emission spectrum using petitRADTRANS (step **6** in Section 3.2), so the temperature-pressure profile was calculated assuming the presence of all species and remains the same. The leftmost panel (*c*) contains both the temperature-pressure structure of the atmosphere (in black, x-axis located at the bottom), as well as the volume mixing ratios (VMR) of a selection of atmospheric species (coloured, x-axis located at the top). The panel to the bottom right (*d*) shows the opacity contribution as a function of wavelength and pressure. Regions with especially strong contributions from SiO, SiO_2, and TiO are highlighted (red, maroon, and blue respectively).

Looking at the spectrum for the case with no atmosphere in panel *a*, we see that including an atmosphere leads to an overall decrease in flux. This is due to the major emitting region (also known as the photosphere) in the model containing an atmosphere being located in a region of the atmosphere (between 1e-1 and 1e-2 bar) which has a lower temperature than the surface. Similarly, the SiO_2 features around 7 μm show up as absorption features in the spectrum due to originating from a relatively colder part of the atmosphere - coinciding with 1e-3 bar, the lowest temperature region of the atmosphere.

As we go beyond this point to higher altitudes and lower pressures around 1e-4 bar, TiO and SiO become the spectrally dominant species. As explained in Gandhi & Madhusudhan (2019), thermal inversions occur in atmospheres where

$$\kappa_{\rm vis}/\kappa_{\rm ir} \gtrsim 1 \tag{3.3}$$

Where κ_{vis} is the average opacity in the optical wavelength range (between about 0.1 and 1 μm) and κ_{ir} the average opacity in the infrared (beyond $\simeq$ 3μm). Looking at the contribution plot (panel *d*), we see a strong increase in

the opacity in the optical, which, despite the SiO opacity contribution in the infrared, is enough to satisfy the criterion in equation 3.3, leading to a thermal inversion. The presence of a thermal inversion allows for emission features in the spectrum (Gandhi & Madhusudhan 2019), which we see clearly for TiO around 0.7 μm and for SiO at 3, 4.5, and 8 micron. Going up further into the atmosphere, the opacity contribution of these species decreases, coinciding with the decrease in their abundance at lower pressures, as can be seen by comparing panel *c* to panel *d*. The more complex species disassociate into their atomic counterparts with increasing temperature and decreasing pressure.

Thanks to the strong influence on both the thermal structure of the atmosphere and the emission spectrum of SiO, SiO_2, and TiO, we find that varying the abundance of SiO_2 and TiO_2 in the melt has a significant effect on the emission spectra of HREs. This is covered in detail in the following subsections. Besides the aforementioned species, there are a few other species that may have an observable effect on the emission spectrum of HREs (Zilinskas et al. 2022). However, we find that only Na and K could potentially lead to some observable changes if their corresponding melt end-member species (Na_2O and K_2O) are changed. This is explored in the final subsection of the results.

3.3.2 TiO_2 variation

In Figure 3.4, we show how varying the TiO_2 melt abundance affects the VRM of TiO throughout the atmosphere for a planet orbiting a G-type star[9]. The change in VMR of TiO at a given pressure is almost in linear relation to the change in abundance of TiO_2 in the melt. However, we do see a decrease in surface pressure as a result of decreasing surface temperature. In Figure 3.5 we show in detail how a varying TiO_2 melt abundance affects the emission spectrum (panels in the left column), and the temperature pressure profile (panels in the right column) for F, G, K, and M type stars. The temperature profiles shown are those calculated at a 40° angle away from the sub-stellar point as they were deemed most representative of the average dayside (see Figure 3.2). To allow for a clearer visualization of the differences in the spectra, we added a panel below panels containing the emission spectra showing the difference in flux between the spectra calculated using the BSE (indicated with the '1 x TiO_2' label) composition and those with varying levels of TiO_2.

The behaviour of the emission spectra and TP profiles is qualitatively similar for planets orbiting F-, G-, and K- type stars, which we will describe first, after which we will focus on the results of planets orbiting an M- type star. Changing the TiO_2 melt abundance - and as a result the TiO atmospheric abundance - of these planets has a significant effect on both the temperature-pressure profile of the atmosphere and its emission spectrum. The two most notable effects are 1) a significant decrease in the surface temperature and 2) an

[9]The relative behaviour of TiO shown in Figure 3.4 is representative for the behaviour of F-, K- and M- type stars as well.

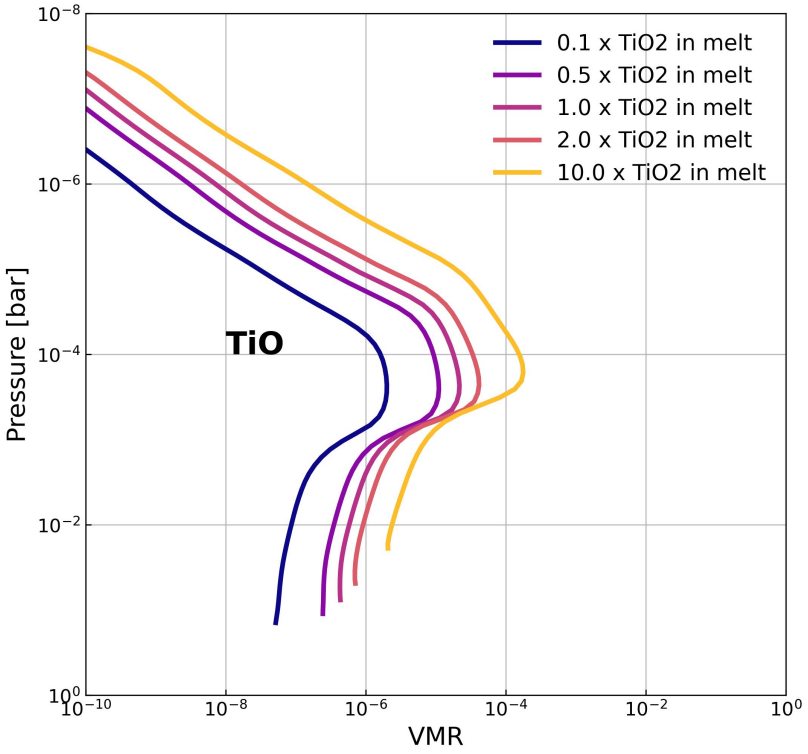


Figure 3.4: Atmospheric TiO changing with TiO_2 melt abundance: Shown for a planet orbiting a G-type star (see Table 3.1 for parameters). The TiO_2 abundance in the melt was changed with respect to the BSE abundance (see Table 3.2).

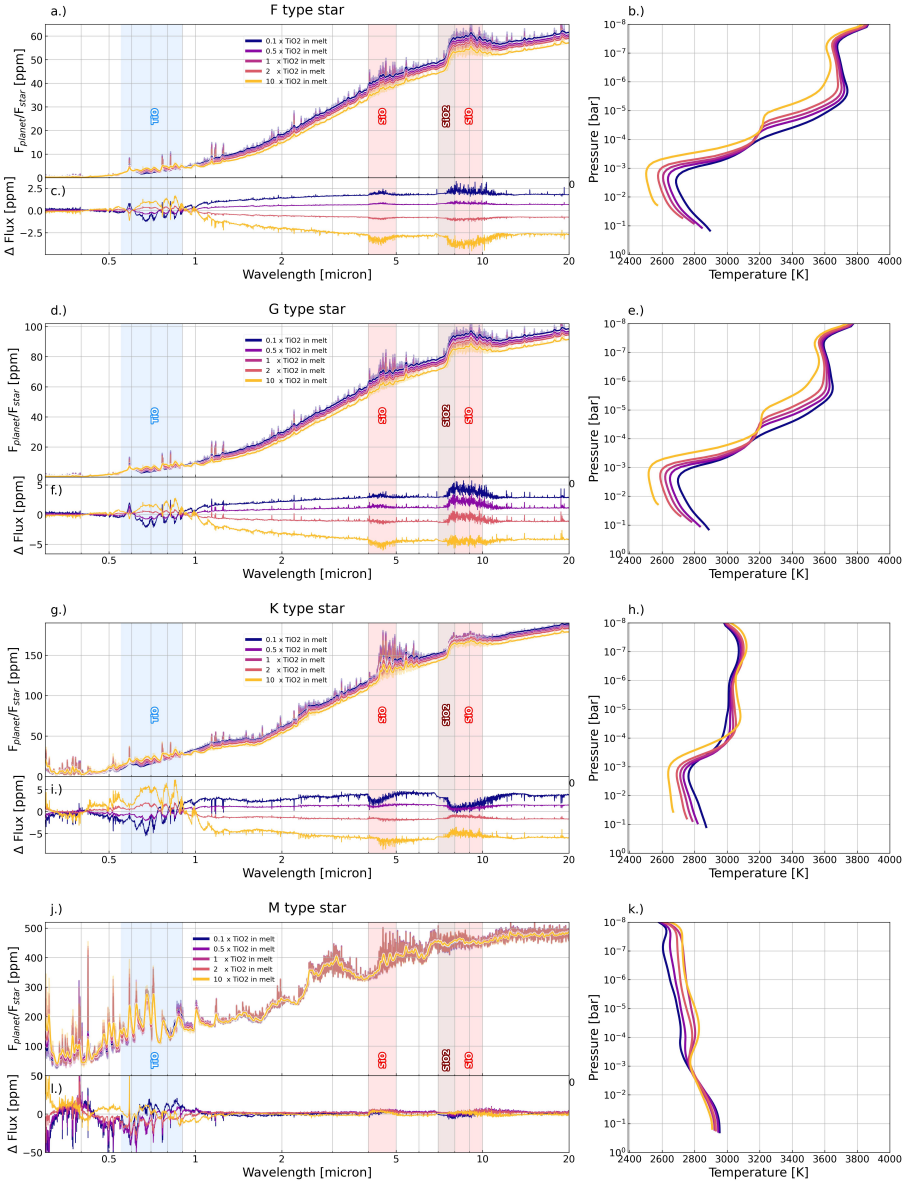


Figure 3.5: Effect of varying TiO_2 melt percentage on emission spectra - For an F-, G-, K-, and M-type star we show the calculated pseudo-2D emission spectra and TP profiles for different TiO_2 melt abundances. Under each spectrum we also plot the differences in flux between the different spectra with respect to 1 x TiO_2 melt (which is the same as a BSE composition). The TP profiles shown are those for the models calculated at a 40° angle away from the substellar point. Note the difference in the scales of the y-axes of the emission spectra for the different stellar types.

increase in the size of the TiO emission features (highlighted in blue in Figure 3.5).

The decrease in surface temperature, from around 2900 K to 2550 K for the F- and G-type stars and from 2850 to 2650 K for K-type stars, is due to the increase in TiO abundance leading to an increase in the opacity of the atmosphere in the optical wavelengths (see panel *d* in Figure 3.3). This allows less of the stars irradiation to reach the planet's surface, decreasing its temperature, leading to a significantly lower flux being emitted from the planet, as is shown in panels *c*, *f*, and *i*, where we see a decrease in flux of up to 5 ppm in the infrared (with respect to the BSE case) for a 10x increase in TiO_2 abundance.

In the upper atmosphere, however, the temperatures converge again up around 3900 K. Hence, as the TiO_2 melt abundance (and the TiO atmospheric abundance) increases, the size of the temperature inversion increases as well. Looking back at equation 3.3, we see that this is what one would expect for an increase in the opacity in the optical wavelength range. The result of the strengthening of the temperature inversion and increasing TiO atmospheric abundance with increasing TiO_2 melt abundance, is that even with an overall decrease in flux, the TiO emission features grow.

Comparing the low TiO_2 abundance TP profiles with their high abundance counterparts for F- and G- type stars also shows that in atmospheres with abundant TiO_2 the TP profile becomes almost isothermal between 1e-4 and 1e-5 bar - which coincides with the pressures with the highest TiO abundance (see Figure 3.4) and also the pressures from which the greatest opacity contribution in the optical is located (see Figure 3.5).

All of the changes to the emission spectrum and temperature pressure profile caused by varying the TiO_2 abundance, are due to the changing absorption of irradiation within the optical. Hence, the spectra of planets orbiting F- and G-type stars, which emit the majority of their energy in the optical wavelengths (see Figure 3.14), are affected more than for cooler K-type stars. This is most visible in the temperature pressure profiles in Figure 3.5. Those calculated for K-type stars have far weaker thermal inversions and are close to isothermal above 1e-4 bar. This trend of decreasing thermal inversion strength was also found for hot-Jupiters by Lothringer & Barman (2019) and was also shown for HREs in Zilinskas et al. (2022). What should be noted though, is that the planet to star flux ratio is higher for cooler/smaller stars, hence the differences in the size of the TiO_2 emission features are greater than that of hotter stars, reaching up to 5 ppm, despite the smaller temperature inversion.

Looking at the spectrum of a planet orbiting an M-type star in the bottom row of Figure 3.5, we see that varying TiO_2 melt abundance does not seem to have a very significant effect on the emission spectrum or TP profile of the planet. This is due to the fact that the emission peak of M-type stars is shifted so far to the red (see Figure 3.14) that the high opacity of TiO in the optical does not block as significant an amount of the radiation as for the hotter stars.

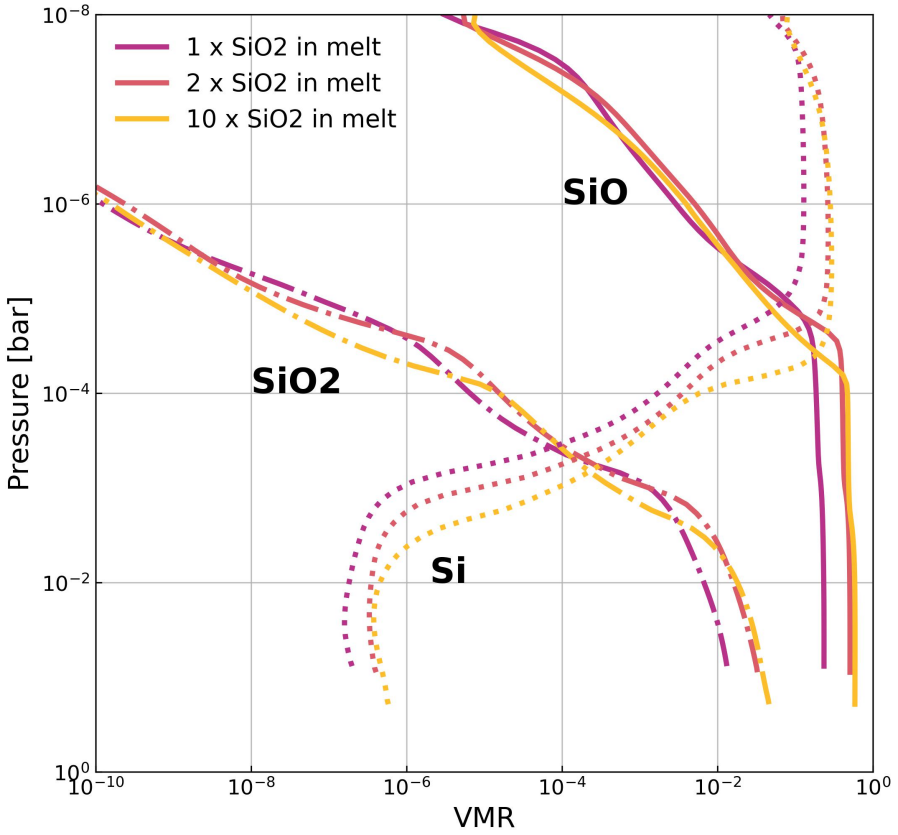


Figure 3.6: Atmospheric SiO and SiO_2 changing with SiO_2 melt abundance: Shown for a planet orbiting a G-type star (see Table 3.1 for parameters). The SiO_2 abundance in the melt was changed with respect to the BSE abundance (see Table 3.2).

Hence, the surface temperature is not affected as strongly and the overall flux level remains about the same for all TiO_2 melt abundances. Furthermore, the relatively small temperature inversion and generally lower temperature of the atmosphere leads to far less prominent emission features, making it more difficult to discern the planetary atmosphere features from the features in the stellar spectrum.

3.3.3 SiO_2 variation

As mentioned in section 3.2, we were not able to model a decrease in SiO_2 abundance in the melt composition due to `MELTS` not being able to run for compositions with low SiO_2 abundance. In Figure 3.6 we show the VMR of the

most important Si species in the atmosphere of a G-type star at 40° degrees away from the substellar point. In contrast to varying TiO_2 melt abundance and its effect on TiO atmospheric abundance, increasing SiO_2 melt abundance does not lead to an increase of SiO or SiO_2 throughout the entire atmosphere. Lower in the atmosphere (at higher pressures) an increase in SiO_2 melt abundance does lead to an increase in SiO and SiO_2 atmospheric abundance. However, as we can see in panel *e* (the TP profile of the planet orbiting a G-type star) in Figure 3.7, the changing melt composition affects the TP profile such that there is an increase in temperature with increasing SiO_2 beyond 1e-2 bar. This temperature increase is enough to cause SiO and SiO_2 to start dissociating into Si lower in the atmosphere. This causes the SiO and SiO_2 VMRs to be about equal for all melt abundances at pressures below 1e-3 and 1e-5 bar respectively. SiO and SiO_2 have the greatest amount of opacity contributions at greater pressures, so the spectra of these atmospheres still see significant changes.

Increasing SiO_2 melt abundance leads to an increase in surface temperature for the planets around all four tested stellar spectral types. The temperature increase is caused by a relative decrease in TiO_2 in the melt as SiO_2 melt abundance is increased. SiO_2 makes up such a large fraction of the total melt composition ($\simeq$ 45% in BSE), that changing its abundance also significantly affects the abundances of the other melt species. The resulting decrease in TiO_2 abundance leads to an increase in temperature similar to that seen in the previous section where we decreased TiO_2 melt abundance directly.

Increasing the abundance of SiO_2 in the melt causes the temperature inversion to take place at higher atmospheric pressures. This is due to a combination of: 1) higher surface temperatures, 2) an increase in IR opacity due to more abundant atmospheric SiO_2 and SiO, and 3) a decrease in the optical opacity with less abundant atmospheric TiO. For the planets orbiting the F-, G-, and K-type, this moves the thermal inversion from around 1e-3 bar to around 1e-2 bar for a 10x increase in SiO_2.

This change moves the temperature inversion from a region in the atmosphere above the SiO_2 opacity contribution to a region below it (see Figure 3.3), turning the SiO_2 absorption feature between 7 and 8 μm into an emission feature. This indicates that detecting an SiO_2 emission or absorption feature in the emission of an HRE could constrain the pressure/altitude at which a thermal inversion takes place.

Although the temperature inversion starts at a higher pressure and with a higher minimum temperature, the increase in IR absorption leads to the higher temperatures higher up in the atmosphere (as mentioned above as well). This causes the overall size of the temperature inversion to remain the same, but shifted towards higher temperatures for greater SiO_2 melt abundances. This, in combination with a greater abundance of SiO in the atmosphere, leads to very prominent SiO emission features (at 4.5 and 9 mum) at high SiO_2 melt abundance which are up to 10 ppm greater for G-type stars and around 7

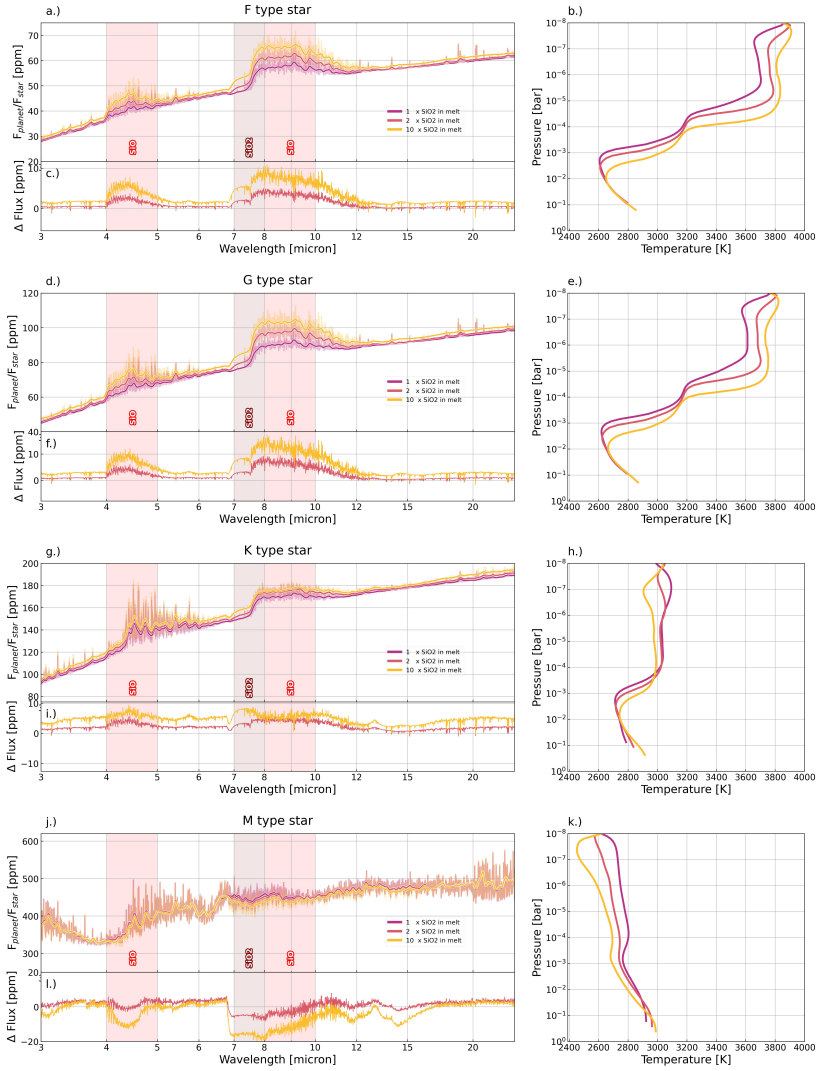


Figure 3.7: Effect of varying SiO_2 melt percentage on emission spectra - For an F-, G-, K-, and M-type star we show the calculated pseudo-2D emission spectra and TP profiles for different SiO_2 melt abundances. Under each spectrum we also plot the differences in flux between the different spectra with respect to 1 x SiO_2 melt (which is the same as a BSE composition). The TP profiles shown are those for the models calculated at a 40° angle away from the substellar point. Note the difference in the scales of the y-axes of the emission spectra for the different stellar types.

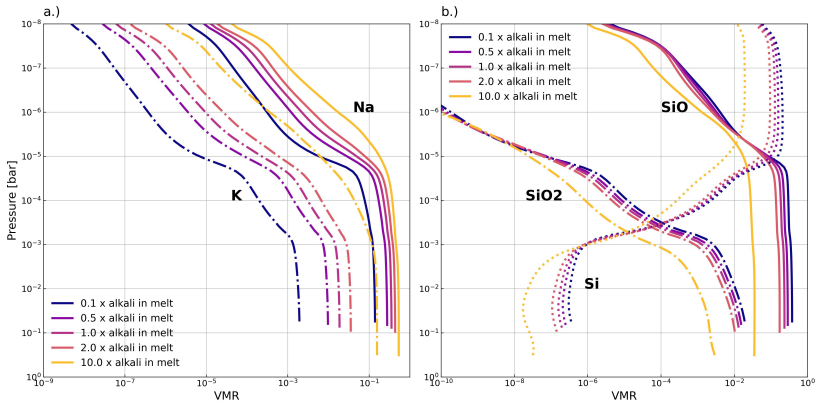


Figure 3.8: Atmospheric species changing with alkali melt abundances: Shown for a planet orbiting a G-type star (see Table 3.1 for parameters). The alkali oxide (Na_2O and K_2O) abundances in the melt were changed with respect to the BSE abundance (see Table 3.2).

ppm greater for F and K type stars than that of the BSE composition spectra (Figure 3.7).

For planets orbiting M-type stars (bottom row in Figure 3.7) we see different behaviour than for the hotter spectral types. Just as what we saw for TiO_2 melt abundance variation, increasing SiO_2 melt abundance decreases the temperature inversion strength down to the point where it is almost non-existent and most of the atmosphere is non-inverted. This leads to the atmospheric SiO and SiO_2 features becoming absorption features instead of emission features. Although difficult to discern when overlaying the spectra over each other, it becomes clearer when we look at the flux difference between the BSE case and the increased SiO_2 melt abundance models.

3.3.4 Alkali variation

Atmospheric Na and K do not contribute as significantly over broad wavelengths to the opacity of the atmosphere as TiO, SiO, and SiO_2. Hence, they do not have as strong an influence on the TP profile or low-resolution spectrum of HRE exoplanet atmospheres. However, as can be seen in Figure 3.13, they do have a number of lines across the optical and the near-infrared. They are also some of the most volatile species released in melt vaporisation from Na_2O and K_2O (Fegley & Cameron 1987; Schaefer & Fegley Jr. 2004; Zilinskas et al. 2022; van Buchem et al. 2023; Wolf et al. 2023). As such, varying the abundance of Na_2O and K_2O in the melt has a strong effect on the atmospheric abundances of Na and K. We decided to vary Na_2O and K_2O abundance concurrently due to the similarity of their behaviour.

In Figure 3.8 we show the VMR of atmospheric Na and K (in panel *a*) for

different variations of the alkali oxide (Na_2O and K_2O) abundances in the melt at an angle of 40° away from the substellar point for a G-type star. Decreasing the alkali abundance by an order of magnitude relative to the BSE abundance (0.1x) leads to a drop in total surface pressure from 7.63e-2 bar to 5.52e-2 bar, while increasing the alkali abundance by an order of magnitude increases the total surface pressure to 3.21e-1 bar. Looking at Figure 3.9 - we see that this is not due to a change in surface temperature (as we saw for TiO_2 and SiO_2) but due to an increase in vaporised Na and K. Although Figure 3.8 focuses on a planet orbiting a G-type star, we see a similar increase in surface pressure for all host star spectral types, as can be seen in the TP profiles shown in Figure 3.9. This could be of consequence to models that take heat and material redistribution over the day/night side of the planet into account (e.g. Nguyen et al. 2024).

Increasing the melt abundance of Na_2O and K_2O and the resulting increase in Na and K in the atmosphere leads to broadening of their features in the optical. The strongest effect is seen for the K features between 0.75 and 0.8 μm (see Figure 3.9). There are also a number of emission lines between 1 and 3.5 μm from atmospheric K that see significant growth of (up to 10 ppm for planets orbiting a K-type star) with increasing alkali melt abundance - these are indicated in light blue in Figure 3.9. Although the Na feature at 0.6 μm appears to broaden slightly, its peak decreases in height. This is likely due to our model not being of high enough spectral resolution to fully visualize this feature. Further work in high resolution is required to draw any definite conclusions.

Varying the abundance of alkali species in the melt significantly affects the SiO and SiO_2 atmospheric abundance, as shown in panel *b* of Figure 3.8. As a result, the SiO and SiO_2 features in the emission spectrum vary (see Figure 3.9) and the temperature structure of the atmosphere is affected (most significantly above 1e-5 bar). This effect on the atmospheric Si species is partly due to the change in abundance of SiO_2 in the melt after renormalization (similar to the change in TiO_2 abundance when increasing SiO_2 abundance in the previous subsection). However, this change in abundance is relatively small due to the alkalis making up but a small percentage of the total melt composition. Besides melt abundance, the activity (see section 3.2.2) of a species in a melt is also determined by the activity coefficient (γ). In an ideal case, this is equal to one but due to the complex nature of melts this value is usually less than one. As shown in Hirschmann et al. (1998), increasing the alkali contents of a melt decreases the activity coefficient of SiO_2 due to reducing the number of Si-O-Si linkages. In Figure 3.16 we plot both the activity of SiO_2 and its weight percentage in the melt, illustrating this effect.

We do not see any significant changes in the spectrum of the M-type star and hence do not include it. All of the models that we ran for this work can be found on GITHUB OR ZOTERO LINK.

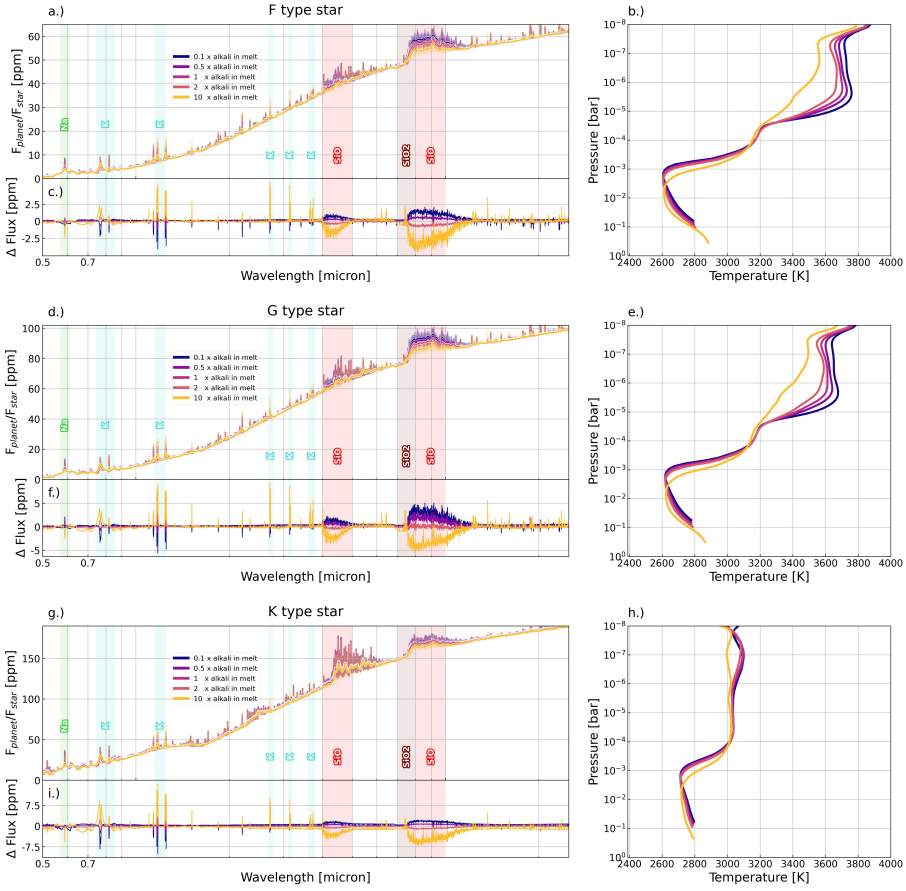


Figure 3.9: Effect of varying Na_2O and K_2O melt percentage on emission spectra: For an F-, G-, and K-type stars, we show the calculated pseudo-2D emission spectra and TP profiles for different SiO_2 melt abundances. Under each spectrum we also plot the differences in flux between the different spectra with respect to 1 x alkali abundances (which is the same as the Na_2O and K_2O weight percentages in a BSE composition). The TP profiles shown are those for the models calculated at a 40° angle away from the substellar point. Note the difference in scales of the y-axes of the emission spectra for the different stellar types.

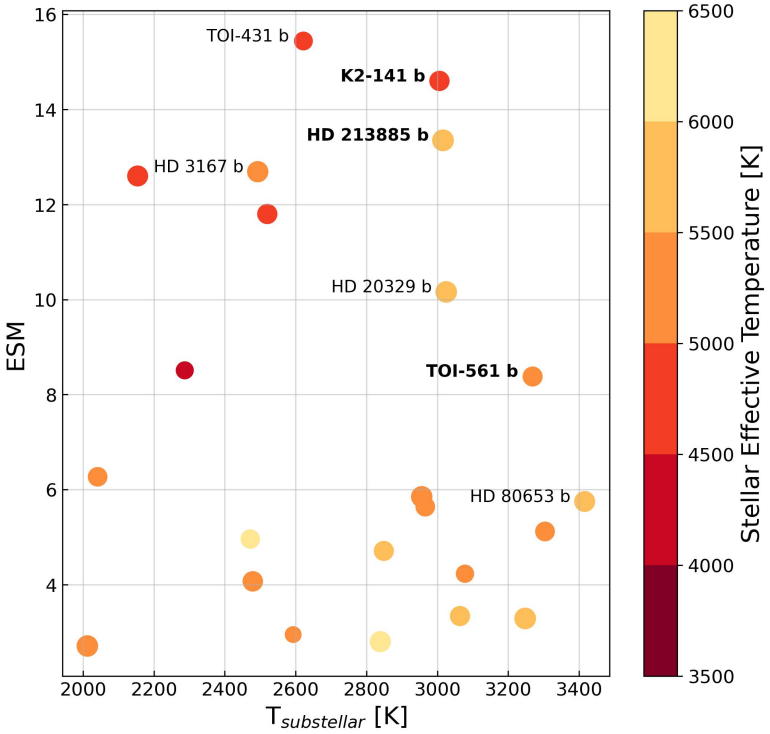


Figure 3.10: Potential observing targets - A selection of confirmed exoplanets with a radius of $< 2R_{\oplus}$ and with a substellar equilibrium temperature > 2000 K. On the y-axis we plot the emission spectroscopy metric (ESM) as defined in Kempton et al. (2018). The planets labelled in bold are those we selected for error bar estimates shown in Figures 3.12 and 3.11.

3.3.5 Observability of potential targets

With the aim of estimating the feasibility of observing variations in the HRE spectra due to changes in melt composition using JWST, we simulated eclipse observations for three different HREs. We then derived the expected precision in measuring their emission spectra for a number of different JWST instruments. In Figure 3.10, we plot a selection of confirmed HREs with a radius $< 2R_{\oplus}$ and with a substellar equilibrium temperature > 2000 K. We plotted them as a function of substellar temperature on the x-axis and their emission spectroscopy metric (ESM) on the y-axis. The ESM, as defined in Kempton et al. (2018), is a useful indicator of the expected S/N of a JWST secondary eclipse observation at mid-IR wavelengths. We also coloured the planets according to the effective temperature of their host stars. We selected HD 213885 b, TOI-561 b, and K2-141 b due to their high ESM values and substellar equilibrium temperatures, as well as covering a range of different stellar spectral types for their host stars. For our simulated observations we used the open source code `PANDEXO` (Batalha et al. 2017) and assumed six eclipses. We chose a number of groups per integration that is $\leq 80\%$ of full well-depth in order to avoid reaching saturation. We assumed an optimistic noise floor of zero ppm.

In Figures 3.11 and 3.12, we show the estimated error bars alongside TiO_2 and SiO_2 variation respectively. For HD 213885 b, we used the system parameter values published in Espinoza et al. (2020). Due to the brightness of the star HD 213885 ($V_{mag} = 7.95$, $J_{mag} = 6.81$), the number of instruments that can be used to observe it without over-saturating is limited, inhibiting observations below 2.5 μm. However, for the instruments with which can observe, the error bars are relatively small, at around 5 ppm at best for NIRSpec G395H. This could potentially allow for the extreme cases of 0.1x and 10x TiO_2 to be discerned from each other. Due to the difference in flux coming from a change in surface temperature and not a distinct feature, this would have to be complemented with some optical data (covering 0.5-1 μm) indicating the presence of TiO in the atmosphere. For SiO_2 abundance variation (Figure 3.12) we see that the error bars for NIRSpec G395H may be small enough to allow one to discern a BSE melt composition from a melt with a 10x SiO_2 abundance increase based on the 4-5 μm feature. Similarly, MIRI LRS may have enough sensitivity to discern these two aforementioned models at the SiO_2 and SiO features between 7 and 10 μm.

For TOI-561 b and K2-141 b, we used the system parameters published in Brinkman et al. (2022) and Zieba et al. (2022) respectively. Although it is possible to use greater number of instruments to observe TOI-561 b and K2-141 b without over-saturation, most error bars are too large to be able to discern any of the models with certainty. For TiO_2 variation (Figure 3.11), NIRSpec G140H and G235H may be able to discern 0.1x and 10x TiO_2 abundance from each other. However, just as with HD 213885 b, the difference in flux is coming from a decrease in surface temperature leading to a lower continuum emission and not from a specific spectral feature. Hence, without the detection of the TiO

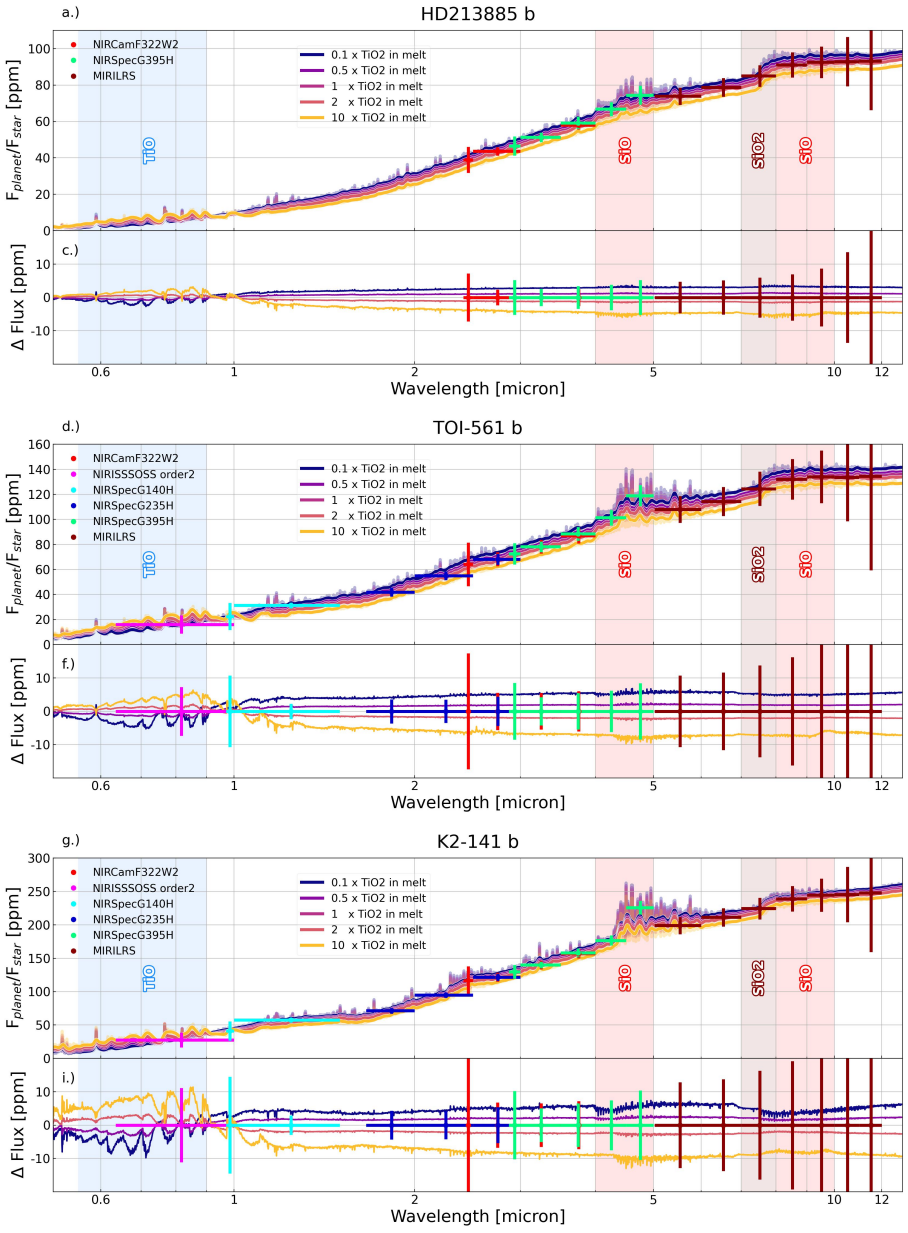


Figure 3.11: JWST error bar estimates for TiO_2 variation - Error estimates were calculated using `PANDEXO` (Batalha et al. 2017) for 6 eclipses.

feature at 0.5-1 μm, it would be difficult to know if the change in temperature is due to the presence of TiO in the atmosphere or due more efficient heat-redistribution than expected. NIRISS SOSS could potentially have been used to break this degeneracy, but does not appear to be sensitive enough. For SiO_2 variation neither NIRSpec G395H nor MIRI LRS appear to be sensitive enough to convincingly discern the different melt compositions from each other.

Overall, it appears difficult to discern changes in melt compositions of HREs using only JWST spectroscopy. The most promising target seems to be HD 213885 b, for which, as of the writing of the paper, there are no planned JWST observations. Observations would likely be most useful if combined with (potentially) Earth-based optical high-resolution spectra that could be used to discern specific species in the atmosphere.

3.4 Discussion

3.4.1 Melt compositions

In section 3.2.1, we have shown (Figure 3.1) that the tested compositional ranges cover the compositional variation of bulk silicate reservoirs derived from stellar compositions (Putirka & Rarick 2019). However, studies of the early chemical evolution of rocky bodies in our own solar system show that the possible range in composition of lava oceans is likely to be significantly larger. The evolution of Earth's Moon serves as a good example. A wide range of geochemical evidence suggests that the Moon was fully molten shortly after its formation in the aftermath of a giant impact on Earth (e.g. Steenstra et al. 2020). At this time the lunar core segregated from the lunar mantle, and the composition of the molten surface was equal to the composition of the whole silicate reservoir. Subsequently, the Moon formed a $>$ 30km thick primary crust formed primarily by the mineral plagioclase (e.g. Elkins-Tanton et al. 2011; Lin et al. 2017), with a composition far richer in Al, Ca, and Si, and far poorer in Fe, Mg, and Ti, than this initial bulk silicate reservoir. Subsequent volcanism concentrated on the lunar nearside then led to the formation of a range of lavas rich in Mg, and Fe, exhibiting a range in TiO_2 concentrations up to $>$15 wt. per cent, well beyond the maximum of the range of lava compositions based on bulk silicate abundance estimates (Figure 3.1). All other rocky bodies in the inner solar system show crustal compositions that are both different from bulk silicate compositions and that vary across the surface. Clearly geological processes can significantly expand both absolute and relative element abundances of surface materials.

3.4.2 Assumptions made in our model

The model used for this work is a pseudo-2D model that assumes thermochemical equilibrium (see section 3.2). This does not take into account chemical

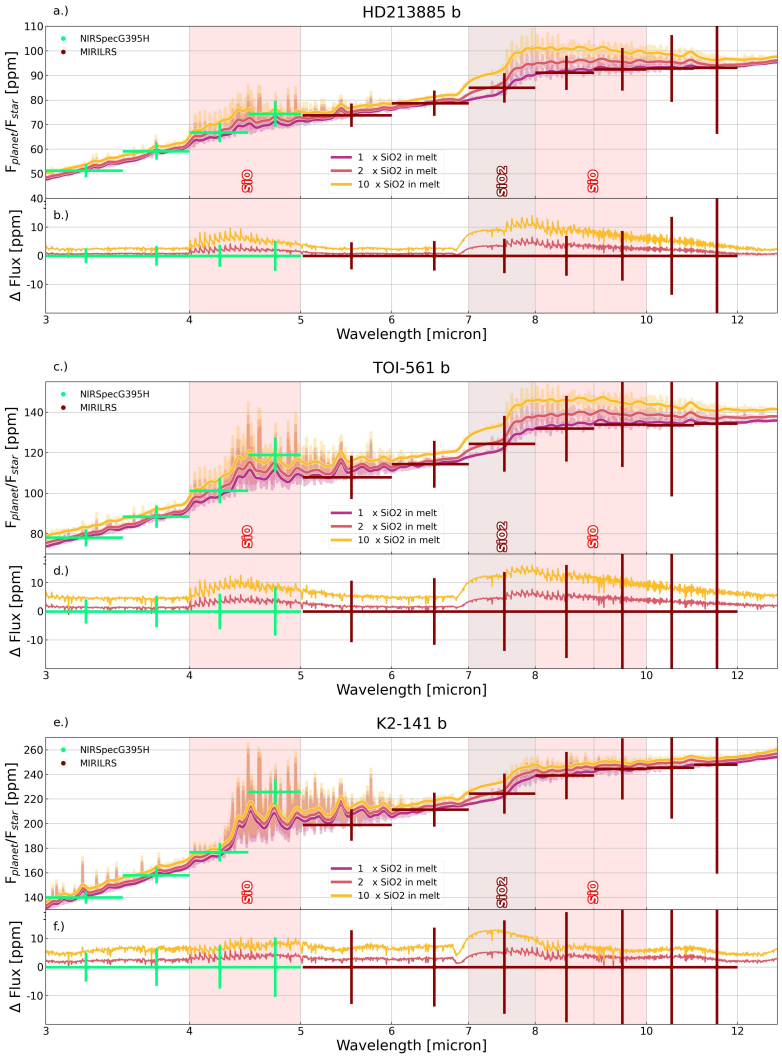


Figure 3.12: JWST error bar estimates for SiO_2 variation - Error estimates were calculated using `PANDEXO` (Batalha et al. 2017) for 6 eclipses.

kinetics that may be taking place higher up in the atmosphere where strong UV radiation could lead to chemical dissociation. Due to the high temperatures of the modelled atmospheres, it is likely that a chemical equilibrium approach provides a good approximation of the atmospheric chemistry. In order to investigate whether photochemistry could have a significant influence, chemical pathways for silicates are needed, which are currently unavailable in literature.

We do not take condensation into account either. As shown in Nguyen et al. (2024), this could have some effect on the temperature structure of the planet at different longitudes. Future work could be focused on combining condensation calculations with a pseudo-2D model to take the resulting changes in temperature structure and (potentially) cloud opacity into account.

The fact that we focus on low resolution spectra means that our results do not rule out that other melt oxide species could be important to high resolution spectral analysis.

3.4.3 Surface temperature degeneracy

As discussed in the results section and as shown in Figures 3.5 and 3.11, varying TiO_2 melt abundance, directly influences TiO atmospheric abundance, which has a very strong influence on the surface temperature of the planet. This is due to its strong optical opacity.

Concluding that an HRE atmosphere contains TiO because the apparent surface temperature is lower than what one would expect without TiO, would be ignoring other key factors that can affect planetary surface temperatures and should therefore not be used as direct evidence. For example, in Hu et al. (2024), the emission spectrum found for 55-Cnc e pointed to a surface temperature of several hundreds of Kelvin lower than expected for a bare lava-vapour atmosphere. This was attributed to the presence of a volatile (potentially carbon-rich) atmosphere leading to more efficient heat-redistribution from the day- to the night-side. Other studies have shown that the presence of clouds may have a significant effect on surface temperatures as well (Nguyen et al. 2024; Loftus et al. 2024).

Conversely, future interpretations of HRE emission spectra should also consider the effect that a significant TiO abundance in the atmosphere could have on the temperature-pressure structure of a lava planet. A potential way to disentangle the resulting degeneracy would be to try and observe the TiO emission feature found between 0.55 and 0.9 μm.

3.5 Conclusion

We investigated how varying the abundances of oxide melt species at the surface of a lava planet affects its atmospheric emission spectrum. We modelled the atmospheres and resulting emission spectra using chemically self-consistent pseudo-2D models for dry HREs orbiting F-, G-, K-, and M-type host stars.

We find that the melt species which have the most significant influence on the emission spectra of HREs are TiO_2 and SiO_2.

TiO_2 melt abundance dictates atmospheric TiO abundance, which, due to its strong optical opacity, heavily influences the surface temperature of the planet if it orbits an F-, G-, or K- type star. This change in surface temperature affects both the total pressure of the vaporised atmosphere and its composition - affecting the strength of emission features of species such as SiO. The decrease in temperature caused by the presence of TiO affects all but the upper reaches of the atmosphere, leading to a drop in the continuum of emission of the planet. A potential way to discern this drop in temperature as being due to the presence of TiO and not due to efficient heat-redistribution is by observing the TiO optical emission feature.

Increasing the SiO_2 melt abundance leads to a significant increase in the strength of the atmospheric SiO and SiO_2 features in the infrared for planets orbiting F-, G-, and K-type stars. It also leads to stronger and deeper temperature inversions, below the point where SiO_2 has the highest opacity contribution. This leads to the SiO_2 feature flipping from being an absorption feature to being an emission feature.

Varying the melt abundance of the alkali oxides Na_2O and K_2O influences the abundance of atmospheric Na and K respectively. This affects the K (and single Na) spectral features in the optical and near-infrared, which may merit further investigation with high-resolution modelling for HRE planets orbiting F-, G-, or M-type stars. The increase in atmospheric Na and K at relatively large melt abundances of Na_2O and K_2O lead to a large increase in the total pressure of the atmosphere. This could potentially be of importance for heat-redistribution models.

Varying the alkali abundance in the melt also affects the activity of the SiO_2 in the melt, with greater alkali abundances leading to lower SiO_2 activities. This significantly impacts the abundances of atmospheric Si species and hence the strength of the SiO and SiO_2 features in the emission spectrum.

To estimate the observability of these changes in emission spectra due to changes in melt composition, simulated JWST observations for HD213885 b, TOI-561 b, and K2-141 b. These planets were selected due to their high infrared observability metric (ESM) and high surface temperatures. We found that with six eclipses, only the most extreme differences in melt composition may be discernible from each other in the infrared for HD213885 b, and in the near-infrared for TOI-561 b, and K2-141 b.

Acknowledgements

This work was supported financially through a Dutch Research Council (NWO) Planetary and Exoplanetary Science (PEPSci) grant awarded to Y.M. and W. van W. Y.M and M.Z. acknowledge funding from the European Research Council (ERC) under the European Union's Horizon 2020 research and innovation

programme (grant agreement no. 101088557, N-GINE). R. B. acknowledges funding from the Oort and Legaat Kruytbosch Scholarship.

Data Availability

The data underlying this article is available upon reasonable request from the author.

Appendix

3.A Melt compositions

The melt compositions are calculated by multiplying their original BSE weight percentage, as given in Palme & O'Neill (2003), by different factors (0.1, 0.5, 2, and 10). This leads to weight percentages of greater than 100 for some species. This is not an issue for LavAtmos due to the fact that the composition is normalized internally. However, it may give a wrong impression of the actual abundance that is being tested. Hence, we provide a table below showing the varied weight percentages for each of the species for which we present results (indicated with *Before norm.*) as well as their normalized counterparts (indicated with *After norm.*). Note that SiO_2 abundances lower than BSE could not be tested due to limitations of the MELTS code.

Table 3.2: Melt composition variation

	Multiplier								
	x0.10		**x0.50**		**x1**	**x2**		**x10**	
Species	Before norm. [%]	After norm. [%]	Before norm. [%]	After norm. [%]	**BSE**	Before norm. [%]	After norm. [%]	Before norm. [%]	After norm. [%]
SiO_2	-	-	-	-	**4.54E+01**	9.08E+01	6.24E+01	4.54E+02	8.93E+01
TiO_2	2.10E-02	2.10E-02	1.05E-01	1.05E-01	**2.10E-01**	4.20E-01	4.19E-01	2.10E+00	2.06E+00
Na_2O	3.49E-02	3.50E-02	1.75E-01	1.75E-01	**3.49E-01**	6.98E-01	6.96E-01	3.49E+00	3.38E+00
K_2O	3.10E-03	3.10E-03	1.55E-02	1.55E-02	**3.10E-02**	6.20E-02	6.20E-02	3.10E-01	3.09E-01

Table 3.3: Opacity data: List of opacities and their sources used to calculate the temperature-pressure profiles and emission spectra in this work. Those with DACE as indicated source were taken directly from the DACE database (`https://dace.unige.ch/`). For the other species, the opacities were calculated using HELIOS-K (`https://github.com/exoclime/HELIOS-K`) (Grimm & Heng 2015; Grimm et al. 2021).

Species	Source	Line list	Line list reference
Al	DACE	VALD	Ryabchikova et al. (2015)
AlO	HELIOS-K	ATP	Patrascu et al. (2015)
Ca	DACE	VALD	Ryabchikova et al. (2015)
CaO	HELIOS-K	VBATHY	Yurchenko et al. (2016)
Fe	DACE	VALD	Ryabchikova et al. (2015)
K	DACE	VALD	Ryabchikova et al. (2015)
Mg	DACE	Kurucz	Kurucz (1992)
MgO	HELIOS-K	LiTY	Li et al. (2019)
Na	DACE	VALD	Ryabchikova et al. (2015)
Si	DACE	VALD	Ryabchikova et al. (2015)
SiO	HELIOS-K	SiOUVenIR	Yurchenko et al. (2022)
SiO_2	DACE	OYT3	Owens et al. (2020)
Ti	DACE	VALD	Ryabchikova et al. (2015)
TiO	HELIOS-K	Toto	McKemmish et al. (2019)
Scattering and continuum			
O_2	Scattering		Gray (2008)
O_2-O_2	petitRADTRANS		Mollière et al. (2019, 2020)

3.B Opacity data

3.C Stellar spectra

3.D Pseudo-2D atmosphere

3.E SiO_2 activity changing with alkali abundances

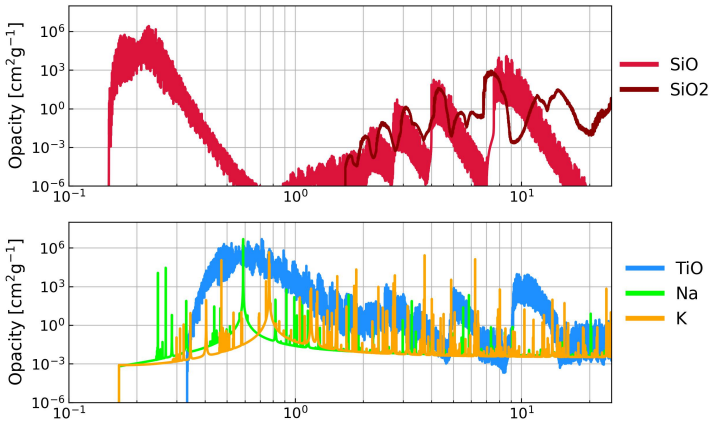


Figure 3.13: Opacities of important atmospheric species: The unweighed opacities of SiO, SiO_2, TiO, Na, and K are shown here for a temperature of 2700 K and 1e-2 bar. See Table 3.3 for the line lists used to calculate the opacities shown here.

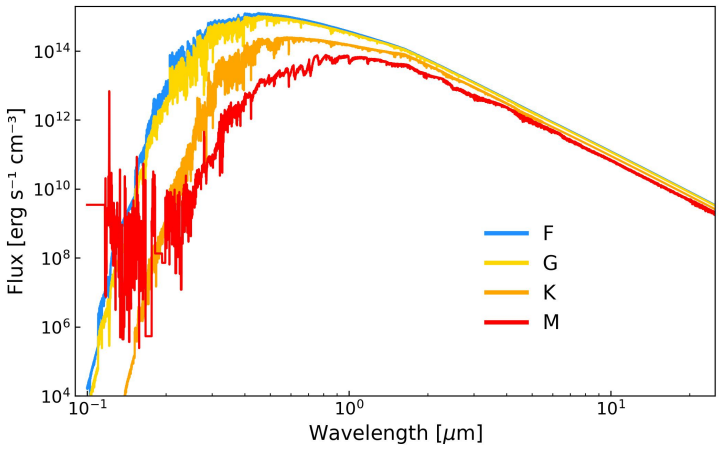


Figure 3.14: Stellar spectra used for each of stellar type: The spectra for the F, G, and K stars were calculated using the `PHOENIX` models. For the M type star we combined the `PHOENIX` model with scaled `MUSCLES` shortwave spectra.

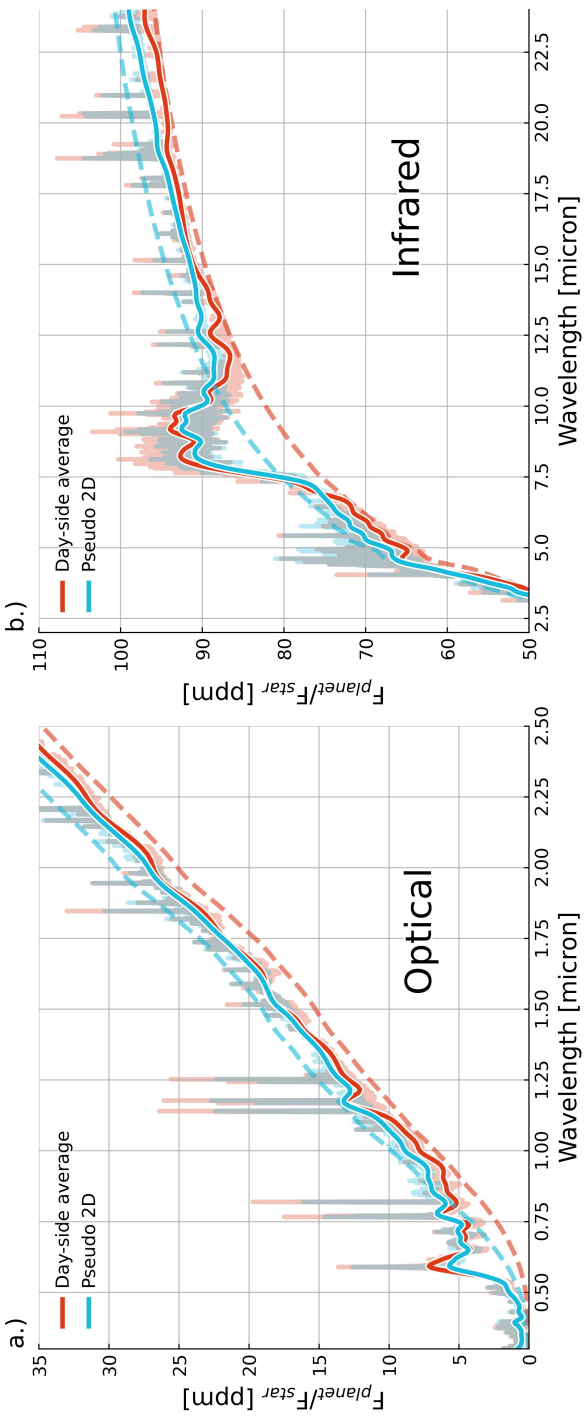


Figure 3.15: Comparison between a pseudo-2D model and a dayside averaged model: The low resolution day-side averaged spectrum is shown in orange, the pseudo-2D approach is shown in light blue. The higher resolution version of the spectra or shown using a lower opacity in the background and the spectra for an empty atmosphere (airless rock) on the same planet is shown using the dashed lines. The left panel (a) shows the spectra within the optical wavelength range, while the right side panel (b) shows the spectra within the infrared wavelength range.

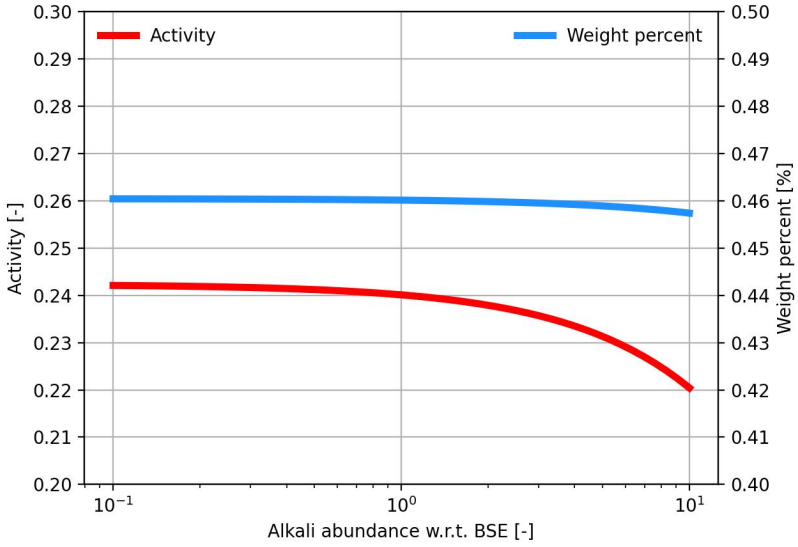


Figure 3.16: SiO_2 melt activity as a function of changing alkali abundances: Calculated using ThermoEngine, the python wrapper to MELTS (Ghiorso & Sack 1995).

4 LavAtmos 2.0: Incorporating volatile species in vaporisation models

Work published in **C. P. A. van Buchem**, M. Zilinskas, Y. Miguel, W. van Westrenen, *Astronomy & Astrophysics*, Vol 695, A157 (2025), Reprinted here in its entirety.

Abstract

Due to strong irradiation, hot rocky exoplanets are able to sustain lava oceans. Direct interaction between these oceans and overlying atmospheres can provide insight into planetary interiors. In order to fully understand how the composition of the atmosphere of such planets are affected by the properties of the oceans, comprehensive chemical equilibrium models are required. Thus far, most models have only taken non-volatile species into account when calculating lava vaporisation.

We investigate the effect of including C-, H-, N-, S-, and P-bearing species in the equilibrium lava vaporisation calculations on the overall atmospheric composition of hot rocky exoplanets by expanding our LavAtmos code.

We calculated the O_2 partial pressure which satisfies both the laws of mass action and mass conservation in a system that contains both melt species and volatile elements. We integrated the chemical equilibrium code FastChem to expand the number of considered gas phase species to 523. We applied this new approach to calculate the composition of "pure" atmospheres which contain only C, H, N, S, or P and of more complex atmospheres which contain all five aforementioned elements. We also tested two proposed compositions for the atmosphere of 55-Cnc e.

We find that the inclusion of volatile elements in vaporisation calculations increases the partial pressures of vaporised species (SiO, SiO_2, Na, and K) compared to volatile-free vaporisation for all tested atmospheric compositions. Moreover, including volatile species in the vaporisation reactions leads to a significantly greater O abundance in the atmosphere than in the volatile-free vaporisation case, which influences partial pressures of key volatile species such as CO_2 and H_2O. When testing the compositions proposed for 55-Cnc e, we find that a low C/O ratio could potentially serve as an indication of the presence of a surface lava ocean on an ultra-short-period planet with a volatile atmosphere.

Volatile elements must be taken into account for comprehensive modelling of vaporisation from a surface lava ocean into a volatile atmosphere.

4.1 Introduction

Recent years have seen a growing interest in the properties of ultra-short period (USP) rocky planets. The proximity of these planets to their host star causes their surfaces to be highly irradiated, reaching temperatures that exceed those required to initiate rock melting (∼1500 K). As a result a significant part of their surface could be covered by a lava ocean (Léger et al. 2009; Henning et al. 2018; Boukaré et al. 2022). A lava ocean serves as a direct interface between the interior and the atmosphere of these planets, allowing the two reservoirs to thermochemically equilibrate with each other, creating a strong link between the compositions of the two. Hence, characterising the chemical composition of a USP rocky world's atmosphere could in principle be used to place constraints on its interior chemical composition. Thanks to the strong observational biases favouring the discovery of short period planets with current detection methods (Beatty & Gaudi 2008), a large number of potential targets for detailed study exists (Zilinskas et al. 2022). The advent of JWST and the development of telescopes such as Ariel and the ELT promise to provide the opportunity to begin characterising the chemical composition of USP atmospheres. Therefore, understanding of the interior-atmosphere compositional link of these planets is more relevant than ever and could be used to provide insights into their chemical and formation history (Schaefer & Fegley 2009; Morbidelli & Raymond 2016; Lichtenberg 2021).

To be able to infer the interior composition from the atmospheric composition of rocky planets, a quantitative understanding of outgassing and ingassing processes is required. A growing number of studies have shown that the vaporisation of a lava ocean with chemical compositions similar to silicate compositions found in our solar system should lead to atmospheres containing species such as SiO, SiO_2, Na, K, MgO, TiO, and a wide variety of other compounds (e.g. Schaefer & Fegley Jr. 2004; Miguel et al. 2011; Ito et al. 2015; Kite et al. 2016; Fegley et al. 2023; van Buchem et al. 2023; Wolf et al. 2023). The abundances of these species present in the atmosphere determine their observability, with SiO and SiO_2 being the easiest to detect due to their high molecular opacity between 7-10 micron (Zilinskas et al. 2022).

In much of the previous work, the simplifying assumption is made that volatile elements such as carbon (C), hydrogen (H), nitrogen (N), sulfur (S), and phosphorus (P) are absent in the atmospheres of USP rocky planets due to the extreme irradiation undergone by these planets and the resulting atmospheric erosion and escape. However, there are indications that magma oceans may potentially harbour large reservoirs of water Hirschmann (2012); Lebrun et al. (2013); Dorn & Lichtenberg (2021); Kite & Schaefer (2021). In addition, Herbort et al. (2020) shows the possibility of stable hot atmospheres containing C, H, N, and S species. The emission spectrum of 55-Cnc e recently observed by JWST shows a day-side temperature of 2000 K (Hu et al. 2024), low relative to the expected equilibrium temperature. This suggests strong heat redistribu-

tion to the night side of the planet. Together with infrared absorption features at ≃4.5 micron, due to either CO or CO_2, this suggests that this USP rocky planet supports a significant volatile atmosphere. Hence, both theory and observations are pointing to the necessity of quantitatively assessing the effects of the presence and abundance of volatile elements when modelling lava ocean outgassing on USP rocky-planets.

Piette et al. (2023) and Zilinskas et al. (2023) have shown that volatile atmospheres may suppress the signatures of vaporised species in the spectra of USP-rocky planets, but these studies do not take into account the effect that volatiles have on the vaporisation of lava and the abundances of the outgassed species. Instead, calculated abundances of the elements coming from vaporised lava are simply added to the total assumed abundances of one or more volatiles in the atmosphere. This does not take into account how volatile species influence the vaporisation reactions themselves.

Charnoz et al. (2023) have investigated what the effect is of the presence of H in the atmosphere of a USP rocky-planet on the vaporisation from a lava ocean by including the formation of H_2O from H_2 and O_2 in chemical equilibrium calculations. They conclude that even a small amount of H (≃1 bar) in the atmosphere can increase the partial pressure of vaporised species (such as SiO and SiO_2) by several orders of magnitude. Using this approach, Falco et al. (2024) have shown that hydrogenated atmospheres can still contain sufficient SiO (≃ 4 bar at a surface temperature of 3000 K) to yield detectable SiO features in the infrared. In this paper we expand upon the approach of Charnoz et al. (2023) by including all melt species available in LavAtmos (van Buchem et al. 2023), as well as all the gas species included in thermochemical equilibrium code FastChem (Stock et al. 2018).

We first apply the resulting code (LavAtmos 2.0) to 'pure' C, H, N, S, and P atmospheres in order to isolate the individual effects that these most common volatile elements have on vaporisation from a lava ocean. We then apply the code to 'complex' volatile atmospheres which are dominated by one volatile element but which contain all of the other volatile elements as well. Finally, we test the effects of N_2, CO, and CO_2-rich atmospheres that are commonly assumed in studies predicting the expected spectral signature of rocky exoplanet atmospheres and that give a good fit to the recently published 55-Cnc e data (Hu et al. 2024). Based on these results, we point out which chemical species could, if detected in the atmosphere of a USP rocky planet, hint at the presence of a lava ocean and potentially constrain aspects of its chemical composition.

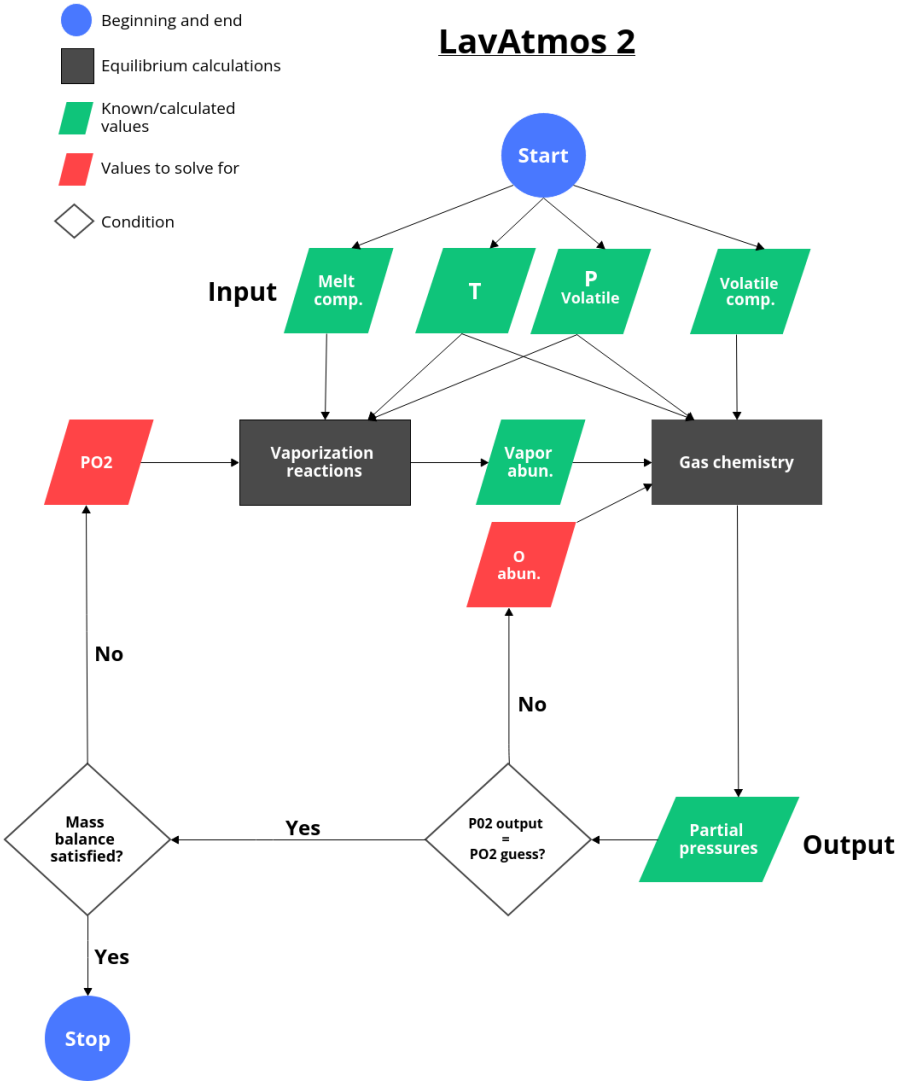


Figure 4.1: Diagram of the LavAtmos 2.0 equilibrium code: The given input (top of the diagram) includes the melt composition, temperature and pressure at the surface of the melt, and the elemental abundances of the volatile elements in the atmosphere. The output consists of partial pressures of all of the species in the atmosphere. The vaporisation reactions are calculated in the same way as in van Buchem et al. (2023). See section 4.2 for a more detailed explanation of how the code works.

4.2 Methods

4.2.1 Workflow

LavAtmos is an open-source thermochemical vaporisation Python code described in detail in van Buchem et al. (2023). It is based on the principle of using the laws of mass action and mass conservation to constrain the partial pressure of O_2 (P_{O_2}) released in lava vaporisation reactions. The thermodynamic properties of the lava are quantified using the MELTS code (Ghiorso & Sack 1995; Asimow & Ghiorso 1998; Ghiorso et al. 2002; Gualda et al. 2012; Ghiorso & Gualda 2015). The original version of LavAtmos covers 31 gas phase species. It does not consider gas-gas reactions, and the only source of atmospheric components is evaporation from lava as calculated from liquid-gas reactions. In LavAtmos 2.0, we expanded the original concept by making use of the gas-phase chemical equilibrium solving abilities of FastChem 3 (**?**) in order to include the effect of volatile elements (for example, those present in a primary atmosphere) on the vaporisation of melt species. We note that condensation reactions, which FastChem 3 can incorporate, are not considered in this work.

To illustrate our method, we walk through the model assuming a lava ocean that is composed of pure molten SiO_2, and that only the volatile element H is present in the atmosphere. We make use of the flow-chart shown in Figure 4.1 to visualise the working of the code. Code input includes a melt composition, a surface temperature T, a total volatile pressure P, and mole fractions of the included volatile elements (green parallelograms at the top of the flow-chart). The total volatile pressure is the pressure of all volatile elements (C, H, N, S, and P) assumed to be in the atmosphere and does not include the species vaporised from the lava ocean. The total pressure of the atmosphere at the gas-melt interface is the sum of the total volatile pressure and the total vaporised pressure. The volatile composition is given as input in the form of elemental fractions of the volatile atmosphere.

With this input, the code calculates the elemental abundances of the vaporised elements coming from the melt. This is done by first calculating the partial pressures of vaporised species. Using our example of a pure SiO_2 melt, we have to consider the following vaporisation reactions:

$$\mathrm{SiO_2(l)} \leftrightarrow \mathrm{SiO_2(g)}, \tag{4.1}$$

and

$$\mathrm{SiO_2(l)} - \frac{1}{2}\mathrm{O_2(g)} \leftrightarrow \mathrm{SiO(g)}. \tag{4.2}$$

The partial pressures of $SiO_2(g)$ and $SiO(g)$ are calculated using the law of mass action and by assuming an ideal gas as follows:

$$P_{\mathrm{SiO_2(g)}} = K_1(T) a_{\mathrm{SiO_2(l)}}, \tag{4.3}$$

and

$$P_{SiO(g)} = K_2(T) a_{SiO_2(l)} P_{O_2}^{-1/2}, \tag{4.4}$$

where $P_{SiO_2(g)}$ and $P_{SiO(g)}$ are the partial pressures of the vaporised species, K_1 and K_2 are the temperature dependent chemical equilibrium constants specific to reactions (1) and (2), respectively, and $a_{SiO_2(l)}$ is the chemical activity of SiO_2 in the melt (see van Buchem et al. (2023) for a more in depth derivation). The chemical equilibrium constant of each reaction is determined using the JANAF tables (Chase 1998) and the activities of the melt species are calculated[1] using MELTS (Ghiorso & Sack 1995; Asimow & Ghiorso 1998; Ghiorso et al. 2002; Gualda et al. 2012; Ghiorso & Gualda 2015). MELTS requires pressure as input due to the fact that beyond 100 bar, increasing pressure starts to have a significant effect on the activities of the endmember-species. Vaporised atmosphere pressures do not reach these pressures within the parameter space explored in this work. However, total volatile pressures do. For this reason we use the total volatile pressure as the total pressure given as input to MELTS (as can be seen in the flowchart in Figure 4.1).

This leaves only P_{O_2} as an unknown in equation 4.4. Since we do not know a priori the correct value for P_{O_2}, we make an initial guess (as indicated in the red parallelogram in the top left corner of the flow-chart in Figure 4.1). From the resulting SiO and SiO_2 partial pressure values, we calculate the initial Si abundance in the atmosphere. This is passed on to FastChem 3, along with the abundance(s) of the volatile element(s), which in the case of this working example is H. The addition of H to the gas equilibrium chemistry means that the P_{O_2} calculated by FastChem will not be the same as the P_{O_2} used to calculate the Si abundances used by FastChem. We must therefore find the O abundance that corresponds to the P_{O_2} value used for the vaporisation calculations in order to match the P_{O_2} imposed by the melt with that in the atmosphere. This approach is necessary due to the fact that we cannot fix PO_2 a-priori when doing FastChem calculations. To achieve this, we guess an initial atmospheric O abundance (red parallelogram in the middle of the flow chart). We pass this to FastChem 3, which outputs partial pressures (green parallelogram, bottom right). If the P_{O_2} output by FastChem 3 is not the same as the P_{O_2} used for the vaporisation reactions, then we assign a new value for the atmospheric O abundance. This is iterated until the FastChem 3 output for P_{O_2} matches the original P_{O_2} guess used for the vaporisation reactions. This ensures that the law of mass action is upheld. Once this condition has been satisfied, we assess if the law of mass balance is satisfied. Assuming that the only species included in our example model are SiO, SiO_2, O_2, H_2, and H_2O, the following equation must hold:

$$0 = P_{O_2} + \frac{1}{2} P_{H_2O} - P_{SiO_2} - \frac{1}{2} P_{SiO}. \tag{4.5}$$

[1] Note that in our particular example, the activity of SiO_2 in the melt would be equal to 1.

This ensures mass balance for oxygen. If condition 4.5 is not satisfied, we return to the top left of the diagram and try a new P_{O_2} value. This 'outer' loop as well as the 'inner' loop (used to determine the correct O abundance to give to FastChem 3) are solved using the Scipy optimization function fsolve[2]

In this worked example, solving for P_{O_2} yields the partial pressures of the above mentioned species (SiO, SiO_2, O_2, H_2, and H_2O) for the given input parameters. In the full version of the code, partial pressures are given for all species with elements present in the melt composition and/or the volatile composition, and that are included in FastChem 3 (Kitzmann et al. 2024). Both LavAtmos 1 and 2 are available on GitHub[3] under the GNU General Public License v3.

It should be noted that this method works under the important assumption that all of the O in the atmosphere comes from vaporisation reactions. This is a commonly used assumption for work done on modelling vaporisation reactions from melts into volatile-free atmospheres (Fegley & Cameron 1987; Schaefer & Fegley Jr. 2004; Kite et al. 2016; van Buchem et al. 2023; Wolf et al. 2023; Charnoz et al. 2023; Seidler et al. 2024). This assumption holds if we assume that the lava ocean is the dominant oxygen reservoir with respect to the atmosphere. We also do not take the solubility in a melt of volatile species such as H_2O or CO_2 into account. The possible effects of this are discussed in section 4.5.1.

4.2.2 Model validation

Extensive validation of the LavAtmos code is described in van Buchem et al. (2023). Here we focus on the validation of the expanded capabilities of LavAtmos 2. Charnoz et al. (2023) were the first to apply a similar method to vaporisation from a melt into an atmosphere containing only H. In Figure 4.2 we plotted the mole fractions of H_2, H_2O, O_2, SiO, SiO_2, Fe, Na, and K in as calculated using LavAtmos 2 (solid lines) alongside the mole fractions published in Charnoz et al. (2023) (dashed lines). These were calculated for a melt with a bulk silicate earth (BSE) composition (Palme & O'Neill 2003) at a temperature of 2000 K. The very close match between the two outputs serves as validation of our code. However, we do observe a significant difference between the two approaches in the partial pressures calculated for SiO_2. LavAtmos 2 makes use of FastChem (Stock et al. 2018, 2022; **?**) for the equilibrium gas-chemistry, while Charnoz et al. (2023) use the CEA/NASA code (Gordon & Mcbride 1994). Both codes make use of the JANAF-NIST thermochemical tables (Chase 1998) to source their thermochemical constants, however they further complement their databases from different sources and have different approaches for minimising the Gibbs free energy of the system. This is likely the reason for the differences of SiO_2 seen in Figure 4.2.

[2]https://docs.scipy.org/doc/scipy/reference/generated/scipy.optimize. fsolve.html.
[3]https://github.com/cvbuchem/LavAtmos

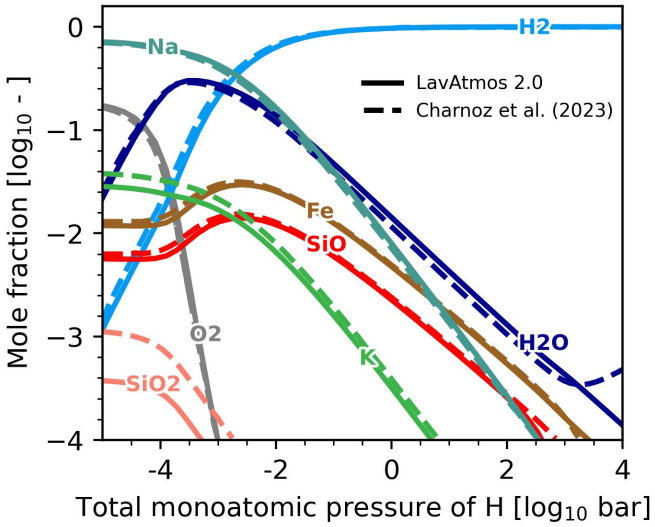


Figure 4.2: Mole fraction output comparison: Results from LavAtmos 2.0 are shown using solid lines and results from Charnoz et al. (2023) are shown using the dashed lines. A surface temperature of 2000 K and a BSE composition of the melt are assumed for both sets of calculations.

4.3 Results

The first subsection looks at the effect of volatile atmospheres containing a single volatile element so as to isolate and compare the individual effects of the major volatile elements C, H, N, S, and P. In the second subsection of the results we show the effect of complex volatile atmospheres by testing volatile compositions that are dominated by one or two elements but contain at least a few percent of each of the other major volatile elements (see Table 4.1), representing atmospheres that could be expected on USP with volatile atmospheres. All of these results are calculated assuming a bulk silicate earth composition (BSE, taken from Palme & O'Neill (2003)) for the lava ocean.

4.3.1 Effect of pure volatile atmospheres

As mentioned in section 4.2, we assume that all of the atmospheric oxygen comes from the vaporisation of melt. When there are no volatile elements present in the atmosphere, vaporised O_2 is an abundant species in the atmosphere. However, if we add the volatile elements H, C, N, S, and/or P to the atmosphere, these react with O_2 to form oxygenated species which reduces the O_2 partial pressure. This affects the vaporisation from the melt. As shown in the methods section (equation 4.4), the law of mass action dictates that

Table 4.1: Volatile components in complex atmosphere compositions above a BSE lava ocean considered in this work

Atmosphere type	C [w%]	H [w%]	N [w%]	S [w%]	P [w%]	O [w%]
Archetypal complex atmospheres						
C dominated	80.00	10.00	9	0.50	0.50	-
H dominated	1.00	80.00	18.00	0.50	0.50	-
N dominated	1.00	18.00	80.00	0.50	0.50	-
S dominated	5.00	1.00	4.00	60.00	30.00	-
55-Cnc e best fits (Hu et al., 2024)						
Carbon poor	9.09e-6	99.01	0.90	3.33e-6	6.67e-6	9.09e-7
Carbon rich	0.91	79.21	0.79	6.67	3.33	9.09

Notes. The percentages are relative to the total amount of volatiles (C, H, N, S and P) added. The first four compositions, labelled "archetypal complex atmospheres", are first-order approximations of possible atmospheres dominated by one of the volatile elements. The other two compositions, labelled "55-Cnc e best fits" are volatile atmospheres that were found to be consistent with recent JWST MIRI and NIRCam observations of 55-Cnc e (Hu et al. 2024).

the partial pressure of SiO is inversely proportional to the square root of the O_2 partial pressure of the atmosphere above the melt. All vaporisation reactions in which O_2 is released are inversely proportional to $P_{O_2}^n$ where n is the amount of O_2 released in the reaction. So, the more O_2 released in the vaporisation reaction, the stronger the dependence of its partial pressure on O_2. Due to the formation of oxygenated species in volatile atmospheres, such as H_2O and CO_2, the O_2 partial pressure drops significantly when compared to non-volatile atmospheres, which increases the amounts of vaporised elements in the atmosphere.

This effect is demonstrated in Figures 4.3, 4.4, and 4.5. In Figure 4.3 each row shows the partial pressures of a single species (O_2, SiO_2, SiO, and Si) as a function of total volatile pressure at a fixed surface temperature of 3000 K (left column) and as a function of surface temperature at a fixed total volatile pressure of 1 bar (right column). The non-volatile atmosphere case is shown using the dashed grey lines alongside the values for pure H, C, N, S, and P volatile atmospheres (where 'pure' means that there is only one volatile element present in the atmosphere into which the melt is vaporising). The total atmospheric pressure of a pure H atmosphere with a volatile pressure of 1 bar is equal to the sum of 1 bar and the total pressure of vaporised species. In Figure 4.4 we show how the major volatile species behave for each 'pure' volatile atmosphere.

At 3000 K the total pressure of a pure melt vapour atmosphere is about

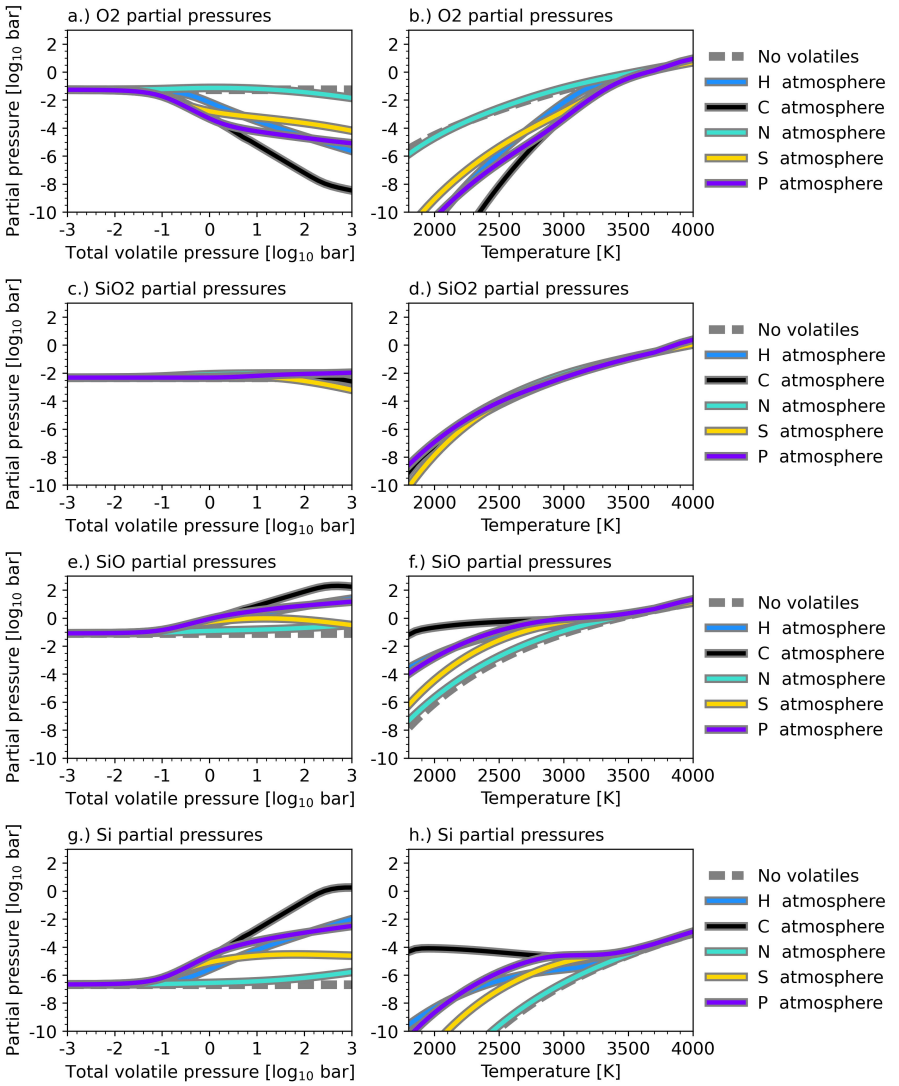


Figure 4.3: Effect of pure volatile atmospheres on Si species: Shown here are the partial pressures of SiO_2 (top row, panels *a* and *b*), SiO (middle row, panels *c* and *d*), and Si (bottom row, panels *e* and *f*) above a BSE lava ocean. The plots in the *left* column show partial pressures as a function of total volatile pressure at a fixed temperature of 3000 K. The plots in the *right* column show partial pressures as a function of temperature at a fixed total volatile pressure of 1 bar. The partial pressures of vaporised species in an atmosphere without volatiles (grey dashed line), pure H atmosphere (dark blue), pure C atmosphere (black), pure N atmosphere (light blue), pure S atmosphere (dark purple), and pure P atmosphere (light purple) above a BSE lava ocean are shown for comparison.

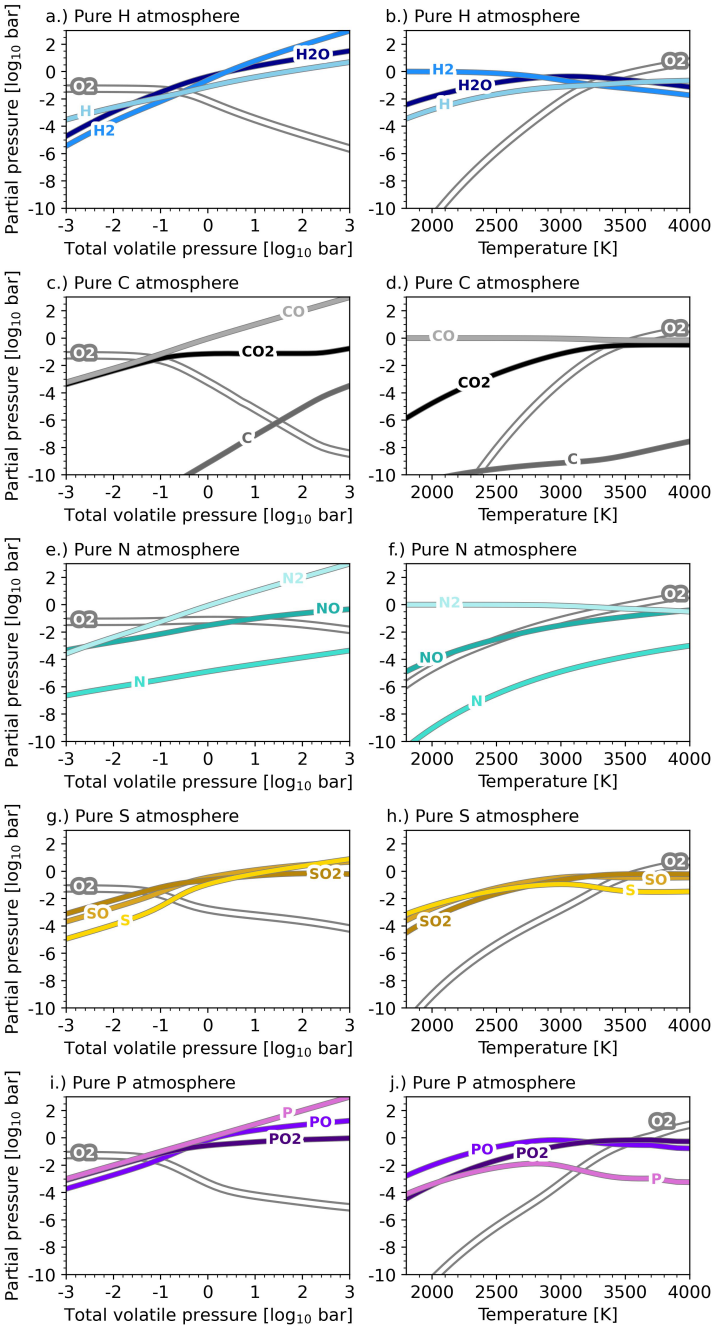


Figure 4.4: Behaviour of major volatile species in pure volatile atmospheres: For each of the tested pure volatile atmospheres, we show the behaviour of the major volatile species. The plots in the *left* column show partial pressures as a function of total volatile pressure at a fixed temperature of 3000 K. The plots in the *right* column show partial pressures as a function of temperature at a fixed total volatile pressure of 1 bar.

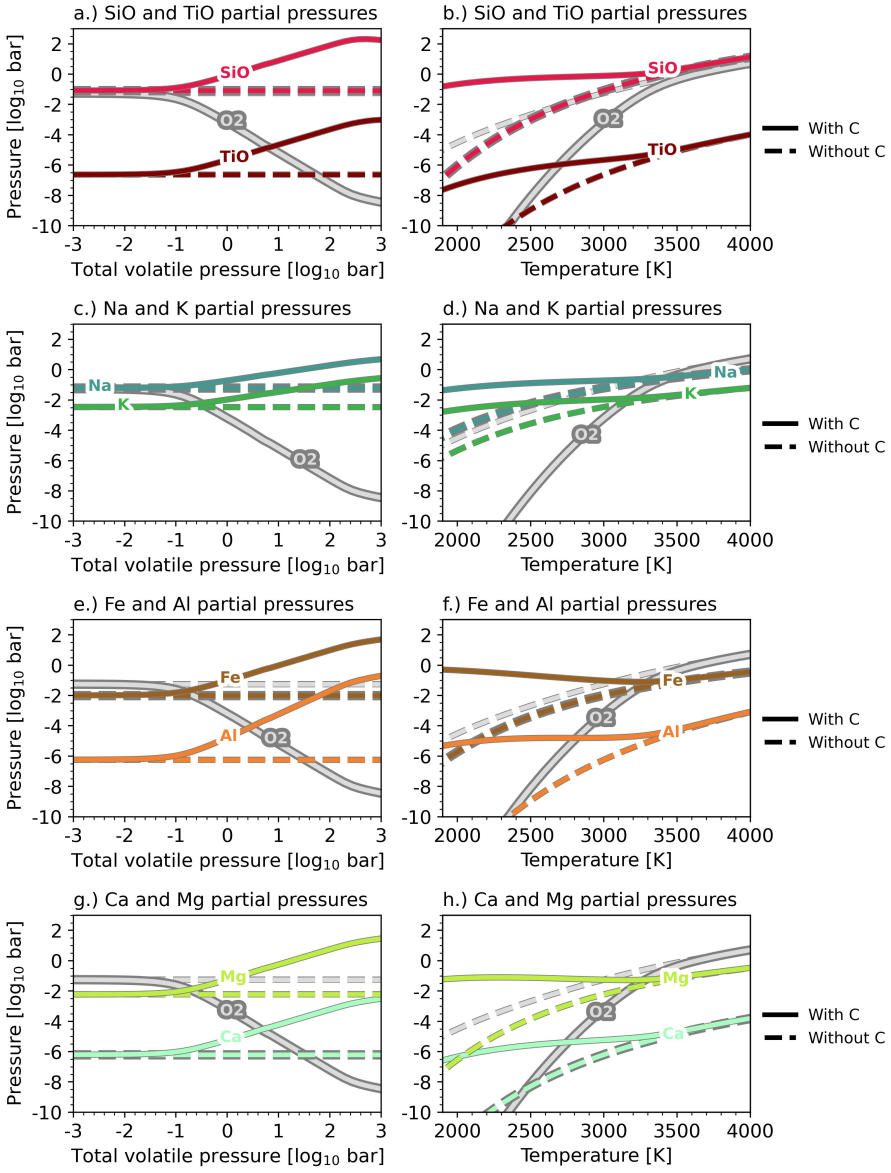


Figure 4.5: Effect of a pure C atmosphere: The partial pressures of selected vaporised species (O_2, SiO, TiO, Fe, Na, and K) in a pure C volatile atmosphere above a BSE lava ocean are shown using solid lines, while the dashed lines are used to indicate their partial pressures in volatile free atmospheres. In the bottom row (i and j) we also show the partial pressures of the dominant C species CO and CO_2. The left panels (a,c,e,g, and i) show the partial pressures as a function of total volatile pressure at a fixed surface temperature of 3000 K. The right panels (b,d,f,h, and j) show the partial pressures as a function of surface temperature at a fixed total volatile pressure of 1 bar.

0.2 bar (van Buchem et al. 2023). In panel *a* of Figure 4.3 we see that as the total volatile pressure goes beyond 0.1 bar there is a decrease in the O_2 partial pressure for all volatile atmospheres. The smallest decrease is for the N atmosphere, while the largest decrease is for the C atmosphere. This is because C is much more likely to form oxygenated species (e.g. CO_2 and CO) than N. This is demonstrated in Figure 4.4 when comparing panels *c* and *e*. In panel *c* the behaviour of the major carbon species is such that as the total volatile pressure increases, the CO partial pressure grows steadily along with an initial increase in CO_2 and a resulting decrease in O_2 partial pressure. In panel *e* we see that O_2 partial pressure decreases far less with increasing total volatile pressure due to only one of the major nitrogen species in the N atmosphere containing O (NO). From this same figure we can see that the C atmosphere is most effective at decreasing the O_2 partial pressure due to the fact that C is less prone to forming monoatomic species than the other four volatiles considered here.

In panel *c* we see that since SiO_2 is not dependent on O_2 partial pressure in its vaporisation reaction (equation 4.3), its partial pressure is barely affected by an increase in total volatile pressure for all atmospheres (except for the S atmosphere, see following subsection). SiO (panel *e*) and Si (panel *g*) partial pressures are affected, due to their dependence on O_2 partial pressure, and show strong increases in partial pressure with increasing total volatile pressure. The strength of the increase in the SiO and Si partial pressures is proportional to the strength in the decrease in O_2 partial pressures. Hence, a C atmosphere has the strongest effect, the N atmosphere the weakest, and the other three lie in between these two extremes.

The right column of Figure 4.3 shows that a decrease in O_2 partial pressures with decreasing lava ocean surface temperature (panel *b*) leads to an increase in SiO and Si partial pressures (panels *f* and *h*) relative to the volatile-free case but little to no change in SiO_2 partial pressure (panel *d*) relative to the case in which there are no volatiles in the atmosphere above the melt. At about 3500 K, partial pressure values converge with the non-volatile atmosphere case. This is due to the fact that the pressure of vaporised species increases exponentially as a function of temperature (van Buchem et al. 2023)), whereas the total volatile pressure is being held constant. Hence, the partial pressures of the vaporised species overwhelm those of the volatiles. Below about 3500 K, the atmosphere is dominated by volatiles. As the temperature decreases, what little O_2 is being released into the atmosphere combines with the volatiles which pushes the O_2 partial pressure even lower, leading to very strong increases in the partial pressures of the species which are dependent on O_2 in their vaporisation reactions (e.g. SiO and Si). Again, the strength of this effect is strongly dependent on the propensity of the volatile element to form oxygen-bearing molecules.

The behaviour of SiO_2, SiO, and Si as shown in Figure 4.3 is qualitatively representative for all species that form through vaporisation reactions from

the melt. Generally, the degree of partial pressure increase relative to the non-volatile case is dictated by the moles of O_2 released in the vaporisation reaction. In Figure 4.5 we show this for a selection of vaporised species which are likely candidates for detection in emission and/or transmission spectra of USP planets Zilinskas et al. (2022, 2023); Ito et al. (2015) in a 'pure' C atmosphere. We chose to show the effect of a C atmosphere due to it having the most pronounced effect on the partial pressure of the vaporised species. As in Figure 4.3, the left column shows partial pressures as a function of total volatile pressure, while the right column shows the partial pressures as a function of temperature.[4] All vapour species shown in this figure are strongly affected by the presence of a volatile atmosphere. It is noteworthy to point out that at around 2000 K, Fe may become the dominant vaporised species instead of Na due to this effect.

4.3.2 Effects of a complex volatile atmosphere

To understand the effects of volatile atmospheres on vaporisation when all five major volatile elements (C, H, N, S, P) are present in the same atmosphere, we modelled complex volatile atmospheres. It is, as of yet, not clear what the (volatile) composition of atmospheres on earth, super-earth, and sub-Neptune sized exoplanets is likely to be. The current consensus is that a wide range of different compositions is possible (Moses et al. 2013; Hu & Seager 2014; Guzmán-Mesa et al. 2022). We therefore consider four different 'archetypal' atmospheres that each represent a first order estimate of an atmosphere dominated by one specific element but which also contains the other four. These are not meant to represent accurate estimates of the volatile element abundances of specific HRE's, but rather to demonstrate the effect that complex volatile atmospheres have on vapour species. We tested five archetypes of atmospheres: C, H, N, and S dominated (see Table 4.1). The C dominated atmosphere is representative of the highly enriched (x10000 solar C/H) atmosphere tested in Moses et al. (2013), the H dominated atmosphere of a more solar-like atmosphere, the N dominated is similar to what we see on Earth and Titan, and finally the S dominated atmosphere represents what we could potentially expect on a highly volcanic planet (analogous to Io). Due to how similar the behaviour is of S and P, we decided to add a significant amount of P to the S dominated atmosphere instead of trying a separate case where P was the only dominant volatile element.

The effect of complex volatile atmospheres on the vaporised species is qualitatively the same as for the pure atmospheres (shown in Figures 4.13, 4.14, 4.15, and 4.16 in the Appendix) with the dominant volatile element dictating atmospheric chemistry.

One notable exception is the atmosphere with N as the dominant volatile, which is highlighted in Figure 4.6. In the first row, we see that the complex N dominated atmosphere leads to a significant increase in Si and SiO partial

[4]The full output for all these atmosphere types is available upon request from the author.

pressure at high total volatile pressures (right side of panel *a*) and at relatively lower temperatures (left side of panel *b*), compared to the pure N atmosphere and the case without volatiles. This indicates that N dominated atmospheres may also have significant amounts of vaporised species if some of the volatiles that are more prone to oxidation, such as C and H, are also present in the atmosphere. This is shown in the panels displaying the partial pressures of the volatile species in the atmosphere. In panels *c* and *d* it is shown how the complex atmosphere has a lower NO partial pressure than its pure counterpart due to the fact that O_2 is used up in the formation of CO, CO_2, and H_2O (panels *e*, *f*, *g*, and *h*). This leads to a lower O_2 partial pressure than in the pure atmosphere, together with increases in the SiO and Si partial pressures.

Expanding the number of chemical species included in LavAtmos 1 by using FastChem also enables us to study changes in partial pressures of vaporised species not only due to a change in the O_2 partial pressure, but also due to different species competing for the same element. Figure 4.7 shows some examples of this for a complex S dominated atmosphere (panel *a*) and a complex C dominated atmosphere (panel *b*) at a fixed temperature of 3000 K. In the S dominated atmosphere, SiO and TiO initially increase as the total volatile pressure increases. SiS and TiS are being formed simultaneously, and as the total volatile pressure reaches 10 bar, these S bearing species become the most abundant Si species and the partial pressures of SiO and TiO decrease. This behaviour can also be seen in panels *e* and *g* of Figure 4.3 for the pure S atmosphere. Figure 4.7*b* shows a feature that is unique to a complex volatile atmosphere that includes both C and N. Here, Na and K initially see an increase in partial pressure with increasing total volatile pressure, but as the total volatile pressure reaches 100 bar, NaCN and KCN become the dominant Na and K bearing species. This example serves to illustrate the importance of including a wide range of different chemical species in order to fully understand the behaviour of the major species over different temperatures and pressures.

4.4 Implications for a 55-Cnc e-like atmosphere

To assess the implications of our results, we modelled the composition at the surface-atmosphere boundary of a planet analogous to 55-Cnc e. Recent JWST observations of the emission spectrum of 55-Cnc e gathered using MIRI-LRS and NIRCam were published by Hu et al. (2024). The observed spectrum does not match that of a thin vaporised-rock atmosphere and instead matches better with the spectrum of a $\simeq$100 bar volatile atmosphere that would facilitate more efficient heat-redistribution. Furthermore, absorption features found in the NIRCam spectrum are consistent with CO and CO_2 features. This points to 55-Cnc e supporting a volatile atmosphere. These main conclusions are based on the differences between two end-member models: a volatile-free atmosphere and a volatile-bearing but rock-vapour-free atmosphere. Hu et al. (2024) also determined the range of physically plausible atmospheres on the planet us-

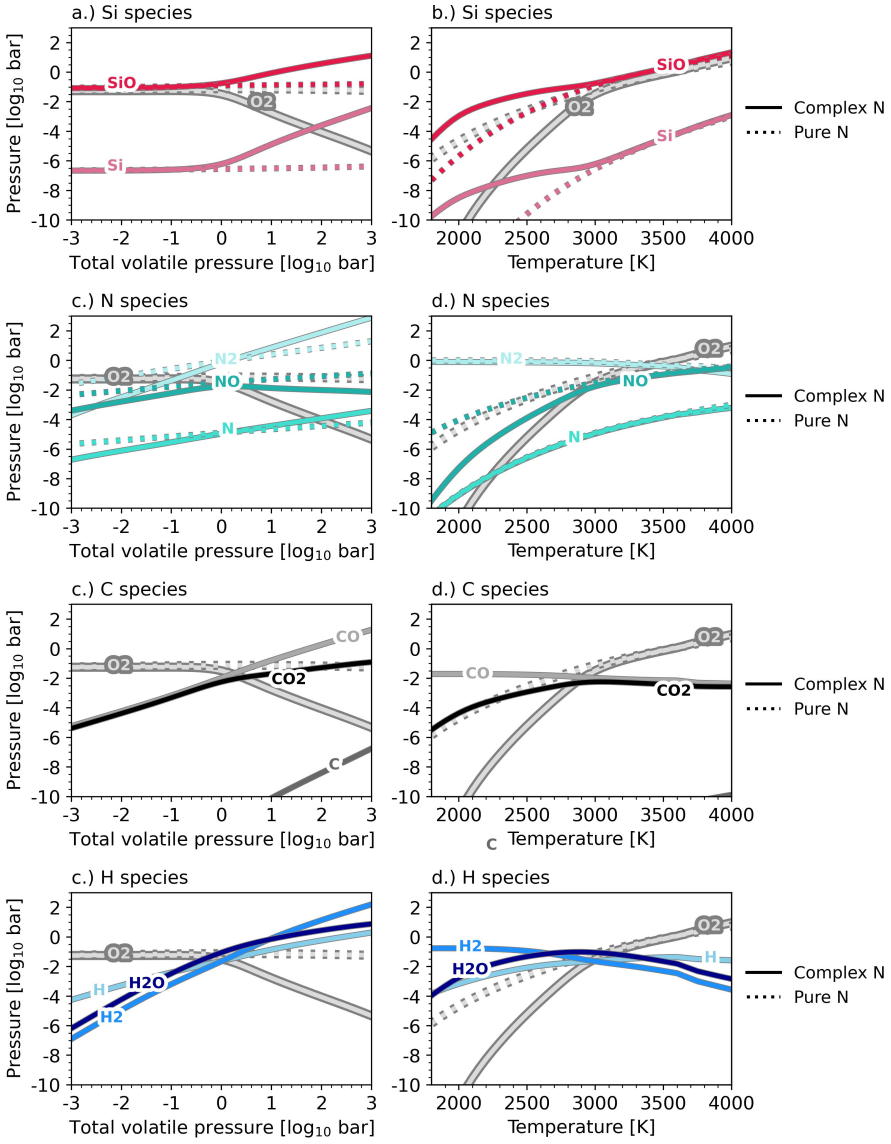


Figure 4.6: Chemistry of a N-dominated complex atmosphere: Shown here are the partial pressure of a selection of atmospheric species as a function of total volatile pressure at a fixed BSE lava ocean surface temperature of 3000 K in the left column (panels *a*,*c*, *e*, and *g*) and temperature at a fixed total volatile pressure of 1 bar in the right column (panels *b*,*d*, *f*, and *h*). The solid lines indicate partial pressures in a complex volatile atmosphere (see 'N dominated' in Table 4.1) and the dash dotted lines a pure N atmosphere.

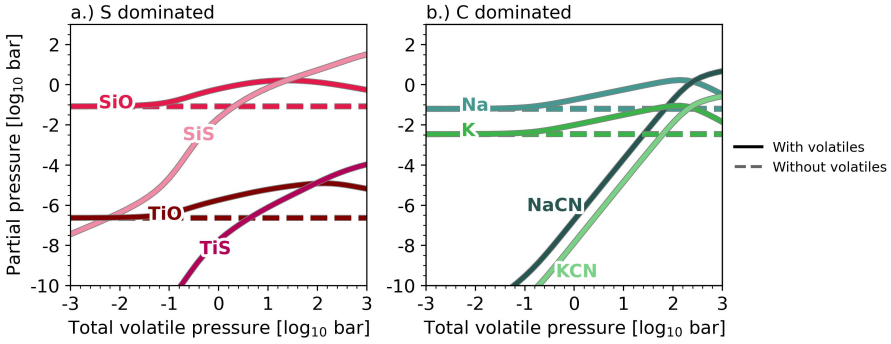


Figure 4.7: Behaviour of K, Na, Si, and Ti species in S- and C-dominated complex atmospheres: In both panels the calculated partial pressures of selected species are shown as a function of total volatile pressure. In the left panel (*a*), a S-dominated complex atmosphere yields a decrease in SiO and TiO partial pressure due to the formation of SiS and TiS, respectively. In the right panel (*b*) similar behaviour is seen in a C-dominated complex atmosphere where the partial pressures of Na and K decrease due to the formation of NaCN and KCN, respectively. Calculations for both panels were done for a fixed BSE lava ocean surface temperature of 3000 K.

ing self-consistent atmospheric models that contained both rock-vapour and volatiles.

Of these self-consistent atmospheric models, the majority were run assuming only volatile species in the atmosphere without a lava ocean feeding rock-vapour species into it. These models indicate that the best fitting atmosphere is one containing abundant CO_2 with a surface temperature of about 2500 K. Some models included species from both lava vaporisation and volatile species, using the approach described in Zilinskas et al. (2023), which is similar to the approach of Piette et al. (2023). The abundances of the vaporised species were calculated without taking the influence of volatile species on vaporisation into account. These abundances were then added to the total abundances of the atmosphere. We refer to this as the 'volatile-free vaporisation' method (which is analogous to the 'sum' method used in the work of Falco et al. (2024)). This approach gave an overall worse fit to the JWST data than the volatile-only scenario, but did indicate that a reasonable fit could be made with a higher surface temperature of a bit less than 3000 K.

Finally, Hu et al. (2024) tested a third type of model in which the vaporisation calculations used an early version of the code presented in this paper. This led to a large increase in the abundance of the vaporised species in the atmosphere, causing a strong inversion of the temperature-pressure profile and yielding a spectrum with strong emission features. This shows that if the conflicting data points observed around 4.5 micron by previous observations of 55-Cnc e with Spitzer (Demory et al. 2016b,a) are indeed physical, this could

potentially be explained by an influx in vaporised species into the atmosphere of 55-Cnc e. This model also provides a potential fit with a significantly lower surface temperature of only 2000 K.

From these models, one can conclude (a) that a wide range of different surface temperatures could potentially explain the observed emission spectrum of 55-Cnc e and (b) that abundances of rock-vapour species in the atmosphere have important implications for the thermal structure of the atmosphere and resulting emission/absorption features of the spectrum. Here we assess the extent to which the Hu et al. (2024) results are affected when using LavAtmos 2.0. We decided to see how two of the best fitting volatile atmosphere compositions from Hu et al. (2024) affect vaporisation when coupled to a lava-ocean.

We selected two model atmospheric volatile compositions with very different C abundances (see Table 4.1) which both show a good fit to the observed spectra of 55-Cnc e. As we have seen in the previous section, the presence of C in the atmosphere has a strong effect on the vaporisation of melt species. We labelled the compositions based on their C abundances, with one named carbon poor (C w% = 9.09e-6) and the other named carbon rich (C w% = 0.91).

For these two volatile compositions we plotted the partial pressures, calculated using both LavAtmos and the volatile-free vaporisation method, of O_2 along with important vaporised species (SiO, SiO_2, Na, and K) in Figure 4.8 and the partial pressures of volatile species with strong spectroscopic signatures (CO, CO_2, H_2O, and SO_2) in Figure 4.10. It is important to note that the partial pressures of the volatile-free vaporisation method are calculated by first deriving the partial pressures of the vapor species while assuming that no volatile species are present. From these partial pressures, the elemental abundance of the vaporised elements (O, Si, Mg, Al, Ti, Fe, Ca, Na, and K) are derived, which are then combined with the elemental abundances of the volatile elements (C, H, N, S, and P) and provided as input to FastChem 3 (Stock et al. 2018; Kitzmann et al. 2024), which calculates the partial pressures of the chemical species at the desired TP point.

Similar to the previous section, we show output for a fixed temperature and varying the total volatile pressure in the panels in the left column and a fixed total volatile pressure but varying temperature in the right side column. We use a fixed surface temperature of 2500 K and a fixed total volatile pressure of 10 bar. These values fall in the middle of the range of total volatile pressures and surface temperatures (indicated using the blue and red shaded regions in Figures 4.8 and 4.10) that could be realistically expected based on the tested self-consistent models in Hu et al. (2024) as summarised above.

In this section, we first draw attention to the differences in composition that the two approaches ('volatile-free vaporisation' and the method presented in this paper) of calculating the composition of melt-vapour in a volatile atmosphere can give. We then look at how the presence or absence of a lava-ocean at the base of a volatile atmosphere could be reflected in its composition.

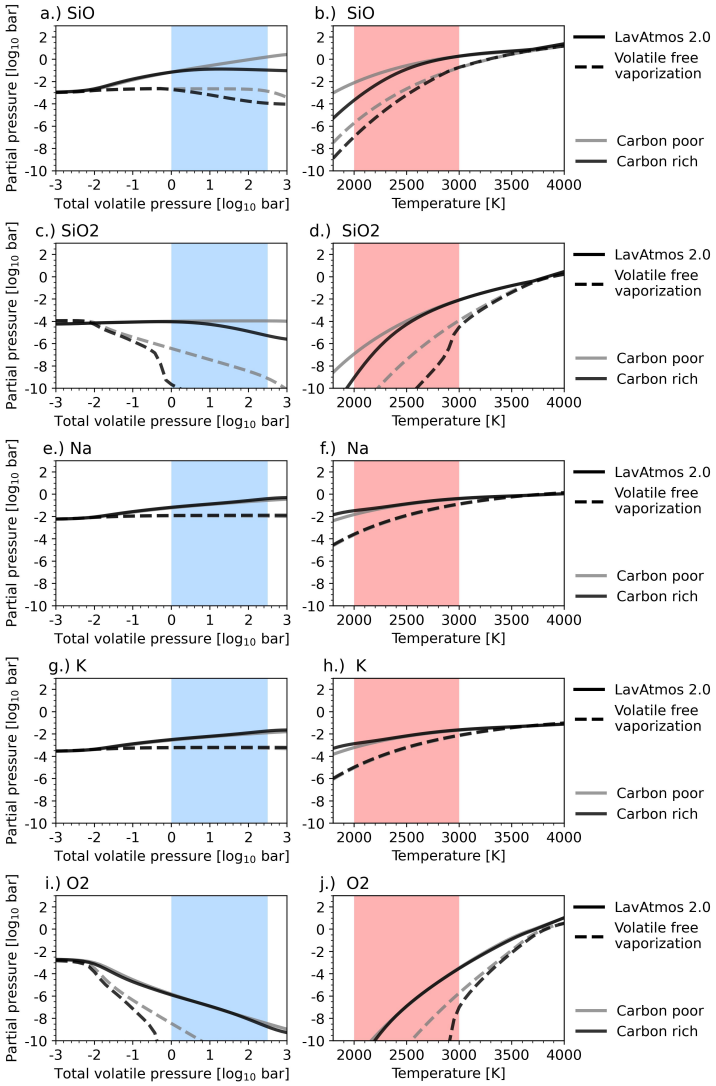


Figure 4.8: Computed partial pressures of vaporised species in a 55-Cnc e like atmosphere: Shown here are the partial pressures of SiO (panels *a* and *b*), SiO_2 (panels *c* and *d*), Na (panels *e* and *f*), K (panels *g* and *h*), and O_2 (panels *i* and *j*). The solid lines indicate the partial pressures calculated using LavAtmos 2.0 (this study), and the dashed lines show the partial pressures calculated when using the volatile-free vaporisation approach (LavAtmos 1). Two volatile atmosphere compositions are tested (see Table 4.1) of which one is carbon poor ($\simeq$0.01 w% C, grey) and the other carbon rich ($\simeq$10%, black). The left-hand panel shows partial pressures plotted as a function of the total volatile pressure of the atmosphere at a fixed temperature of 2500, and the right-hand panel as a function of surface temperature at a fixed total volatile pressure of 10 bar. The blue area indicates the estimated surface pressure range of 55-Cnc e and the red area indicates the estimated surface temperature range of 55-Cnc e (Hu et al. 2024).

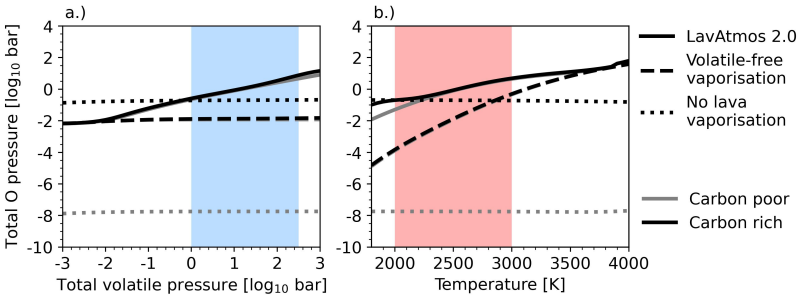


Figure 4.9: Total O pressure in a 55-Cnc e like atmosphere: Shown here are the total O pressure of two different volatile atmosphere compositions - carbon poor (*grey*) and carbon rich (*black*) as a function of total volatile pressure (panel *a*) at a fixed temperature of 2500 K and as a function of temperature at a fixed total volatile pressure of 10 bar (panel *b*). The total O pressures indicated using the solid lines are calculated using the method outline in this paper, those indicated using the dashed line are calculated using the volatile-free vaporisation method, and the dotted line indicates the total O pressure when no lava ocean vaporisation is assumed. The blue area indicates the estimated surface pressure range of 55-Cnc e and the red area indicates the estimated surface temperature range of 55-Cnc e (Hu et al. 2024).

4.4.1 Vaporised partial pressure comparison between LavAtmos 2.0 and the volatile-free vaporisation method

Looking first at the total volatile pressure dependent plots in the left-side column of Figure 4.8, we see how at low total volatile pressure the partial pressures calculated by LavAtmos 2.0 and the volatile-free vaporisation method are in agreement. At these conditions, the abundances of volatile species are too low to have a significant effect on the vaporisation. As we move to the right in these plots, the partial pressures calculated by the two methods start to diverge around 1e-2 bar for all species. This is due to the fact that at the surface temperature at which the volatile pressure dependent calculations were made (2500 K) the total vapour pressure above a melt of BSE composition in a volatile-free atmosphere is around 1e-2 bar (Visscher & Fegley 2013; Ito et al. 2015; van Buchem et al. 2023). As the total volatile pressure nears and then surpasses this point, it starts dominating the atmosphere.

As we have seen in section 4.3, the presence of volatile elements in the atmosphere leads to a drop in O_2 partial pressure, which leads to an increase in the vaporisation of species for which O_2 is released in their vaporisation reaction. This effect occurs here as well, as SiO, Na, and K all exhibit increasing partial pressures relative to the volatile-free vaporisation case once the total volatile pressures go beyond 1e-2 bar.

This may appear to be in contradiction to what we see in the bottom two panels (i and j) where the O_2 partial pressure of the volatile-free atmosphere

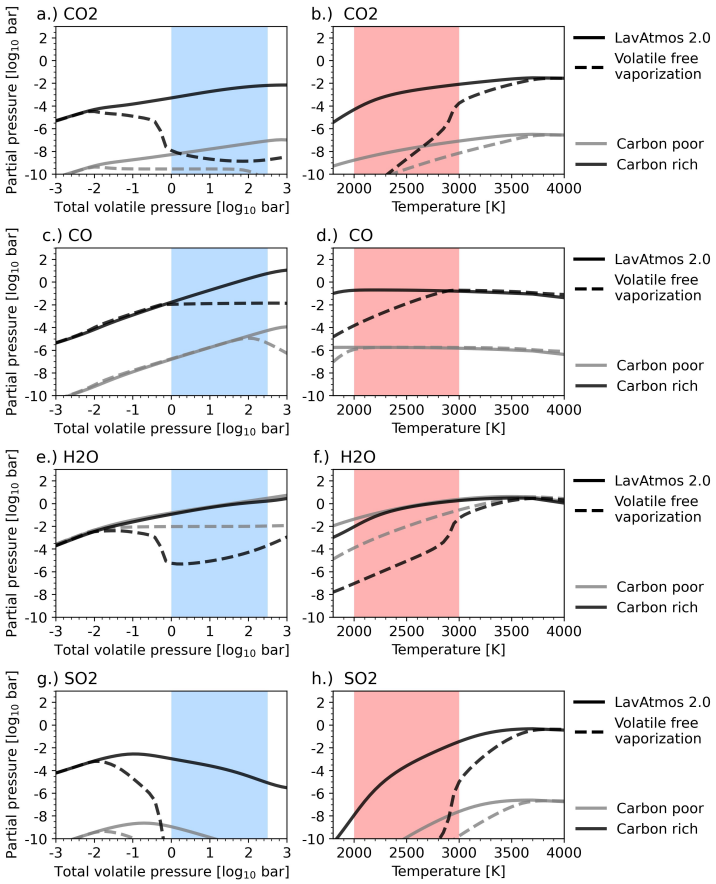


Figure 4.10: Computed partial pressures of volatile species in a 55-Cnc e like atmosphere: Shown here are the partial pressures of CO (panels *a* and *b*) CO_2 (panels *c* and *d*), H_2O (panels *e* and *f*), SO_2 (panels *g* and *h*). The solid lines indicate the partial pressures calculated using LavAtmos 2.0 (this study) and the dashed lines show the partial pressures calculated when using the volatile-free vaporisation approach. Two volatile atmosphere compositions are tested (see Table **??**) of which one is carbon poor ($\simeq$0.01 w% C, grey) and the other carbon rich ($\simeq$10%, black). The left-hand panel shows partial pressures plotted as a function of the total volatile pressure of the atmosphere at a fixed temperature of 2500, and the right-hand panel as a function of surface temperature at a fixed total volatile pressure of 10 bar. The blue area indicates the estimated surface pressure range of 55-Cnc e and the red area indicates the estimated surface temperature range of 55-Cnc e (Hu et al. 2024).

is lower than that of LavAtmos 2. However, this is a product of how the volatile-free vaporisation approach works. As explained at the start of section 4.4, the volatile-free vaporisation approach first calculates the abundance of the vaporised elements and only then combines them with the volatile elements to calculate the chemical composition of the atmosphere. Hence, during the vaporisation calculations, the O_2 found using the volatile-free vaporisation method is indeed greater than for LavAtmos 2 (similar to what we see in Figure 4.5). It is once these partial pressures are converted to abundances, combined with the volatile elements, and the partial pressures are re-calculated, that the resulting O_2 partial pressure is decreased due to the formation of oxygenated species such as H_2O and CO_2.

This indirectly illustrates another distinction between the volatile-free vaporisation approach and LavAtmos 2, which is that including volatile species in the vaporisation reactions leads to an increase in the amount of O in the atmosphere. This is shown explicitly in Figure 4.9, where we plot the total O pressure for all three models as a function of total volatile pressure (panel *a*) and temperature (panel *b*). In both panels the O abundance of the atmosphere without lava vaporisation is fixed - as expected since the O abundance is set a-priori (see Table 4.1). For the volatile-free vaporisation case, the O abundance is fixed in the total volatile pressure plot (*a*) because the presence of the volatile species does not affect the vaporisation - which is also why the same O abundance is found for both volatile compositions. LavAtmos 2 does see an increase in O abundance with increasing total volatile pressure of up to three orders of magnitude with respect to the volatile free case. In panel *b* in Figure 4.9, the total O pressure of the volatile-free vaporisation method increases with temperature, coinciding with the increase in vaporisation with higher temperatures. Here we also see that LavAtmos 2 gives a greater total O pressure due to the presence of the volatile species.

It may feel counter-intuitive that the inclusion of volatile species in the vaporisation reaction leads to an increase in O elemental abundance in the atmosphere, while we have been discussing how a drop in O_2 partial pressure is what is causing an increase in vaporisation partial pressures. However, this makes sense if one considers that a drop in O_2 partial pressure is due to the formation of oxygenated species with volatile elements. As such, the O is not being removed from the atmosphere. Simultaneously, the increase in vaporisation of melt oxides due to a drop in O_2 partial pressure leads to an increase in the amount of O being released into the atmosphere.

The difference in O abundance between the two approaches is also reflected in the decrease of the partial pressure of O bearing vapour species such as SiO and SiO_2 at high total volatile pressures (panels *a* and *c*). As the total volatile pressure increases, causing a drop in O_2 partial pressure, SiO_2 partial pressure and to a lesser extend SiO partial pressure decrease significantly in the volatile-free vaporisation approach. The increased O abundance seen in LavAtmos 2 entails that this effect is far less pronounced, affecting the carbon rich atmo-

sphere more so than the carbon poor atmosphere due to the propensity of C to form oxidized species.

In the right-side column in Figure 4.8, we see that at high temperatures the partial pressures calculated by LavAtmos 2.0 and the volatile-free vaporisation method generally have overlapping values. As temperature decreases, they start to diverge around 3600 K. This coincides with the temperature at which the total vaporised pressure in a volatile-free atmosphere is $\simeq$ 10 bar (Visscher & Fegley 2013; Ito et al. 2015; van Buchem et al. 2023), which is the fixed total volatile pressure at which these plots were made. As temperature decreases further, the volatile atmosphere is dominant over the rock-vapour. As we decrease further in temperature, all partial pressures drop, but those calculated using LavAtmos 2.O do not drop as quickly due to the presence of the volatiles lowering the O_2 partial pressure. The drop in partial pressures of SiO and SiO_2 of the volatile-free vaporisation method are accelerated further due to the volatile species competing with Si for O.

With the exception of vapour atmosphere dominated regimes (at low total volatile pressure and high surface temperature), we see that the volatile-free vaporisation method systematically leads to an underestimation of the partial pressures relative to LavAtmos 2.0. The most significant effects are seen for SiO and SiO_2. Within the total volatile pressure and temperature ranges (indicated in red and blue respectively) that could be expected on 55-Cnc e (Hu et al. 2024), the differences in partial pressure between these two approaches are of one to several orders of magnitude. This could potentially mean that the spectral emission features of SiO and SiO_2 may not be as suppressed by volatile atmospheres as currently thought (Zilinskas et al. 2023; Piette et al. 2023). The differences between the two methods that we see in the partial pressures of Na and K could be of relevance for the thermal structures of atmospheres, which can be heavily influenced by an increase in short-wave absorbers such as Na and K. These findings align with the work by Falco et al. (2024), which suggests that hydrogen-rich atmospheres may contain sufficient abundances of vaporised species for a thermal inversion to occur.

4.4.2 The effect of lava oceans on atmospheric volatile species

In Figure 4.10 the change in partial pressure of spectroscopically important volatile species is shown for LavAtmos 2.0 and the volatile-free vaporisation method. Similarly to what we saw in section 4.4.1, at low total volatile pressure and high temperature the system is dominated by the vaporised species and the two methods have very similar outputs. However, as we move into the volatile dominated regimes, beyond 1e-2 bar in the total volatile pressure dependent plots and below 3600 K in the temperature dependent plots, we again start seeing large differences between the two approaches.

The differences we see for the volatile species can all be attributed to the

fact that in LavAtmos 2.0 the presence of volatiles leads to an increase in the total O elemental abundance with respect to the the volatile-free vaporisation method as seen in the previous section and shown in Figure 4.9. Hence, as the volatile contents of the atmosphere increase, far fewer oxidized species can be formed when compared to the partial pressure from LavAtmos 2.0. In the left column of Figure 4.10, we can see that this effect is most pronounced in the fully oxidized species CO_2, H_2O, and SO_2. As the total volatile pressure increases beyond 1e-2 bar into the volatile dominated regime, the partial pressures of these species as calculated using the volatile-free vaporisation method decrease significantly while we see a gradual increase for LavAtmos 2.0. At around 1 bar, we see a very strong drop in CO_2 partial pressure for the carbon rich atmosphere. This can be attributed to the total elemental C abundance (about 1% of the total volatile atmosphere composition as per Table 4.1) reaching a point where it dominates over the O elemental abundance in the system. This is also reflected in the CO partial pressure; once the total volatile pressure passes 1 bar, there is too little O in the volatile-free vaporisation model to produce additional CO and the partial pressure remains constant.

Looking at the temperature dependent plots in the right-hand side column of Figure 4.10, we see that in the volatile dominated regime (below $\simeq$3600 K) the fully oxidised species show a strong decrease in partial pressure. This is due to the size of the vapour atmosphere being strongly dependent on temperature. As the amount of vapour in the atmosphere decreases, so does the total O elemental abundance (see panel *b* in Figure 4.9). As expected, this decrease is much stronger in the volatile-free atmosphere than for LavAtmos 2.0 thanks to the increased vaporisation due to the presence of volatile species. For CO we see a slight increase in partial pressure with decreasing temperature; this is due to a lower O_2 environment favouring CO formation over CO_2. At 2900 K we then see that the volatile-free vaporisation method diverges from LavAtmos 2.0 (going from high to low temperatures) as there is no longer sufficient O being vaporised. The point at which this occurs is dependent on the total volatile pressure of the atmosphere. For higher total volatile pressures, a higher O abundance is required to sate the formation of oxidised species, while the inverse is true for lower total volatiles pressures - moving this point of divergence/convergence between the models up and down in temperature accordingly.

Overall, when in a volatile pressure and temperature regime where the volatile atmosphere is dominant, LavAtmos 2.0 leads to volatile species in the atmosphere being more oxidised than when using the volatile-free vaporisation method. This leads to the two methods having large differences in partial pressures of volatile species when compared to each other. Especially for the oxidised species, we see difference of more than six orders of magnitude within the total volatile pressure and temperature ranges (indicated in blue and red respectively) expected on 55-Cnc e (Hu et al. 2024). This is especially significant due to the fact that these are all species that have strong opacities within

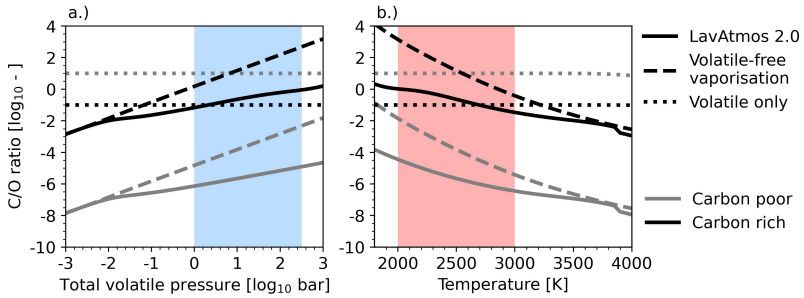


Figure 4.11: C/O ratio in a 55-Cnc e like atmosphere: Shown here are the C/O ratios of two different volatile atmosphere compositions - carbon poor (*grey*) and carbon rich (*black*) as a function of total volatile pressure (panel *a*) at a fixed temperature of 2500 K and as a function of temperature at a fixed total volatile pressure of 10 bar (panel *b*). C/O ratios indicated using the solid lines are calculated using the method outline in this paper, those indicated using the dashed line are calculated using the volatile-free vaporisation method, and the dotted line indicates (constant) C/O ratio when no lava ocean vaporisation is assumed. The blue area indicates the estimated surface pressure range of 55-Cnc e and the red area indicates the estimated surface temperature range of 55-Cnc e (Hu et al. 2024).

both the optical and the infrared and could therefore have large implications for the emission spectra of these atmospheres.

In order to have a more general view of the differences between the two approaches, we plotted the C/O ratios of each tested case in Figure 4.11. As one would expect, we again see a comparable trend to what we saw in Figures 4.8 and 4.10 where the output of LavAtmos 2.0 and the volatile-free vaporisation method coincide within the vapour dominated regimes at low total volatile pressure and high surface temperature. The divergence happens once we enter the volatile dominated regimes (above about 1e-2 bar and below about 3600 K). In both the total volatile pressure and temperature plots, the increased O abundance seen in LavAtmos 2.0 output in the presence of volatile leads to a lower C/O ratio than the volatile-free vaporisation method. The volatile-free vaporisation method has a fixed atmospheric elemental O abundance for a given temperature, hence why we see a linear increase in the C/O ratio in the total volatile pressure dependent plot (panel *a*). Again, we see that within the range of expected possible pressures and temperatures on 55-Cnc e (blue and red regions respectively) there are significant differences between the two approaches of several orders of magnitude.

Figure 4.11 also includes the fixed C/O abundances of the two hypothetical 55-Cnc e atmosphere compositions (see Table 4.1) so as to represent the case where no lava vaporisation is taken into account, hence it is labelled as 'volatile-only'. We would like to point out that one needs to be careful with the interpretation of this plot, due to the fact that these are two fundamentally

different approaches. In the LavAtmos 2.0 and the volatile-free vaporisation model, it is assumed that all of the oxygen in the atmosphere comes from the vaporisation of the melt species in the lava ocean, whereas for the volatile only we assume the O composition given in Table 4.1, which is the O abundance found to fit for these atmospheres in Hu & Seager (2014). Nonetheless, we consider it a worthwhile exercise to compare the calculated C/O ratios using the vaporisation methods to the fixed C/O found to give a good fit to the 55-Cnc e data, as it allows us to see how the C/O ratio varies as a function of total volatile pressure and temperature relative to values that are consistent with observations (the large majority of the tested models had C/O ratio's within the range of these two selected models).

In panel *a* we see that the C/O ratio calculated by LavAtmos 2.0 for a carbon rich atmosphere matches the fixed C/O ratio of the volatile-only atmosphere well between total volatile pressures of about 1 to 10 bar. In panel *c*, we see a similar match around about 2700 K. Both within the expected possible pressure and temperature ranges of 55-Cnc e. For the volatile-free vaporisation case, the C/O ratio crosses the volatile-only lines well outside of the possible pressure and temperature range at around 7e-2 bar and 3250 K. In the case of the carbon poor atmospheres, neither model is able to come even close to the C/O ratio of the volatile-only atmosphere.

If 55-Cnc e does indeed have a lava ocean at the base of its atmosphere that is also large enough to buffer the O_2 partial pressure of the system, then a carbon rich atmosphere with the composition given in Table 4.1 that is in equilibrium with a lava ocean, could give a C/O ratio that matches the C/O ratio of a volatile only atmosphere that is found to give a good fit to the emission spectrum. This is not the case for the carbon poor atmosphere.

We wish to stress that these outcomes are based on all of the above mentioned assumptions, along with a number of important caveats discussed in the following section. We therefore do not think that these findings provide sufficiently strong evidence to draw firm conclusions about the possible composition of the atmosphere of 55-Cnc e. However, this analysis does show that having a lava ocean in direct contact with a volatile atmosphere can have significant effects on the atmospheric oxidation state and needs to be considered in the future for a proper interpretation of the observational data of potential lava planets.

4.5 Discussion

4.5.1 Effect of water on melt activities

One of the effects that is not taken into account in this work is that of the dissolution of volatile species in the lava ocean. Volatile species such as H_2O and CO_2 can exhibit high solubility in silicate melts at elevated pressure (Sossi et al. 2023). In order to understand the extent to which dissolved water in the melt

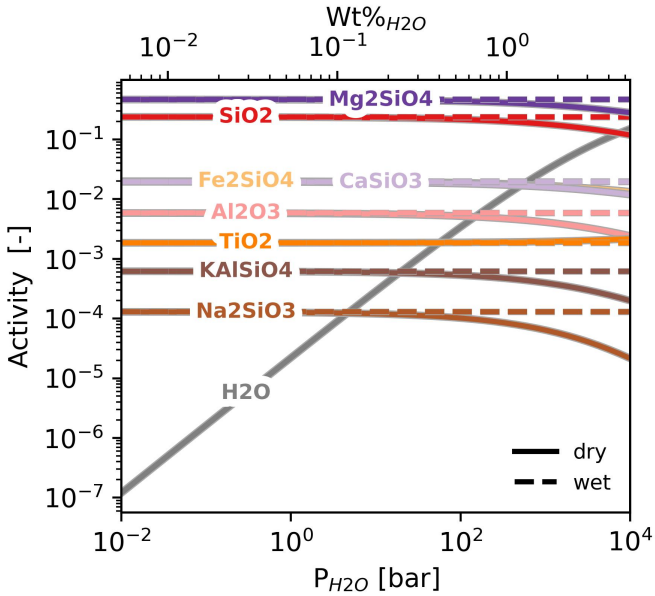


Figure 4.12: Effect of water dissolution in melt on melt endmember component activities: An increasing weight percentage of water in a melt leads to a decrease in the activities of the different endmember components. However, this change in activity is too small to have an effect on the outgassing of the vapour species that is detectable in thermal emission spectra. Sossi et al. (2023) was used to estimate the solubility of water in silicate melt.

may affect lava outgassing, we assumed parametrisations of the solubility of water in peridotite as derived by Bower et al. (2022), and used MELTS (Ghiorso & Sack 1995) to calculate the activities of different melt species (assuming BSE composition) as a function of increased dissolved water abundance. In Figure 4.12 we plotted the activity of key melt species with the H_2O weight percentage on the top x-axis and the corresponding partial pressure of atmospheric H_2O on the bottom x-axis. The dashed lines indicate the activities within a dry melt (unchanging) and the solid lines the activity in a melt saturated in water. From a P_{H2O} of about 10^2 bar (corresponding to about 0.5% weight percentage) we see significant decreases in the activities of the melt species. This likely means that, beyond an H_2O partial pressure of 100 bar, there could be a relative decrease in the partial pressure of vaporised melt species. Further work is required to quantify whether or not this could offset the increase in vaporised species due to the presence of volatile species. CO_2 may also affect the activity of the melt species (Dixon et al. 1995). For this work however, we never go above H_2O partial pressures of 30 bar (see Figure 4.10) and therefore this effect is not significant for our results.

4.5.2 Water in melt as a source of oxygen

Another effect that is overlooked with the current approach of not including water in the melt is related to the potential role of water as an additional source of oxygen. As long as the magma reservoir is sufficiently large to control the system's oxygen fugacity, including water in the melt vaporisation reactions would increase the total oxygen budget of the system and hence would lead to an increase in the O_2 partial pressure of the atmosphere. This would in turn lead to a decrease in the partial pressures of the vaporised species relative to what we are seeing in the current approach. It would, however, lead to an even lower C/O ratio than we are currently finding. The same holds for CO_2, albeit to a lesser extent due to its lower solubility relative to water. Implementing this effect in our model and determining at what weight percentages this could become significant is beyond the scope of the present study. We note that a significant weight percentage of water dissolved in lava would be required to have a noticeable effect on the atmosphere. As seen in Figure **??**, this would require an H_2O partial pressure in excess of 100 bar.

4.5.3 How to identify a surface lava ocean from atmospheric composition

Although many observations have already been dedicated to detecting signs of surface lava oceans on hot-rocky exoplanets (e.g. Zieba et al. 2022; Rasmussen et al. 2023; Hu et al. 2024; Zhang et al. 2024b), we have yet to find conclusive evidence for their presence. It is thought that in the absence of volatile species, SiO and SiO_2 features in the infrared are the easiest way to detect the presence of lava oceans interacting with the atmosphere (Ito et al. 2015; Zilinskas et al. 2022). Understanding the full effect of the increase in partial pressures of vaporised species on the calculated emission spectrum of a planet requires the development of self-consistent 1D models and is beyond the scope of this work. However, looking at the partial pressures of the difference species provides some hints as to what signs we should look for to deduce the presence of a surface lava ocean at the base of a volatile atmosphere.

One of the main outcomes of this study is that vaporised species may be easier to detect in volatile (C, H, N, S, and P) atmospheres than previously thought (Zilinskas et al. 2023; Piette et al. 2023). This supports the conclusion drawn from the study by Charnoz et al. (2023) who found that including H in the atmosphere of a lava planet increases that partial pressure of vaporised species. This is due to the fact that the presence of volatile species leads to a decrease in O_2 partial pressure, which leads to an increase in vapor species in the atmosphere.

Both Zilinskas et al. (2023) and Piette et al. (2023) found that the presence of a volatile atmosphere tends to suppress the spectroscopic signatures of SiO and SiO_2, the abundances of which were calculated using the volatile-free vaporisation method. This may change with an increase in partial pressures of

the vaporised species as found using LavAtmos 2. This is especially the case if we look at surface temperatures around 2000 K, where the relative increase in SiO partial pressure (see Figure 4.3) is greatest, even with a total volatile pressure of 1 bar. Similar conclusions can be drawn for Na and K. Furthermore, Falco et al. (2024) have shown that including volatile species in vaporisation reactions not only changes the chemistry of the atmosphere of a planet, but also its thermochemical structure.

Section 4.4.2 illustrates the influence that the presence of a lava ocean can have on the composition of a volatile atmosphere. We find that having an atmosphere in thermochemical equilibrium with a lava-ocean leads to it being able to drawn from a large reservoir of O. This leads to a higher elemental O abundance and a lower C/O ratio than what one might expected without the presence of a lava ocean. A low C/O ratio could therefore potentially provide some circumstantial evidence for the presence of a surface lava-ocean at the base of a volatile atmosphere. This conclusion holds as long as the main O reservoir in the atmosphere-lava-ocean system is the lava-ocean (i.e., the ocean needs to be deep enough compared to the thickness of the atmosphere for this conclusion to hold). An estimate of the needed depth of a lava ocean to be able to effectively buffer an overlying vapour only atmosphere was made by Seidler et al. (2024). They find that, depending on the temperature of the melt and its oxygen fugacity, a minimum lava ocean depth of anywhere from 10^{12} to 10^{6} m is necessary. The addition of volatiles and the resulting decrease in O_2 partial pressure would lead to a decrease in the required depth according to this approach. Quantitative estimates would require comprehensive interior modelling outside of the scope of this work.

4.6 Conclusion

We present LavAtmos 2.0, an updated version of LavAtmos which makes use of FastChem (Stock et al. 2018, 2022; Kitzmann et al. 2024) gas-equilibrium capabilities to include volatile species in vaporisation calculations. We found that including volatile elements in chemical equilibrium vaporisation calculations for a melt in contact with an atmosphere leads to an increase in the partial pressure of the vaporised species. We show that this holds true for all tested volatile atmospheres which include C, H, N, S, and P. The strength of the relative increase in the partial pressure of the vaporised species is positively correlated with the total volatile pressure in the atmosphere and inversely proportional to the surface temperature of the melt. Of all the tested volatile elements, C has the strongest effect on the increase in outgassing and N the weakest. This work confirms and matches the work done by Charnoz et al. (2023) and Falco et al. (2024) for hydrogen atmospheres.

To understand the behaviour of the chemical composition along the full range of possible temperatures and structures, it is important to include the effect of different volatile elements and species and hence justifies the use of a

more complex chemical model with regard to previous studies. Simply adding volatiles as passive additional components to a calculated vaporisation atmosphere as done in some previous studies tends to underestimate the partial pressures of vaporised species as well as the C/O ratio of the atmosphere.

The increase in the partial pressure of vaporised species due to the presence of volatiles could make species such as SiO, SiO_2, Na, and K easier to detect, making them suitable tracers for the indirect detection of surface lava oceans on USP planets. Our results also suggest that the oxidation state of an atmosphere is strongly influenced by the presence of a significant lava ocean with which it equilibrates, because a lava ocean provides a large reservoir of O for the atmosphere to tap from. This is reflected in the large differences (up to six orders of magnitude) in the partial pressures calculated by LavAtmos 2.0 with respect to the volatile-free vaporisation method of spectroscopically important volatile species (CO_2, CO, H_2O, and SO_2). Based on this, we find that a low C/O ratio could be a potential indication that a surface lava ocean is present on a USP planet with a volatile atmosphere. In any case, this work shows the importance of self-consistently modelling the interaction between a volatile-rich atmosphere and a lava ocean when interpreting atmospheric models of HREs.

Future work will be focused on modelling the implications for the chemical and thermodynamic structure of the atmospheres of HREs and the potential changes in emission spectra with respect to previous models.

Acknowledgements

We would like to thank the anonymous reviewer for the insightful comments and constructive feedback. This work was supported financially through a Dutch Science Foundation (NWO) Planetary and Exoplanetary Science (PEPSci) grant awarded to Y.M. and W. van W. Y.M and M.Z. acknowledge funding from the European Research Council (ERC) under the European Union's Horizon 2020 research and innovation programme (grant agreement no. 101088557, N-GINE).

Appendix

4.A Effect of complex volatile atmospheres on vaporised species

Generally, complex volatile atmospheres have a similar effect on the vapour species as pure volatile atmospheres. The most important differences are outlined in section 4.3 and the relevant species were plotted separately in Figures 4.6 and 4.7. The behaviour of each of these vaporised species may still be of interest to those seeking to interpret potential atmospheric compositions and hence were added to the appendix.

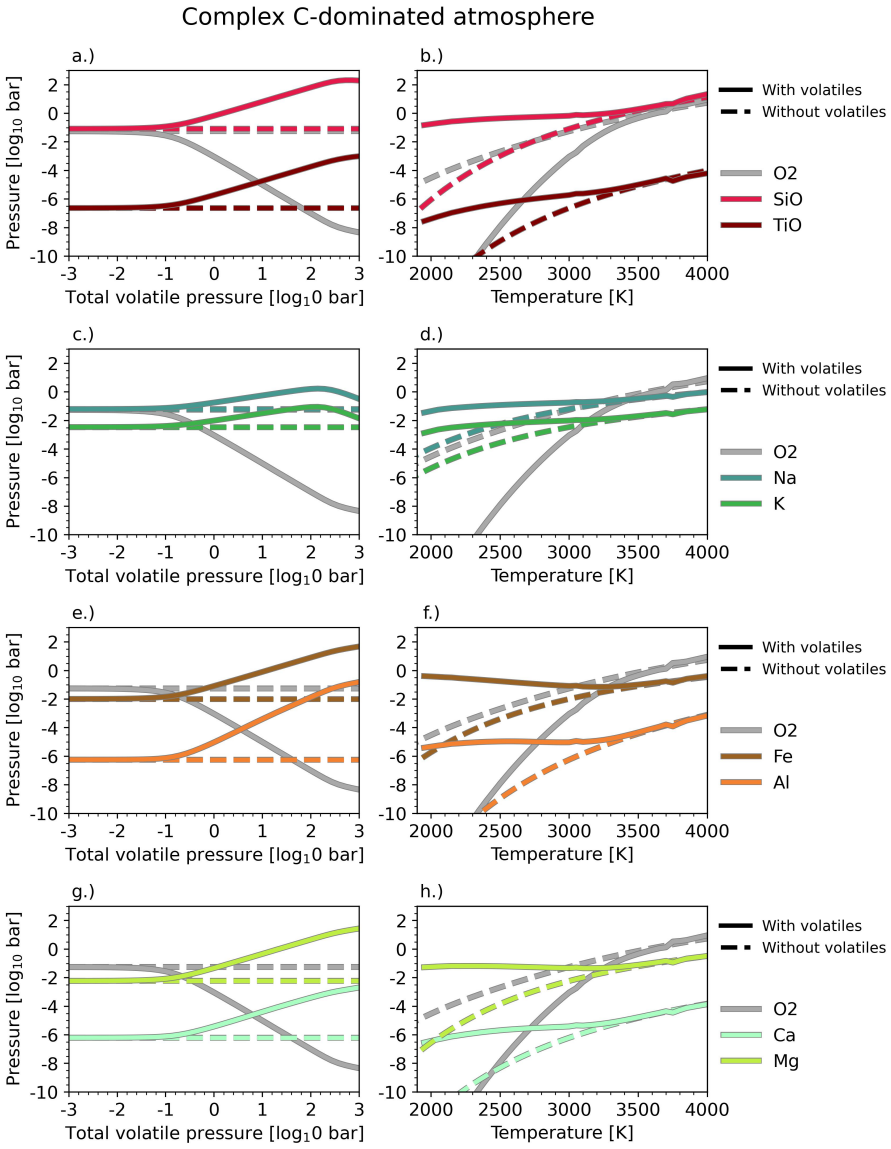


Figure 4.13: Effect of a complex C-dominated atmosphere on a selection of vaporised species: The partial pressures of the selected vaporised species (O_2, SiO, TiO, Fe, Na, and K) in a complex (including C, H, N, and S) C-dominated volatile atmosphere are shown using solid lines, while the dashed lines are used to indicate their partial pressures in volatile free atmospheres. The left panel (a) shows the partial pressures as a function of total volatile pressure at a fixed surface temperature of 3000 K. The right panel (b) shows the partial pressures as a function of surface temperature at a fixed total volatile pressure of 1 bar.

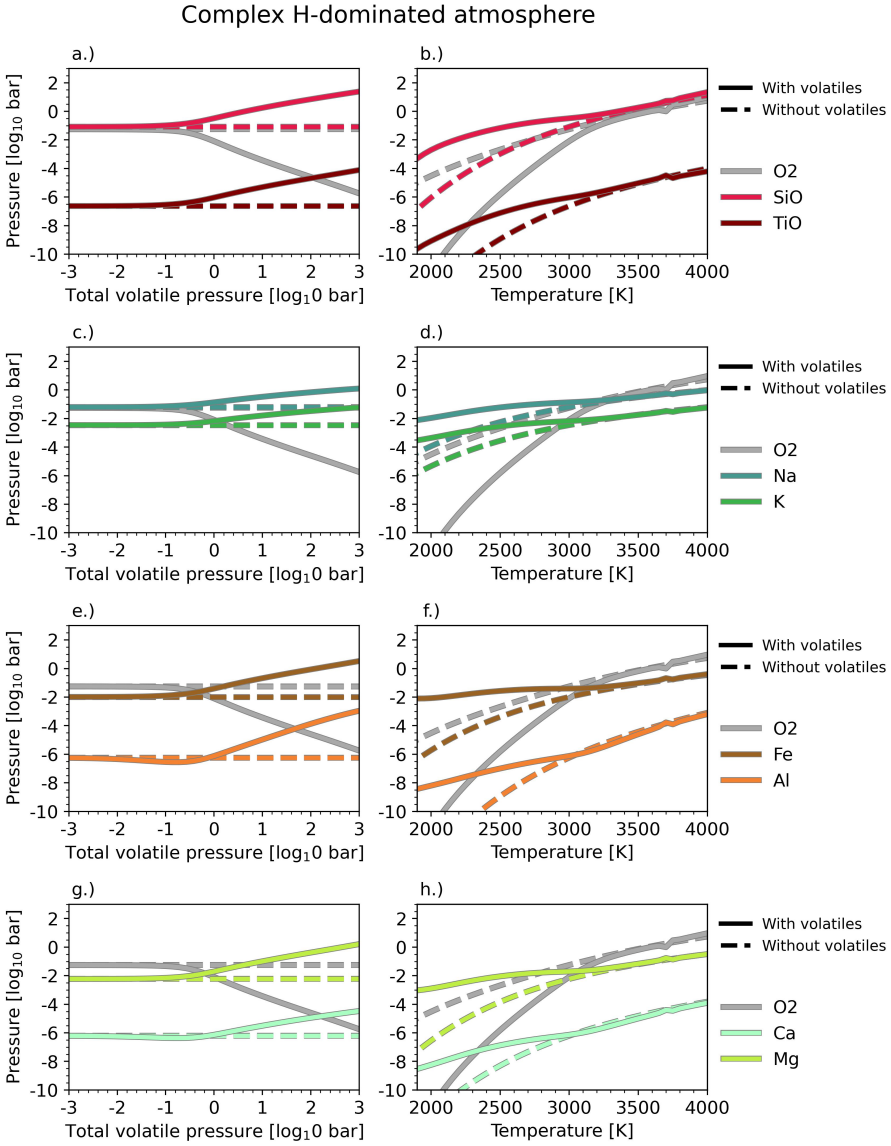


Figure 4.14: Effect of a complex H-dominated atmosphere on a selection of vaporised species: The partial pressures of the selected vaporised species (O_2, SiO, TiO, Fe, Na, and K) in a complex (including C, H, N, and S) H-dominated volatile atmosphere are shown using solid lines, while the dashed lines are used to indicate their partial pressures in volatile free atmospheres. The left panel (a) shows the partial pressures as a function of total volatile pressure at a fixed surface temperature of 3000 K. The right panel (b) shows the partial pressures as a function of surface temperature at a fixed total volatile pressure of 1 bar.

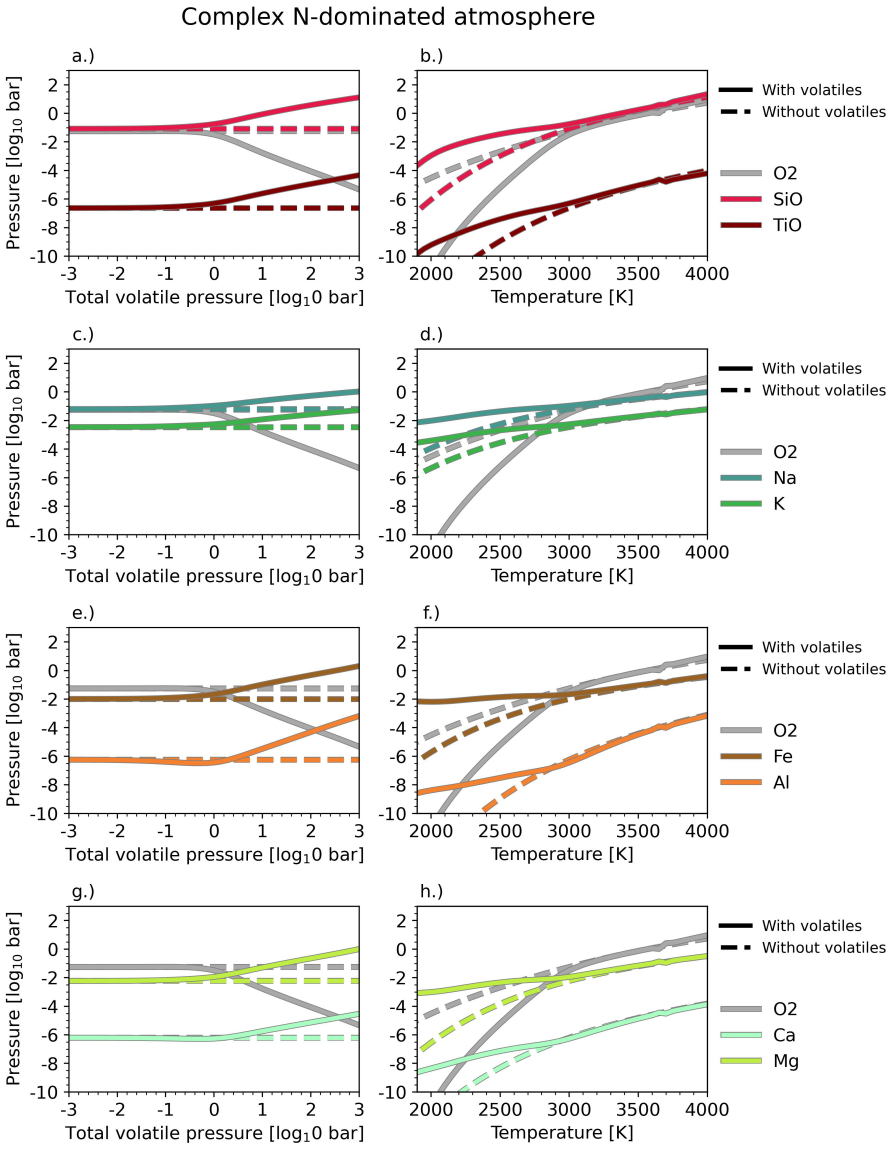


Figure 4.15: Effect of a complex N-dominated atmosphere on a selection of vaporised species: The partial pressures of the selected vaporised species (O_2, SiO, TiO, Fe, Na, and K) in a complex (including C, H, N, and S) N-dominated volatile atmosphere are shown using solid lines, while the dashed lines are used to indicate their partial pressures in volatile free atmospheres. The left panel (a) shows the partial pressures as a function of total volatile pressure at a fixed surface temperature of 3000 K. The right panel (b) shows the partial pressures as a function of surface temperature at a fixed total volatile pressure of 1 bar.

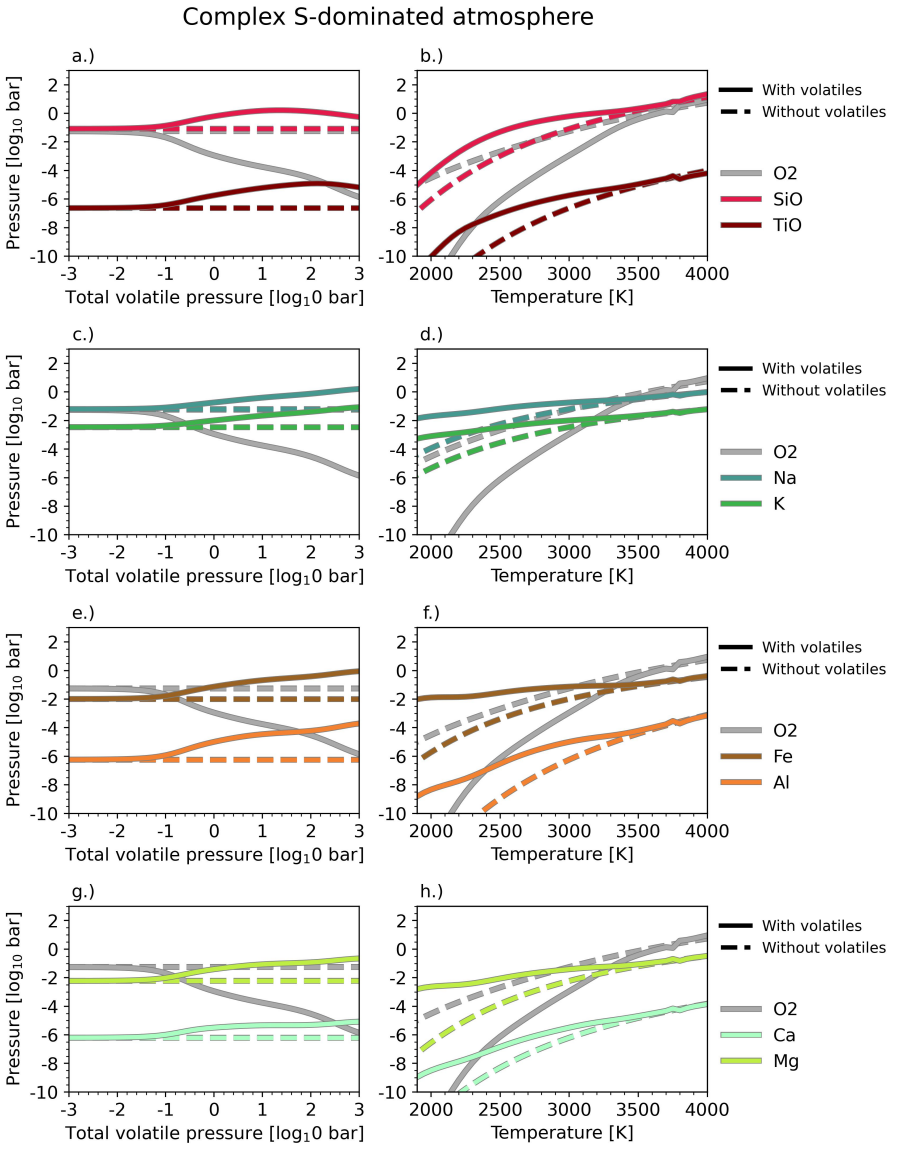


Figure 4.16: Effect of a complex S-dominated atmosphere on a selection of vaporised species: The partial pressures of the selected vaporised species (O_2, SiO, TiO, Fe, Na, and K) in a complex (including C, H, N, and S) S-dominated volatile atmosphere are shown using solid lines, while the dashed lines are used to indicate their partial pressures in volatile free atmospheres. The left panel (*a*) shows the partial pressures as a function of total volatile pressure at a fixed surface temperature of 3000 K. The right panel (*b*) shows the partial pressures as a function of surface temperature at a fixed total volatile pressure of 1 bar.

5 The effect of H^- continuum on Lava Planet Emission Spectra

Work in preparation **C.P.A. van Buchem**, M. Zilinskas, L. J. Janssen, Y. Miguel, and W. van Westrenen

Abstract

Hot rocky exoplanets (HREs) have the potential to reveal their interior makeup through studies of their atmospheric compositions thanks to surface lava oceans creating a direct interface between their interior and exterior reservoirs. Recent observations and modelling efforts point suggest that HREs may be able to support volatile bearing atmospheres. The extent to which volatile species can overwhelm lava composition specific signals in atmospheric spectra in such systems is as of yet not fully understood.

We aim to model volatile bearing HRE atmospheres and to understand how the presence of volatiles affects thermal emission spectra of these planets. The presence of free-electrons, due to the abundance of vaporised and subsequently ionized (alkali) metals, in a hot hydrogen-bearing atmosphere, suggests that H^- continuum opacity likely plays an important role in HRE atmospheres. It is already well established that the H^- continuum is highly influential in the atmospheres of stars and hot gas-giants, in this work we asses its impact on the atmospheres of HREs.

We make use of a self-consistent 1D forward model to estimate atmospheric chemical abundances, temperature-pressure structures, and thermal emission spectra, including feedback from the molten surface on the atmosphere.

We find that HREs with surface temperatures $\gtrsim$2500 K, even at a hydrogen volume mixing ratio of 10^{-5} in a 0.1 bar atmosphere, can lead to H^- continuum opacity dominating the features of the emission spectrum. As a result, spectral features of abundant atmospheric species (e.g. H_2O and SiO) are suppressed, and the planet's overall emission increases. This occurs because H^- opacity raises the photosphere to higher altitudes (with respect to atmospheres without H^- continuum absorption), where the temperature is higher in thermally inverted HRE atmospheres.

A strong H^- continuum could make it difficult to characterize the atmospheric composition of HREs due to the lack of/weakened strength of specific spectral features. However, due to the fact that abundant free-electrons are required for strong H^- opacity and that their main source is from ionized metals, the detection of a strong H^- continuum could be a potential indication of the presence of a surface lava ocean.

5.1 Introduction

Observations of hot rocky exoplanets (HREs) may have the potential to enable the inference of their interior compositions based on their atmospheric composition. Due to their short orbits, these planets have surface temperatures that can reach well above the eutectic melting point of silicate rocks ($\gtrsim$ 1500 K) making the existence of surface lava oceans very likely. Lava oceans could act as direct interfaces between the interiors and atmospheres of these planets (Léger et al. 2009; Henning et al. 2018; Boukaré et al. 2022). Understanding how the composition of a surface lava ocean influences the atmospheric composition of an HRE under varying temperatures, pressures, and volatile abundances, and quantifying the effect that this has on emission spectra is key to unlocking these windows into rocky planet interiors.

The modelling of lava oceans on HREs has historically been done under the simplifying assumption that no volatile elements (such as H, C, N, S, and P) are present in either the atmosphere or the interior of these planets (Schaefer & Fegley Jr. 2004; Miguel et al. 2011; Ito et al. 2015; Kite et al. 2016; Nguyen et al. 2020; Zilinskas et al. 2022; van Buchem et al. 2023; Wolf et al. 2023; Seidler et al. 2024). In recent years, an increasing number of both theoretical and observational studies have shown that it is plausible for HREs to contain volatile species. For example, magma oceans may potentially harbour large reservoirs of water (Hirschmann 2012; Lebrun et al. 2013; Dorn & Lichtenberg 2021; Kite & Schaefer 2021) and JWST observations of 55-Cnc e hint at the possible presence of a significant volatile atmosphere (Hu et al. 2024).

As such, the forward modelling of HRE atmospheres and their emission spectra has started to include volatile elements (Miguel 2018; Zilinskas et al. 2020, 2021). Piette et al. (2023) and Zilinskas et al. (2023) have shown that atmospheres that are a combination of vapor from a 'dry' (volatile-free) lava ocean and volatile atmospheric species (e.g. H_2O, CO, CO_2) may provide limited opportunities for observing lava ocean signatures in the infrared. Charnoz et al. (2023) and van Buchem et al. (2024) have shown that including volatile species in the lava ocean vaporisation reactions can lead to an increase in the abundance of all vapour elements. Falco et al. (2024) have studied the effect of lava vaporisation into an H atmosphere on emission spectra of HREs, finding that the existence of a thermal inversion may not a-priori exclude the presence of H in the atmosphere. In this work, we make use of LavAtmos 2.0 (van Buchem et al. 2024), which is able to take into account the effect of volatile elements (C, H, N, S, and P) to specifically investigate the effect of the HH^- continuum on HRE spectra.

The H^- continuum was first discovered to be of importance in the context of stellar atmospheres (e.g. Wildt 1939; Chandrasekhar 1945; John 1989) and has also been shown to be an important source of opacity in hot-Jupiters (Arcangeli et al. 2018; Lothringer et al. 2018; Parmentier et al. 2018). For H^- absorption to take place, the presence of both H and free-electrons is required. In previous

work where volatile-free atmospheres were assumed (Schaefer & Fegley 2009; Miguel et al. 2011; Kite et al. 2016; Zilinskas et al. 2022), no H was present, and in colder rocky-planet atmospheres containing volatiles, the concentration of free-electrons is not significant enough. HREs, however, have now been shown to potentially contain both H in their atmospheres and an abundance of free-electrons thanks to the presence of (alkali) metals vaporising from their surface lava oceans at high temperatures. Hence, H^- continuum absorption may potentially be of great importance to obtain a proper interpretation of HRE atmospheric emission spectra.

In this work, we use a self-consistent 1D modelling framework to show that even at low abundances H in HRE atmospheres can lead to significant H^- absorption across a range of equilibrium temperatures. We investigate the range of parameters within which this is the case and assess the effects this could have on the interpretation of HRE emission spectra.

5.2 Methods

5.2.1 Forward model

The forward model we use for this work is similar to that used in Zilinskas et al. (2022) and Zilinskas et al. (2023), but has been updated with the most recent versions of the component codes, as described in Zilinskas et al. (in rev) and Van Buchem et al. (in rev).

The model starts with calculating the melt-vapour composition for given melt-oxide (SiO_2, MgO, Al_2O_3, TiO_2, FeO, CaO, Na_2O, and K_2O) weight percentages and total atmospheric volatile element abundances (H, C, N, S, and P) . This is done using LavAtmos 2 (van Buchem et al. 2024), a vaporisation code that allows for volatile element abundances to be included in vaporisation calculations self-consistently. LavAtmos 2 makes use of the geothermodynamic code MELTS (Ghiorso & Sack 1995; Asimow & Ghiorso 1998; Ghiorso et al. 2002; Gualda et al. 2012; Ghiorso & Gualda 2015) to calculate the activities of melt species. The chemical-equilibrium constants used in the vaporisation reactions were calculated using data from the JANAF-NIST database (Chase 1998). In this study we assume the composition of the melts is equal to the composition of the Bulk Silicate Earth (BSE) (Palme & O'Neill 2003). We tested a range of different atmospheric volatile element abundances, each representing end-member compositions observed in our Solar System (see Table **??**).

The output from the vaporisation code is passed on to the atmospheric thermochemical equilibrium code FastChem 3 (Stock et al. 2018, 2022; Kitzmann et al. 2024) to calculate chemical compositions across a wide temperature-pressure (TP) grid. These abundances are then used by HELIOS (Malik et al. 2017, 2019; Whittaker et al. 2022) to calculate a TP profile. If the temperature at the bottom of the atmosphere, as determined by the TP profile, does not

coincide with the initial guess of the surface temperature, the code reiterates using the the temperature at the bottom of the TP profile as a new starting point. This is repeated until the difference between the initial temperature used for the vaporisation calculations differs by less than 25 K with the surface temperature derived from the TP profile.

The heat redistribution is parametrised using an f-factor (Hansen 2008) approximation based on the longwave optical depth of the atmosphere (Koll 2022) as included in HELIOS. We used a standard diatomic adiabatic coefficient $\kappa = 2/7$ for convective adjustment.

Once the model converges on a surface temperature, FastChem 3 is used again to calculate the chemical abundances along the finalized TP profile. The final temperature and chemical structure of the atmosphere are passed on to petitRADTRANS (Mollière et al. 2019, 2020) which produces an emission spectrum between 0.3 and 28 μm.

The opacities used in this work, in both HELIOS and petitRADRANS, are the same as those used for Zilinskas et al. (in rev.). A complete list is given in the appendix (Table 5.2)[1]. These opacities were either taken from the DACE[2] database or calculated using HELIOS-K (Grimm & Heng 2015; Grimm et al. 2021). Due to the H^- opacity being the focus of this paper, we discuss it in detail in the following subsection.

We used star-planet system parameters resembling those of 55-Cnc e as an illustrative example to demonstrate the overall influence of H^- on HRE atmospheres. This work does not aim to explain 55-Cnc e specifically. We use a planet radius of 1.946 $R_\oplus$, a planet surface gravity of 2222 cm s^{-2}, a stellar radius of 0.98 $R_\odot$, a stellar temperature of 5214 K, and a metallicity of 0.35. For the spectrum of the star we use the same spectrum that was used for 55-Cnc in Hu et al. (2024). This spectrum combines the near-infrared and infrared spectra of 55-Cnc as gathered during the observations presented in Hu et al. (2024) along with an interpolation of a `PHOENIX` model (Husser et al. 2013), and the spectrum from Crossfield (2012) for the shorter wavelengths.

5.2.2 H^- opacity

H^- has been known as the dominant source of continuum opacity in stellar atmospheres since first pointed out by Wildt (1939). The two mechanisms through which H^- absorbs are bound-free (*bf*) absorption and free-free (*ff*) absorption.

Bound-free absorption (also known as photo-detachment) takes place when a photon collides with an H^- ion and the photon carries enough energy to free the extra electron from the H^- ion, producing a free electron and a neutral H

[1] ExoMol (`https://www.exomol.com/`) was used as the main source for line list recommendations.

[2] https://dace.unige.ch/

Table 5.1: Volatile element compositions in mole fractions of the total volatile pressure in the atmosphere

	H	C	N	S	P
Solar	9.996E-01	2.691E-04	6.758E-05	1.318E-05	2.569E-07
Earth	5.126E-03	2.600E-04	9.946E-01	0.000E+00	0.000E+00
Titan	2.824E-02	6.627E-03	9.334E-01	0.000E+00	0.000E+00
Venus	3.900E-05	9.320E-01	6.784E-02	1.470E-04	0.000E+00

Notes. These composition are not including the species vaporised from the lava ocean. Solar composition was derived from Asplund et al. (2009). The Earth, Titan, and Venus atmospheric compositions were taken from Morley et al. (2017).

atom:

$$H^- + \gamma \rightarrow H + e^- \tag{5.1}$$

Where γ is a photon and e^- a free electron. The binding energy of an electron with an H atom is 0.7542 eV (Frolov 2015) and as such, this absorption method only impacts photons with a wavelength ≤ 1.644 μm.

Free-free absorption occurs when a photon is absorbed by an electron accelerating in the field of a neutral hydrogen atom (John 1991), as given in the reaction:

$$H + e^- + \gamma \rightarrow H + e^- \tag{5.2}$$

This type of absorption can take place at any given photon energy and is therefore not limited to specific wavelengths. However, its opacity does increase with wavelength and becomes significant (for this work) from the near infrared onwards. Unlike *bf* absorption, which is dependent on H^- abundance, *ff* absorption is dependent on the abundance of neutral H and free-electrons (e-).

The different regimes in which these types of absorption are dominant are shown in Figure 5.1. The models used in this figure are those of John (1988), and are also used in the radiative transfer codes to calculate the planetary emission spectra (HELIOS and petitRADTRANS, see Section **??**). These models are in good agreement with other commonly used parametrisations provided by Gray (2022) based on data gathered by Wishart (1979) and Bell & Berrington (1987) for *bf* and *ff* absorption respectively.

5.3 Results

The emission spectra of HREs can change significantly depending on their atmospheric composition. This is illustrated in Figure 5.2, where we compare the emission spectra (panel *a*) and TP profiles (panel *b*) of three atmosphere types. In blue, we show a pure (no lava vapour) 0.1 bar volatile atmosphere of

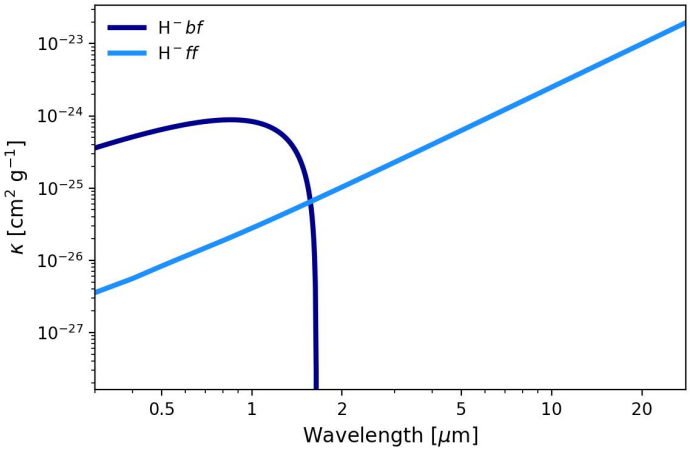


Figure 5.1: H- *bf* and *ff* opacities: Plotted using the models from John (1988) at 3000 K, 1e-4 bar, and assuming H-, H, and e- volume mixing ratios (VMRs) of $\simeq$ 2.21e-8, 4.48e-1, and 5.79e-2 respectively. These values are representative for what we find in a 0.1 bar atmosphere, at 0.016 AU, for a BSE composition melt (see section **??**).

solar-like composition (see Table 5.1)[3], in red a pure lava vapour atmosphere (no volatiles), and in orange a 'hybrid' atmosphere containing both 0.1 bar of volatile elements and lava vapour. All other system parameters used for these models are the same (as specified in section 5.2).

The volatile-only atmosphere has a non-inverted TP profile and has a spectrum dominated by H_2O absorption features in the near- and far-infrared. This is in contrast with the vapour only atmosphere, which has a fully inverted TP profile. This is due to the presence of strong optical absorbers, such as TiO, causing the atmosphere to be more opaque in the optical than in the infrared (Gandhi & Madhusudhan 2019), and is a common feature of HRE atmospheres (Zilinskas et al. 2022; Seidler et al. 2024). The vapour only spectrum also has clear spectral features of atomic Na and K in the optical and SiO in the infrared (around 9 μm). The 'hybrid' atmosphere, containing both volatile species and lava vapour, contrasts starkly with the other two. Emission is greater, and the emission spectrum is dominated by a continuum, lacking strong features of atmospheric species. The TP profile of this atmosphere bears some resemblance to the lava-vapour case, except with a non-inverted almost isothermal lower atmosphere (pressures above 1e-3 bar). To understand why the emission spectrum from the hybrid atmosphere looks so different, we have to look at its chemical structure and contribution to the opacity throughout the atmosphere.

[3]Due to the absence of a lava ocean determining the O abundance of the atmosphere, we used a solar O abundance.

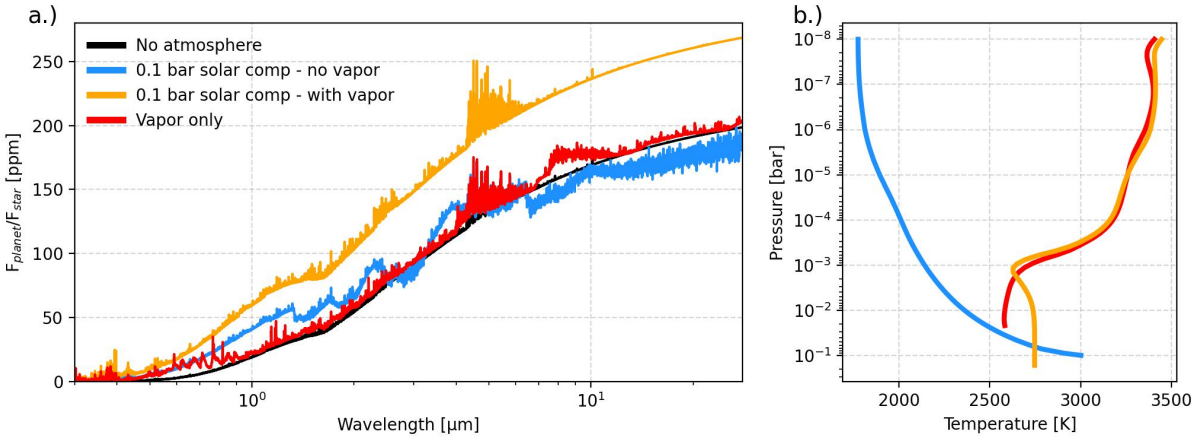


Figure 5.2: Comparing atmosphere types: Emission spectra (panel *a*) and TP profiles (panel *b*) of three different atmosphere types. A pure volatile atmosphere (of solar-like composition) is shown in blue, a pure volatile free (BSE) lava vapour atmosphere is shown in red, and the combination of a volatile with lava vapour atmosphere is shown in orange. As a point of reference we also plot the emission spectrum in the case of no atmosphere being present in black.

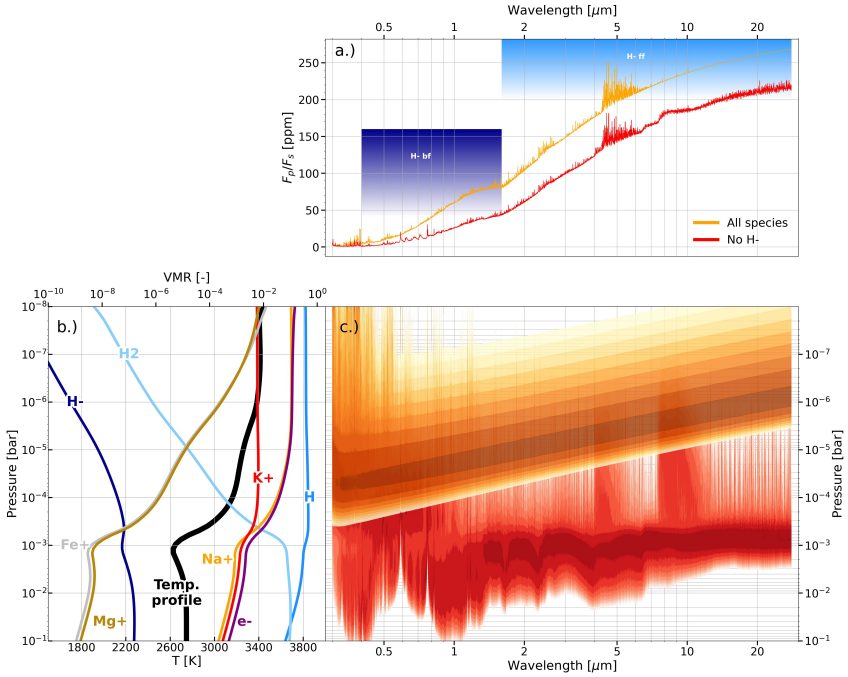


Figure 5.3: Overview of an atmosphere containing both lava vapor and volatile elements: The top panel (a) shows the spectrum of an HRE when including H^- continuum opacity in orange and the spectrum of the same atmosphere when H^- continuum opacity is ignored. The regions in which H^- bf and ff absorption dominate are indicated in dark blue and light blue respectively. The bottom left panel (b) shows the VMR of relevant species in the atmosphere, along with the TP profile. In the bottom right panel (c), the opacity contribution as a function of wavelength and pressure is shown for when H^- continuum opacity is (in orange) and is not (in red) included.

Figure 5.3 provides an overview of a number of properties of the 'hybrid' atmosphere. In the top panel (panel *a*), the full emission spectrum of the 'hybrid' atmosphere (shown in orange) is compared to the emission spectrum of the same atmosphere excluding H^- continuum opacities (shown in red). When H^- is excluded from the radiative transfer model used to produce the emission spectrum (see section 5.2.1), the resulting spectrum looks more similar to the vapor only model at a lower brightness, with K and Na lines visible in the optical and the SiO feature visible around 9 μm. The bottom right panel (panel *c*) explains the source of these differences. For the two spectra, the normalized opacity contribution is shown in the respective colors. When including the H^- continuum opacity the photosphere is located higher up in the atmosphere, from 1e-4 bar in the optical to 1d-6 bar in the infrared. When the H^- continuum opacity is excluded, the photosphere is located just below 1e-4 bar in the optical and around 1e-3 bar in the infrared. Due to the temperature-pressure profile being inverted (see panel *b* in the bottom left), the photosphere of the spectrum that includes H^- continuum opacity is emitting radiating from a region with a much higher temperature (around 3300 K) than the case without H^- continuum opacity (around 2600 K). As a result, the temperature brightness of the 'hybrid' spectrum is much higher than that of the other two models seen in Figure 5.2. We also see in this example how the H^- continuum opacity dominance does not allow for other spectral features to contribute significantly to the emission spectrum of the atmosphere.

Panel *b* includes the volume mixing ratio (VMR) of a number of relevant species. As discussed in section 5.2.2, H^- bf absorption is dependent on the abundance of H-, while H^- ff absorption is linked to the abundance of H and free electrons (e-). While H_2 dominates over H at the surface, as pressure decreases and (below 1e-3 bar) temperature increases, H_2 dissociates to form H. The abundance of e- is dependent on the abundance of ionized metals from which the e- have escaped through thermal dissociation. This is reflected in the strong correlation between the e- abundance and the abundance of the four major metal ions Na+, K+, Mg+, and Fe+. Below 1e-3 bar, K+ is the main source of free electrons with Na taking over beyond 1e-3 where the thermal inversion starts. From 1e-7 bar onward, Fe+ and Mg+ also start to contribute significantly to the e- abundance. The start of the photosphere of the 'hybrid' model at around 1e-5 bar, coincides with the e- abundance reaching a VMR of around 1e-1.

For H^-, its abundance follows the general trend of the TP profile at higher pressures and lower temperatures (in the case of this particular atmosphere), increasing with higher temperatures thanks to an increase in H and e-. However, as the temperature reaches beyond about 2800 K, the H^- abundance starts to decrease with increasing temperature. This is due to the thermal dissociation of H^- into H and e- (similarly to the formation of the positive metal ions).

In the following subsections we investigate the effects of varying atmospheric

H abundance, temperature, and volatile composition on the H^- continuum opacity.

5.3.1 Adding H to a lava planet atmosphere

To understand how much hydrogen must be present in the atmosphere for H^- continuum absorption to have a significant impact on the emission spectrum, we calculated the emission spectra of an HRE with a volatile atmosphere of varying total pressures (from 1e-8 up to 1e-1 bar) containing only H as volatile element. The results can be seen in Figure 5.4.

In panel *a* of Figure 5.4, the emission spectrum of the test planet in the case without an atmosphere is shown in black. The emission spectrum produced when including a pure lava vapour atmosphere is shown in yellow. Comparing with the no atmosphere case, we see that including a lava vapour atmosphere leads to the presence of emission features of K and Na in the optical and of SiO and SiO_2 in the infrared (around 9 μm). From this point onward, emission spectra are calculated for atmospheres containing an increasing amount of H in the atmosphere.

Adding just 1e-8 bar of total H pressure already leads to a shift in the spectrum, with a slight increase in emission at wavelengths beyond μm. With each increasing order of magnitude of added total elemental H abundance to the atmosphere, we see an increase in emission. This effect becomes more substantial towards longer wavelengths. At 1e-5 bar total H pressure the SiO and SiO_2 features around 9 μm are no longer discernible in the spectrum. At this H abundance, a significant increase in optical emission also starts taking place, which starts obscuring the alkali features. From 1e-4 bar total H pressure and upwards, the calculated emission spectra are entirely dominated by the H^- continuum. Increasing the total H abundance leads to a higher brightness temperature but no significant changes in the spectral features.

In panel *b* of Figure 5.4 the corresponding TP profiles of each of the models (except the no atmosphere case) are shown. The vapour only and low H abundance models all have very similar TP profiles and are superimposed on each other. From 1e-4 bar added H we start seeing a divergence in the lower atmosphere to higher pressures and higher temperatures. From 1e-3 bar onwards, moving up in the atmosphere to lower pressures, all TP profiles follow the same general trend. As we have seen in Figure 5.3, even when no H^- continuum opacity is included, the photosphere is located at around 1e-3 bar at its lowest point. As a result, the differences in TP structure that we are seeing deeper in the atmosphere do not affect the emission spectra. Hence, the differences that we are seeing in the spectra in panel *a* are due to the photosphere rising up to lower pressures and, due to the temperature inversion, higher temperatures leading to an increase in emission.

These models make it clear that only a small amount of H is required for H^- continuum opacity to affect the emission spectrum of HREs. In Figure 5.5

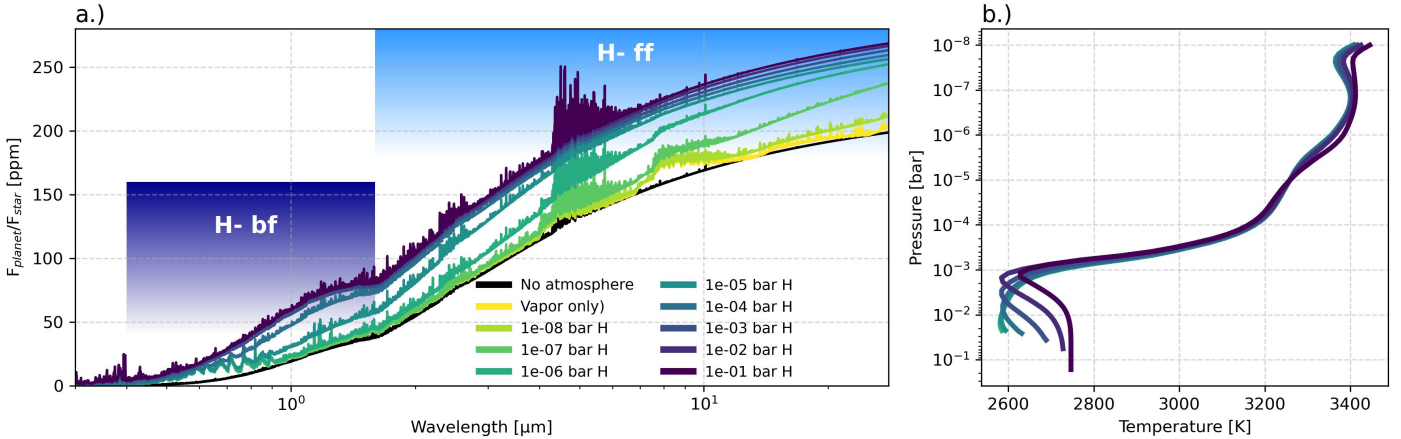


Figure 5.4: Adding H to a lava ocean atmosphere: The thermal emission spectra of our test planet plotted at varying total atmospheric H pressures are plotted in panel *a*. Note that this refers to the total H abundance. Panel *b* shows the corresponding TP profiles.

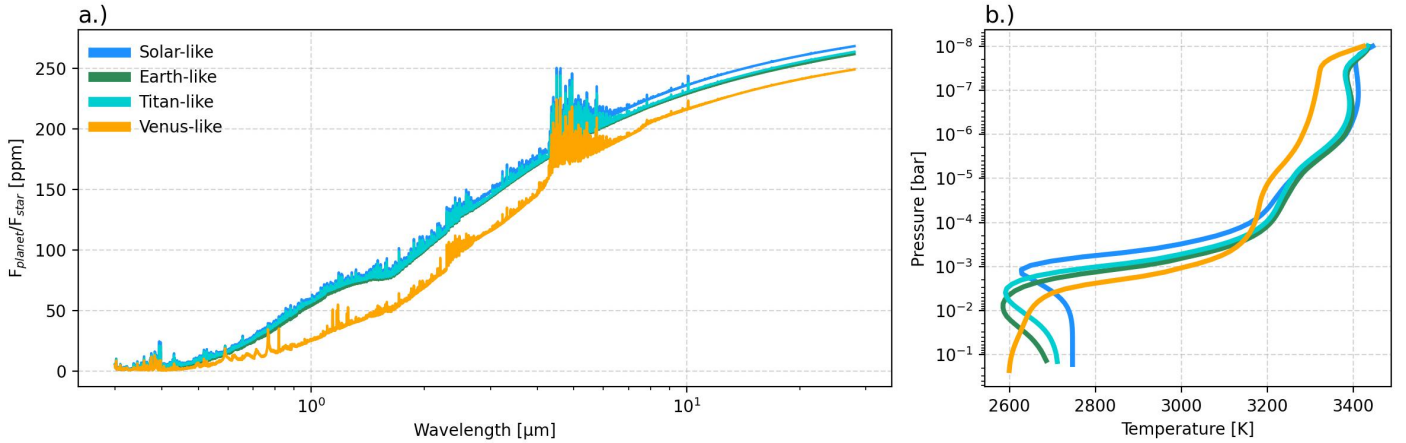


Figure 5.5: Emission spectra of complex volatile atmospheres: For each model a 0.1 bar of volatiles was assumed. The volatile compositions of each are given in Table 5.1.

we show that this is also the case for 'complex' volatile atmospheres, containing H, C, N, S, and P. In panel *a* the emission spectra of atmospheres with 0.1 bar volatiles are shown. Volatile abundances are based on a solar-like composition (Asplund et al. 2009), and Earth-like, Titan-like, and Venus-like compositions (Morley et al. 2017) (see Table 5.1). The corresponding TP profiles are shown in panel **b**.

The Solar-like, Earth-like, and Titan-like atmospheres (with H mole fractions of 9.996e-1, 5.126e-3, and 2.824e-2 respectively) are all significantly affected by the H^- minus continuum opacity - consistent with what we see in the pure H atmospheres in Figure 5.4. The Venus-like atmosphere has the least amount of H (mole fraction of 3.9e-5) and is therefore least affected by the H^- continuum opacity, but even so we see (most clearly in the far infrared beyond around 8 μm) that the spectrum is affected by the H^- ff opacity similarly to the 1e-6 bar pure H atmosphere in Figure 5.4 (which has a similar total H abundance).

From these models it is clear that an HRE requires very little H in its atmosphere for the emission spectrum to be dominated by H absorption. With as little as 1e-6 bar total H pressure obscuring vaporised lava features and 1e-4 bar total H being enough for the H^- continuum opacity to dominate the entire spectrum. However, as seen in Figure 5.2, more than just H is required in the atmosphere for H^- continuum opacity to affect the emission spectrum.

5.3.2 Sensitivity to temperature

As explained in section 5.2.2, free electrons are needed for atmospheric H^- continuum absorption to take place. They are necessary for H-*bf* absorption to form H^- ions and they are necessary for the H-*ff* absorption reaction to be able to take place (see equation 5.2). The main source of free electrons in HRE atmospheres is from (alkali) metals which enter the atmosphere through vaporisation from lava and are subsequently ionised at high temperatures. The most important of these ions for a melt of BSE composition (Palme & O'Neill 2003) are Na^+, K^+, Fe^+, and Mg^+. The (surface) temperature of the HRE dictates the amount and composition of vapour entering the atmosphere (van Buchem et al. 2023, 2024) and is a measure of the extent of thermal ionization taking place.

Furthermore, H-*bf* requires H atoms for H^- to be able to form and H-*ff* requires H atoms for the absorption reaction to take place. The formation of H over H_2 in an atmosphere is both pressure and temperature dependent, with higher temperatures favouring the formation of H. This adds another temperature dependence to the strength of H^- continuum opacity.

To assess how these temperature dependences affect the abundance of the relevant atmospheric species, the TP structure, and the resulting emission spectrum, we lowered the temperature of the test planet by varying the orbital distance from its host star from 0.016 AU to 0.032 AU. In Figure 5.6 we show how

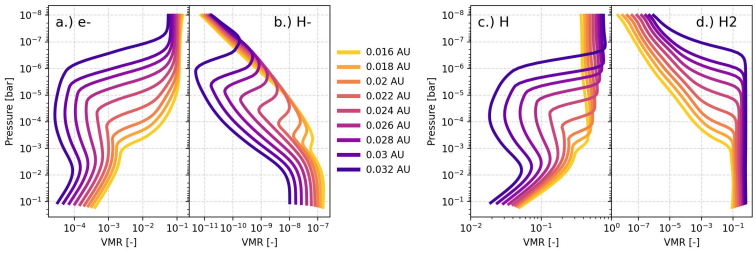


Figure 5.6: Abundance of atmospheric species at varying orbital distances: Shown for atmosphere with solar relative volatile abundances at a total volatile pressure of 0.1 bar and a BSE lava composition.

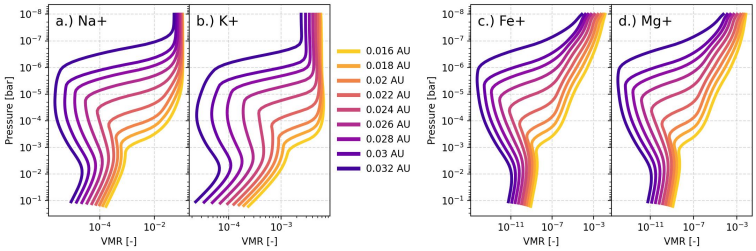


Figure 5.7: Abundances of metal ions at varying orbital distances: Shown for atmosphere with solar relative volatile abundances at a total volatile pressure of 0.1 bar and a BSE lava composition.

changing the orbital distance affects e-, H-, H, and H_2 abundances throughout the tested atmospheres. Figure 5.7 shows the same but for the key metal ion species (Na+, Mg+, Fe+, and Mg+). In Figure 5.8 we show the emission spectra and the TP profiles of these same models.

Comparing the e- abundances in panel *a* in Figure 5.6 and the metal ion abundances in Figure 5.7 with the TP profiles in panel *b* in Figure 5.8 clearly shows the positive relationship between temperature and atmospheric abundance of these species. In panels *c* and *d* the increase in H with temperature due to the dissociation of H_2 is illustrated.

Looking at panel *b* in Figure 5.6, we see that the H^- abundance has a positive relationship with temperature below about 2600 K. However, as temperatures reach beyond this point, the increase in thermal energy leads to the release of the captured electron, and H^- reverts to neutral H and a free electron. This explains the decrease in H^- abundance higher up in the atmospheres, even though we see an overall increase lower in the atmospheres where the temperatures are cooler.

The temperature dependences of the abundances of all the species required

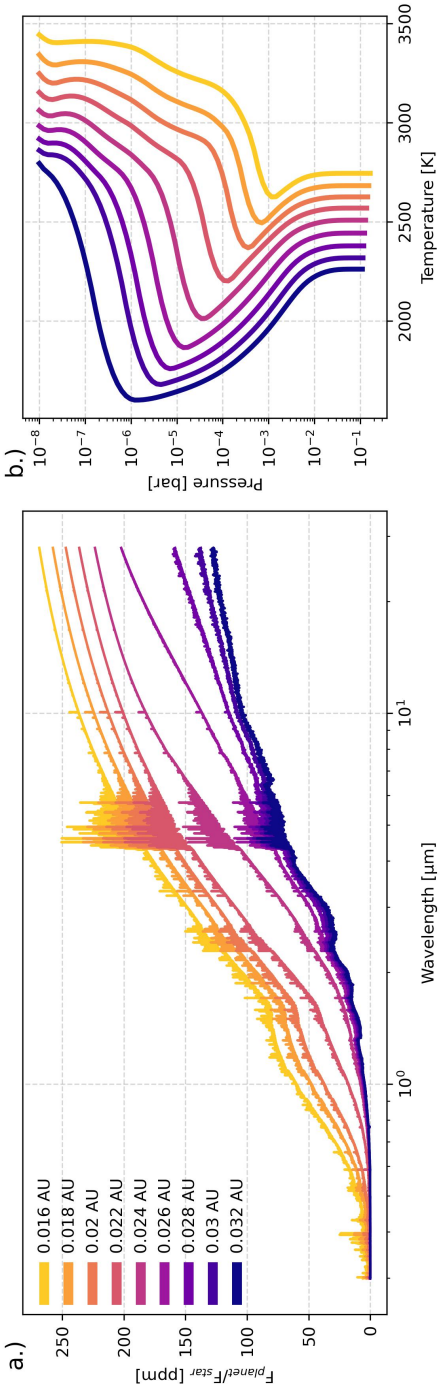


Figure 5.8: Emission spectra at varying orbital distances: Shown for atmospheres with solar relative volatile abundances at a total volatile pressure of 0.1 bar and a BSE lava composition.

for H^- continuum absorption causes emission spectra to vary strongly with temperature as well. Looking at panel *a* of Figure 5.8, we see that when the test planet is placed at a distance of 0.032 AU, surface temperature drops by 500 K, and at higher altitudes the drop is even greater (up to 1000 K with respect to the test planet at 0.016 AU). As a result the emission spectrum is far less bright, and it contains some visible spectral features. The drop in brightness of the emission spectrum is due to a combination of the photosphere being located at lower (and colder) altitudes due to a lack of H^- continuum opacity and a colder atmosphere overall. Without the H^- continuum dominating over other spectral features and colder atmospheric temperatures, we see some H_2O features in the optical wavelengths. There is also a hint of the SiO feature around 9 μm.

As the test planet orbital distance is lowered from 0.032 AU, our calculations indicate that at 0.026 AU (surface temperature of $\simeq$2400 K) there is a significant increase in emission in the infrared, obscuring any potential SiO features from a surface lava ocean. At 0.022 AU (surface temperature of $\simeq$2600 K) the H^- continuum also dominates over the optical lava ocean features - no spectral features are discernible anymore. Based on these models, which assume the presence of 0.1 bar of volatiles combined with vapour from a surface lava ocean, it appears that a rough temperature threshold from which point onwards the H^- continuum dominates the spectrum is when the majority of the atmosphere has a temperature greater than 2500 K.

5.4 Discussion

The dominance of the H^- continuum in HRE spectra at temperatures above approximately 2500 K in atmospheres containing hydrogen is such that it cannot be ignored when interpreting the spectra of these atmospheres.

The most significant change that we see in the emission spectra when including the H^- continuum is the large increase in flux emitted from the planet due to the photosphere moving up to higher altitudes and temperatures (see Figure 5.3). This can lead to a degeneracy in determining the surface temperature.

A potential way to overcome this degeneracy is by identifying distinct spectral features. As shown in Figure 5.2, both a vapour only and volatile only atmosphere have clear spectral features of the dominant species in their respective atmospheres. In an atmosphere dominated by the H^- continuum, none of these features are visible. The absence of spectral features in an H^- dominated spectrum will likely make it difficult to characterize the composition of these HREs.

However, as we have seen in sections 5.3.1 and 5.3.2, the opacity of the H^- continuum is heavily reliant on the presence of both H and free electrons in the atmosphere. Hence, if an emission spectrum is found to be dominated by the H^- continuum, this could be used in retrievals to place constraints on the H abundance of the atmosphere, and on the abundance of metal ions necessary

to produce the free-electrons. This has been shown to be of importance in studies on hot Jupiters, where including the H^- continuum in atmospheric retrievals has led to tighter constraints on the metallicity of the atmospheres of these planets (Arcangeli et al. 2018; Lothringer et al. 2018; Parmentier et al. 2018). In contrast with hot Jupiters, where metals may reach high up in the atmosphere through mixing with the interior, the dominant mechanism for metals to enter the atmosphere of an HRE would be through vaporisation of a surface lava ocean. Hence, strong H^- continuum emission could point to the presence of a surface lava ocean on an HRE.

5.5 Conclusion

We find that the H^- continuum from H-*bf* and H-*ff* absorption can dominate the emission spectrum of HREs. Even trace amounts of hydrogen in the atmosphere (as little as 10^{-6} total H partial pressure) can obscure the spectral features of other major atmospheric species. This also holds for planets with volatile but non-hydrogen dominated atmospheres - similar in composition to those of Earth, Titan, or Venus - may still experience significant effects from the H^- continuum in their emission spectra.

The presence of the H^- continuum leads to the photosphere of an HRE to move to higher altitudes than when no H^- continuum is included. As the atmospheres of HREs are generally inverted, this means that the photosphere is radiating from a region with a much greater temperature (around 500 K more) leading to a far brighter emission spectrum.

Due to the dependences of atmospheric H and free electron abundance on temperature, the impact of the H^- continuum is also heavily dependent on temperature. If the majority of an atmosphere has a temperature above approximately 2500 K, then we find that all other features are obstructed by the H^- continuum.

Due to the necessity of abundant free electrons in the atmosphere for H^- absorption to take place and the main source of free-electrons being ionized metals, finding a strong influence of the H^- continuum in an HRE atmosphere could be an indication of the existence of a surface lava ocean.

Acknowledgements

This work was supported financially through a Dutch Research Council (NWO) Planetary and Exoplanetary Science (PEPSci) grant awarded to Y.M. and W. van W.

Y.M and M.Z. acknowledge funding from the European Research Council (ERC) under the European Union's Horizon 2020 research and innovation programme (grant agreement no. 101088557, N-GINE). Part of this research was carried out at the Jet Propulsion Laboratory, California Institute of Technology, under a contract with the National Aeronautics and Space Administration.

Appendix

5.A Opacities

Table 5.2: List of opacities and their sources used to calculate the temperature-pressure profiles and emission spectra in this work. Those with DACE as indicated source were taken directly from the DACE database (`https://dace.unige.ch/`). For the other species, the opacities were calculated using HELIOS-K (`https://github.com/exoclime/HELIOS-K`) (Grimm & Heng 2015; Grimm et al. 2021).

Species	Source	Line list	Line list reference
Al	DACE	VALD	Ryabchikova et al. (2015)
AlH	HELIOS-K	AlHambra	Yurchenko et al. (2018c)
AlO	HELIOS-K	ATP	Patrascu et al. (2015)
C	DACE	Kurucz	Kurucz (1992)
C_2	DACE	8states	Yurchenko et al. (2018b)
C_2H_2	DACE	aCeTY	Chubb et al. (2020)
C_2H_4	DACE	MaYTY	Mant et al. (2018)
Ca	DACE	VALD	Ryabchikova et al. (2015)
CaH	HELIOS-K	MoLLIST	Li et al. (2012); Bernath (2020)
CaO	HELIOS-K	VBATHY	Yurchenko et al. (2016)
CaOH	DACE	OYT6	Owens et al. (2022)
CH	DACE	MoLLIST	Masseron et al. (2014); Bernath (2020)
CH_3	DACE	AYYJ	Adam et al. (2019)
CH_4	DACE	YT34to10	Yurchenko et al. (2017)
CN	HELIOS-K	Trihybrid	Syme & McKemmish (2021)
CO	DACE	Li2015	Li et al. (2015)
CO_2	DACE	HITEMP & UCL-4000[c]	Rothman et al. (2010); Yurchenko et al. (2020)
CS	DACE	JnK	Paulose et al. (2015)
Fe	DACE	VALD	Ryabchikova et al. (2015)
FeH	DACE	MoLLIST	Dulick et al. (2003)
H_2^+	DACE	ADJSAAM	Amaral et al. (2019)
H_2CO	DACE	AYTY	Al-Refaie et al. (2015)
H_2O	DACE	POKAZATEL	Polyansky et al. (2018)
H_2O_2	DACE	APTY	Al-Refaie et al. (2016)
H_2S	DACE	AYT2	Azzam et al. (2016)
H_3O^+	DACE	eXeL	Yurchenko et al. (2020)
HCN	HELIOS-K	Harris	Barber et al. (2014)
HNO_3	DACE	AIJS	Pavlyuchko et al. (2015)
HS	HELIOS-K	GYT	Gorman et al. (2019)
K	DACE	VALD	Ryabchikova et al. (2015)
KOH	DACE	OYT4	Owens et al. (2021)
Mg	DACE	Kurucz	Kurucz (1992)
MgH	HELIOS-K	MoLLIST	GharibNezhad et al. (2013); Bernath (2020)
MgO	HELIOS-K	LiTY	Li et al. (2019)
N	DACE	VALD	Ryabchikova et al. (2015)
N_2	DACE	WCCRMT	Western et al. (2018)
N_2O	DACE	HITEMP2019	Hargreaves et al. (2019)
Na	DACE	VALD	Ryabchikova et al. (2015)
NaH	HELIOS-K	Rivlin	Rivlin et al. (2015)
NaO	DACE	NaOUCMe	Mitev et al. (2022)
NaOH	DACE	OYT5	Owens et al. (2021)
NH	DACE	MoLLIST	Fernando et al. (2018)
NH_3	DACE	CoYuTe	Coles et al. (2019)
NO	DACE	XABC	Wong et al. (2017); Qu et al. (2021)
NO_2	DACE	HITEMP2019	Hargreaves et al. (2019)
NS	DACE	SNaSH	Yurchenko et al. (2018a)
OH	DACE	HITEMP	Rothman et al. (2010)
OH^+	DACE	MoLLIST	Hodges & Bernath (2017)

P	DACE	VALD	Ryabchikova et al. (2015)
PC	DACE	MoLLIST	Ram et al. (2014); Qin et al. (2021)
PH	HELIOS-K	LaTY	Langleben et al. (2019)
PH_3	DACE	SAlTY	Sousa-Silva et al. (2015)
PN	DACE	YYLT	Yorke et al. (2014)
PO	DACE	POPS	Prajapat et al. (2017)
PS	HELIOS-K	POPS	Prajapat et al. (2017)
S	DACE	VALD	Ryabchikova et al. (2015)
Si	DACE	VALD	Ryabchikova et al. (2015)
SiH	HELIOS-K	Slightly	Yurchenko et al. (2018c)
SiH_2	HELIOS-K	CATS	Clark et al. (2020)
SiH_4	DACE	OY2T	Owens et al. (2017)
SiN	DACE	SiNfull	Semenov et al. (2022)
SiO	HELIOS-K	SiOUVenIR	Yurchenko et al. (2022)
SiO_2	DACE	OYT3	Owens et al. (2020)
SiS	DACE	UCTY	Upadhyay et al. (2018)
SO	DACE	SOLIS	Brady et al. (2024)
SO_2	ExoMol	ExoAmes	Underwood et al. (2016a)
SO_3	ExoMol	UYT2	Underwood et al. (2016b)
Ti	DACE	VALD	Ryabchikova et al. (2015)
TiH	HELIOS-K	MoLLIST	Burrows et al. (2005); Bernath (2020)
TiO	HELIOS-K	Toto	McKemmish et al. (2019)

Scattering and continuum

CO, CO_2, H		Scattering	
H_2, N_2, O_2		Scattering	
H^-		Continuum (bf & ff)	John (1988)
H_2-H_2	petitRADTRANS	CIA	Borysow et al. (2001); Borysow (2002)
CO_2-CO_2	petitRADTRANS	CIA	Karman et al. (2019)
O_2-O_2	petitRADTRANS	CIA	Karman et al. (2019)
N_2-H_2	petitRADTRANS	CIA	Karman et al. (2019)
N_2-N_2	petitRADTRANS	CIA	Karman et al. (2019)

Bibliography

Adam A. Y., Yachmenev A., Yurchenko S. N., Jensen P., 2019, Journal of Physical Chemistry A, 123, 4755

Al-Refaie A. F., Yachmenev A., Tennyson J., Yurchenko S. N., 2015, \mnras, 448, 1704

Al-Refaie A. F., Polyansky O. L., Ovsyannikov R. I., Tennyson J., Yurchenko S. N., 2016, \mnras, 461, 1012

Amaral P. H. R., Diniz L. G., Jones K. A., Stanke M., Alijah A., Adamowicz L., Mohallem J. R., 2019, \apj, 878, 95

Andrault D., Bolfan-Casanova N., Nigro G. L., Bouhifd M. A., Garbarino G., Mezouar M., 2011, Earth and Planetary Science Letters, 304, 251

Angelo I., Hu R., 2017, The Astronomical Journal, 154, 232

Arcangeli J., et al., 2018, The Astrophysical Journal, 855, L30

Aris R., 1969, Elementary Chemical Reactor Analysis. Prentice-Hall Inc., Englewood Cliffs, NJ

Armstrong D. J., Osborn H. P., Brown D. J. A., Faedi F., Gómez Maqueo Chew Y., Martin D. V., Pollacco D., Udry S., 2014, Monthly Notices of the Royal Astronomical Society, 444, 1873

Asimow P. D., Ghiorso M. S., 1998, American Mineralogist, 83, 1127

Asplund M., Grevesse N., Sauval A. J., Scott P., 2009, Annual Review of Astronomy and Astrophysics, 47, 481

Azzam A. A. A., Tennyson J., Yurchenko S. N., Naumenko O. V., 2016, \mnras, 460, 4063

Barber R. J., Strange J. K., Hill C., Polyansky O. L., Mellau G. C., Yurchenko S. N., Tennyson J., 2014, \mnras, 437, 1828

Barnes R., 2017, Celestial Mechanics and Dynamical Astronomy, 129, 509

Batalha N. E., et al., 2017, Publications of the Astronomical Society of the Pacific, 129, 064501

Bean J. L., Raymond S. N., Owen J. E., 2021, Journal of Geophysical Research: Planets, 126, e2020JE006639

Beatty T. G., Gaudi B. S., 2008, The Astrophysical Journal, 686, 1302

Bell K. L., Berrington K. A., 1987, Journal of Physics B: Atomic and Molecular Physics, 20, 801

Bell T. J., et al., 2023, A First Look at the JWST MIRI/LRS Phase Curve of WASP-43b, doi:10.48550/arXiv.2301.06350, http://arxiv.org/abs/2301.06350

Bell T. J., et al., 2024, Nature Astronomy, 8, 879

Bernath P. F., 2020, \jqsrt, 240, 106687

Blackman J. W., et al., 2021, Nature, 598, 272

Bond J. C., O'Brien D. P., Lauretta D. S., 2010, The Astrophysical Journal, 715, 1050

Bonsor A., Jofré P., Shorttle O., Rogers L. K., Xu() S., Melis C., 2021, Monthly Notices of the Royal Astronomical Society, 503, 1877

Borysow A., 2002, åp, 390, 779

Borysow A., Jorgensen U. G., Fu Y., 2001, \jqsrt, 68, 235
Boukaré C. E., Cowan N. B., Badro J., 2022, The Astrophysical Journal, 936, 148
Boukaré C. E., Lemasquerier D., Cowan N., Samuel H., Badro J., 2023, Lava planets interior dynamics govern the long-term evolution of their magma oceans, doi:10.48550/arXiv.2308.13614, http://arxiv.org/abs/2308.13614
Bower D. J., Hakim K., Sossi P. A., Sanan P., 2022, The Planetary Science Journal, 3, 93
Brady R. P., Yurchenko S. N., Tennyson J., Kim G.-S., 2024, \mnras, 527, 6675
Brinkman C., et al., 2022, TOI-561 b: A Low Density Ultra-Short Period "Rocky" Planet around a Metal-Poor Star, doi:10.48550/arXiv.2210.06665, http://arxiv.org/abs/2210.06665
Brugman K., Phillips M. G., Till C. B., 2021, Journal of Geophysical Research: Planets, 126, e2020JE006731
Bryson S., et al., 2021, The Astronomical Journal, 161, 36
Burrows A., Dulick M., Bauschlicher C. W. J., Bernath P. F., Ram R. S., Sharp C. M., Milsom J. A., 2005, \apj, 624, 988
Busetti F., Beust H., Harley C., 2018, Astronomy & Astrophysics, 619, A91
Carter-Bond J. C., O\textquotesingleBrien D. P., Mena E. D., Israelian G., Santos N. C., Hernández J. I. G., 2012, The Astrophysical Journal, 747, L2
Chandrasekhar S., 1945, The Astrophysical Journal, 102, 223
Charnoz S., Falco A., Tremblin P., Sossi P., Caracas R., Lagage P.-O., 2023, Astronomy & Astrophysics, 674, A224
Charpinet S., et al., 2011, Nature, 480, 496
Chase M. W., 1998, NIST-JANAF Thermochemical Tables, 4 edn. Vol. 1, American Chemical Society, http://adsabs.harvard.edu/pdf/1971LPSC...2.1367D
Chubb K. L., Min M., Kawashima Y., Helling C., Waldmann I., 2020, Astronomy & Astrophysics, 639, A3
Chubb K. L., et al., 2021, Astronomy & Astrophysics, 646, A21
Clark V. H. J., Owens A., Tennyson J., Yurchenko S. N., 2020, \jqsrt, 246, 106929
Cohen L. H., Ito K., Kennedy G. C., 1967, American Journal of Science, 265, 475
Coles P. A., Yurchenko S. N., Tennyson J., 2019, \mnras, 490, 4638
Crossfield I. J. M., 2012, Astronomy & Astrophysics, 545, A97
Dawson R. I., Johnson J. A., 2018, Annual Review of Astronomy and Astrophysics, 56, 175
Deibert E. K., Mooij E. J. W. d., Jayawardhana R., Ridden-Harper A., Sivanandam S., Karjalainen R., Karjalainen M., 2021, The Astronomical Journal, 161, 209
Demory B.-O., et al., 2011, Astronomy & Astrophysics, 533, A114

Demory B.-O., Gillon M., Madhusudhan N., Queloz D., 2016a, Monthly Notices of the Royal Astronomical Society, 455, 2018

Demory B.-O., et al., 2016b, Nature, 532, 207

Denbigh K., 1955, The Principles of Chemical Equilibrium, with Applications in Chemistry and Chemical Engineering.. Cambridge University Press, Cambridge, UK

Dixon J. E., Stolper E. M., John R. H., 1995, Journal of Petrology

Dorn C., Lichtenberg T., 2021, The Astrophysical Journal Letters, 922, L4

Dorn C., Khan A., Heng K., Connolly J. A. D., Alibert Y., Benz W., Tackley P., 2015, Astronomy & Astrophysics, 577, A83

Dorn C., Venturini J., Khan A., Heng K., Alibert Y., Helled R., Rivoldini A., Benz W., 2017, Astronomy & Astrophysics, Volume 597, id.A37, <NUMPAGES>16</NUMPAGES> pp., 597, A37

Dressing C. D., Charbonneau D., 2015, The Astrophysical Journal, 807, 45

Dulick M., Bauschlicher C. W. J., Burrows A., Sharp C. M., Ram R. S., Bernath P., 2003, \apj, 594, 651

Dyck B., Wade J., Palin R., 2021, The Astrophysical Journal Letters, 913, L10

Elkins-Tanton L. T., 2012, Annual Review of Earth and Planetary Sciences, 40, 113

Elkins-Tanton L. T., Burgess S., Yin Q.-Z., 2011, Earth and Planetary Science Letters, 304, 326

Espinoza N., et al., 2020, Monthly Notices of the Royal Astronomical Society, 491, 2982

Esteves L. J., Mooij E. J. W. d., Jayawardhana R., Watson C., Kok R. d., 2017, The Astronomical Journal, 153, 268

Falco A., Tremblin P., Charnoz S., Robert Ridgway J., Lagage P.-O., 2024, Astronomy & Astrophysics

Fedkin A., Grossman L., Ghiorso M., 2006, Geochimica et Cosmochimica Acta, 70, 206

Fegley B., Cameron A., 1987, Earth and Planetary Science Letters, 82, 207

Fegley B., Lodders K., Jacobson N. S., 2023, Geochemistry, 83, 125961

Fernando A. M., Bernath P. F., Hodges J. N., Masseron T., 2018, \jqsrt, 217, 29

Fortney J. J., Marley M. S., Lodders K., Saumon D., Freedman R., 2005, The Astrophysical Journal, 627, L69

France K., et al., 2016, The Astrophysical Journal, 820, 89

Frolov A. M., 2015, The European Physical Journal D, 69, 1

Gale A., Dalton C. A., Langmuir C. H., Su Y., Schilling J.-G., 2013, Geochemistry, Geophysics, Geosystems, 14, 489

Gandhi S., Madhusudhan N., 2019, Monthly Notices of the Royal Astronomical Society, 485, 5817

Gandhi S., et al., 2025, The ESO SupJup Survey V: Exploring Atmospheric Variability and Orbit of the Super-Jupiter AB Pictoris b with CRIRES+, doi:10.48550/arXiv.2501.05114, http://arxiv.org/abs/2501.05114

GharibNezhad E., Shayesteh A., Bernath P. F., 2013, \mnras, 432, 2043
Ghiorso M. S., Gualda G. A. R., 2015, Contributions to Mineralogy and Petrology, 169, 53
Ghiorso M. S., Sack R. O., 1995, Contributions to Mineralogy and Petrology, 119, 197
Ghiorso M. S., Hirschmann M. M., Reiners P. W., Kress V. C., 2002, Geochemistry, Geophysics, Geosystems, 3, 1
Gordon S., Mcbride B. J., 1994, Computer program for calculation of complex chemical equilibrium compositions and applications. Part 1: Analysis, https://ntrs.nasa.gov/citations/19950013764
Gorman M. N., Yurchenko S. N., Tennyson J., 2019, \mnras, 490, 1652
Gray D. F., 2008, The Observation and Analysis of Stellar Photospheres. https://ui.adsabs.harvard.edu/abs/2008oasp.book.....G
Gray D. F., 2022, The Observation and Analysis of Stellar Photospheres, 4 edn. Cambridge University Press
Greenwood R. C., Franchi I. A., Jambon A., Buchanan P. C., 2005, Nature, 435, 916
Grimm S. L., Heng K., 2015, The Astrophysical Journal, 808, 182
Grimm S. L., et al., 2021, The Astrophysical Journal Supplement Series, 253, 30
Gualda G. A. R., Ghiorso M. S., Lemons R. V., Carley T. L., 2012, Journal of Petrology, 53, 875
Guillot T., Fletcher L. N., Helled R., Ikoma M., Line M. R., Parmentier V., 2022, Giant Planets from the Inside-Out, doi:10.48550/arXiv.2205.04100, http://arxiv.org/abs/2205.04100
Guimond C. M., Wang H., Seidler F., Sossi P., Mahajan A., Shorttle O., 2024, From stars to diverse mantles, melts, crusts and atmospheres of rocky exoplanets, doi:10.48550/arXiv.2404.15427, http://arxiv.org/abs/2404.15427
Guzmán-Mesa A., Kitzmann D., Mordasini C., Heng K., 2022, Monthly Notices of the Royal Astronomical Society, 513, 4015
Hakim K., Spaargaren R., Grewal D. S., Rohrbach A., Berndt J., Dominik C., van Westrenen W., 2019a, Astrobiology, 19, 867
Hakim K., Berg A. v. d., Vazan A., Höning D., Westrenen W. v., Dominik C., 2019b, Astronomy & Astrophysics, 630, A152
Hans Wedepohl K., 1995, Geochimica et Cosmochimica Acta, 59, 1217
Hansen B. M. S., 2008, The Astrophysical Journal Supplement Series, 179, 484
Hargreaves R. J., et al., 2019, \jqsrt, 232, 35
Hastie J., Bonnell D. W., 1985, High Temp.Sci., 19, 275
Hastie J., Bonnell D., 1986, Journal of Non-Crystalline Solids, 84, 151
Hastie J. W., Horton W. S., Plante E. R., Bonneel D. W., 1982a, High Temperatures - High Pressures, 14, 669
Hastie J. W., Plante E. R., Bonnel D. W., 1982b, in ACS Symposium Series, Vol. 179, Metal Bonding and Interactions in High Temperature Sys-

tems. AMERICAN CHEMICAL SOCIETY, pp 543–600, doi:10.1021/bk-1982-0179.ch034, https://doi.org/10.1021/bk-1982-0179.ch034
Henning W. G., et al., 2018, arXiv:1804.05110 [astro-ph, physics:physics]
Herbort O., Woitke P., Helling C., Zerkle A., 2020, Astronomy & Astrophysics, 636, A71
Herbort O., Woitke P., Helling C., Zerkle A. L., 2022, Astronomy & Astrophysics, 658, A180
Hin R. C., et al., 2017, Nature, 549, 511
Hinkel N. R., Burger D., 2017, arXiv:1712.04944 [astro-ph]
Hinkel N. R., Unterborn C. T., 2018, The Astrophysical Journal, 853, 83
Hirschmann M. M., 2000, Geochemistry, Geophysics, Geosystems, 1, n/a
Hirschmann M. M., 2012, Earth and Planetary Science Letters, 341-344, 48
Hirschmann M., Baker M., Stolper E., 1998, Geochimica et Cosmochimica Acta, 62, 883
Hodges J. N., Bernath P. F., 2017, \apj, 840, 81
Hu R., Seager S., 2014, The Astrophysical Journal, 784, 63
Hu R., et al., 2024, Nature, pp 1–2
Husser T.-O., Berg S. W.-v., Dreizler S., Homeier D., Reiners A., Barman T., Hauschildt P. H., 2013, Astronomy & Astrophysics, 553, A6
Iezzi G., Vulcanologia I., Roma S., Roma 2008
Ito Y., Ikoma M., Kawahara H., Nagahara H., Kawashima Y., Nakamoto T., 2015, The Astrophysical Journal, 801, 144
Ito Y., Changeat Q., Edwards B., Al-Refaie A., Tinetti G., Ikoma M., 2021, Experimental Astronomy
John T. L., 1988, Astronomy and Astrophysics, 193, 189
John T. L., 1989, Monthly Notices of the Royal Astronomical Society, 240, 1
John T. L., 1991, Astronomy and Astrophysics, 244, 511
Jäggi N., et al., 2021, The Planetary Science Journal, 2, 230
Karman T., et al., 2019, ıcarus, 328, 160
Keles E., et al., 2022, Monthly Notices of the Royal Astronomical Society, 513, 1544
Kempton E. M.-R., et al., 2018, Publications of the Astronomical Society of the Pacific, 130, 114401
Kippenhahn R., Weigert A., Weiss A., 2012, Stellar Structure and Evolution, 2nd ed. 2012 edition edn. Springer, Berlin Heidelberg
Kite E. S., Schaefer L., 2021, The Astrophysical Journal Letters, 909, L22
Kite E. S., Fegley Jr. B., Schaefer L., Gaidos E., 2016, The Astrophysical Journal, 828, 80
Kite E. S., Fegley Jr. B., Schaefer L., Ford E., 2020, The Astrophysical Journal, 891, 111
Kitzmann D., Stock J. W., Patzer A. B. C., 2024, Monthly Notices of the Royal Astronomical Society, 527, 7263
Klein B., Jura M., Koester D., Zuckerman B., 2011, The Astrophysical Journal, 741, 64

Koll D. D. B., 2022, The Astrophysical Journal, 924, 134

Krieger F. J., 1965, Technical report, The Thermodynamics of the Alumina/Aluminum-Oxygen Vapor System, https://www.rand.org/pubs/research_memoranda/RM5042.html. The Rand Corporation, https://www.rand.org/pubs/research_memoranda/RM5042.html

Kurucz R. L., 1992, Revista Mexicana de Astronomia y Astrofisica, vol. 23, 23, 45

Lamoreaux R. H., Hildenbrand D. L., 1984, Journal of Physical and Chemical Reference Data, 13, 151

Lamoreaux R. H., Hildenbrand D. L., Brewer L., 1987, Journal of Physical and Chemical Reference Data, 16, 419

Langleben J., Tennyson J., Yurchenko S. N., Bernath P., 2019, \mnras, 488, 2332

Lebrun T., Massol H., Chassefière E., Davaille A., Marcq E., Sarda P., Leblanc F., Brandeis G., 2013, Journal of Geophysical Research: Planets, 118, 1155

Li G., Harrison J. J., Ram R. S., Western C. M., Bernath P. F., 2012, \jqsrt, 113, 67

Li G., Gordon I. E., Rothman L. S., Tan Y., Hu S.-M., Kassi S., Campargue A., Medvedev E. S., 2015, \apjs, 216, 15

Li H. Y., Tennyson J., Yurchenko S. N., 2019, Monthly Notices of the Royal Astronomical Society, 486, 2351

Lichtenberg T., 2021, The Astrophysical Journal Letters, 914, L4

Lichtenberg T., Miguel Y., 2024, Super-Earths and Earth-like Exoplanets, doi:10.48550/arXiv.2405.04057, http://arxiv.org/abs/2405.04057

Lichtenberg T., Bower D. J., Hammond M., Boukrouche R., Sanan P., Tsai S.-M., Pierrehumbert R. T., 2021, Journal of Geophysical Research: Planets, 126, e2020JE006711

Lin Y., Tronche E. J., Steenstra E. S., van Westrenen W., 2017, Nature Geoscience, 10, 14

Lin Y., van Westrenen W., Mao H.-K., 2021, Proceedings of the National Academy of Sciences, 118, e2110427118

Loftus K., Luo Y., Fan B., Kite E. S., 2024, Extreme Weather Variability on Hot Rocky Exoplanet 55 Cancri e Explained by Magma Temperature-Cloud Feedback, http://arxiv.org/abs/2409.16270

Lothringer J. D., Barman T., 2019, The Astrophysical Journal, 876, 69

Lothringer J. D., Barman T., Koskinen T., 2018, The Astrophysical Journal, 866, 27

Loyd R. O. P., et al., 2016, The Astrophysical Journal, 824, 102

Léger A., et al., 2009, Astronomy & Astrophysics, 506, 287

Malik M., et al., 2017, The Astronomical Journal, 153, 56

Malik M., Kempton E. M. R., Koll D. D. B., Mansfield M., Bean J. L., Kite E., 2019, The Astrophysical Journal, 886, 142

Manabe S., Strickler R. F., 1964, Journal of the Atmospheric Sciences, 21, 361

Mant B. P., Yachmenev A., Tennyson J., Yurchenko S. N., 2018, \mnras, 478, 3220

Masseron T., et al., 2014, åp, 571, A47

Maurice M., Dasgupta R., Hassanzadeh P., 2024, Astronomy & Astrophysics, 688, A47

Mayor M., Queloz D., 1995, Nature, 378, 355

McKemmish L. K., Masseron T., Hoeijmakers H. J., Pérez-Mesa V., Grimm S. L., Yurchenko S. N., Tennyson J., 2019, Monthly Notices of the Royal Astronomical Society, 488, 2836

Meier T. G., Bower D. J., Lichtenberg T., Hammond M., Tackley P. J., 2023, Interior dynamics of super-Earth 55 Cancri e, doi:10.48550/arXiv.2308.00592, http://arxiv.org/abs/2308.00592

Miguel Y., 2018, Monthly Notices of the Royal Astronomical Society

Miguel Y., Kaltenegger L., Fegley B., Schaefer L., 2011, The Astrophysical Journal, 742, L19

Mitev G. B., Taylor S., Tennyson J., Yurchenko S. N., Buchachenko A. A., Stolyarov A. V., 2022, \mnras, 511, 2349

Mollière P., Wardenier J. P., van Boekel R., Henning T., Molaverdikhani K., Snellen I. A. G., 2019, Astronomy & Astrophysics, 627, A67

Mollière P., et al., 2020, Astronomy & Astrophysics, 640, A131

Morbidelli A., Raymond S. N., 2016, Journal of Geophysical Research: Planets, 121, 1962

Morley C. V., Kreidberg L., Rustamkulov Z., Robinson T., Fortney J. J., 2017, The Astrophysical Journal, 850, 121

Morton T. D., Bryson S. T., Coughlin J. L., Rowe J. F., Ravichandran G., Petigura E. A., Haas M. R., Batalha N. M., 2016, The Astrophysical Journal, 822, 86

Moses J. I., et al., 2013, The Astrophysical Journal, 777, 34

Mullally S. E., et al., 2024, JWST Directly Images Giant Planet Candidates Around Two Metal-Polluted White Dwarf Stars, doi:10.48550/arXiv.2401.13153, http://arxiv.org/abs/2401.13153

Naeye R., 2017, Astronomy, 45, 24

Namur O., Collinet M., Charlier B., Grove T. L., Holtz F., McCammon C., 2016, Earth and Planetary Science Letters, 439, 117

Nguyen T. G., Cowan N. B., Banerjee A., Moores J. E., 2020, Monthly Notices of the Royal Astronomical Society, 499, 4605

Nguyen T. G., Cowan N. B., Dang L., 2024, Clouds on partial atmospheres of lava planets and where to find them, doi:10.48550/arXiv.2407.21111, http://arxiv.org/abs/2407.21111

Nittler L. R., Weider S. Z., 2019, Elements, 15, 33

Norris C. A., Wood B. J., 2017, Nature, 549, 507

Owens A., Yachmenev A., Thiel W., Tennyson J., Yurchenko S. N., 2017, \mnras, 471, 5025

Owens A., Conway E. K., Tennyson J., Yurchenko S. N., 2020, Monthly Notices of the Royal Astronomical Society, 495, 1927
Owens A., Tennyson J., Yurchenko S. N., 2021, \mnras, 502, 1128
Owens A., Mitrushchenkov A., Yurchenko S. N., Tennyson J., 2022, \mnras, 516, 3995
Palme H., O'Neill H. S. C., 2003, in , Vol. 2, Treatise on Geochemistry. Elsevier Ltd., p. 38
Panahi A., et al., 2022, Astronomy & Astrophysics, 663, A101
Parmentier V., et al., 2018, Astronomy & Astrophysics, 617, A110
Patrascu A. T., Yurchenko S. N., Tennyson J., 2015, Monthly Notices of the Royal Astronomical Society, 449, 3613
Paulose G., Barton E. J., Yurchenko S. N., Tennyson J., 2015, \mnras, 454, 1931
Pavlyuchko A. I., Yurchenko S. N., Tennyson J., 2015, \mnras, 452, 1702
Payacán I., Gutiérrez F., Bachmann O., Parada M., 2023, Geosphere, 19, 348
Picos D. G., et al., 2024, Astronomy & Astrophysics, 689, A212
Pierrehumbert R. T., Hammond M., 2019, Annual Review of Fluid Mechanics, 51, 275
Piette A. A. A., Gao P., Brugman K., Shahar A., Lichtenberg T., Miozzi F., Driscoll P., 2023, The Astrophysical Journal, 954, 29
Polyansky O. L., Kyuberis A. A., Zobov N. F., Tennyson J., Yurchenko S. N., Lodi L., 2018, \mnras, 480, 2597
Prajapat L., Jagoda P., Lodi L., Gorman M. N., Yurchenko S. N., Tennyson J., 2017, \mnras, 472, 3648
Putirka K. D., Rarick J. C., 2019, American Mineralogist, 104, 817
Putirka K. D., Xu S., 2021, Nature Communications, 12, 6168
Putirka K., Dorn C., Hinkel N., Unterborn C., 2021, arXiv:2108.08383 [astro-ph, physics:physics]
Qin Z., Bai T., Liu L., 2021, \jqsrt, 258, 107352
Qu Q., Yurchenko S. N., Tennyson J., 2021, \mnras, 504, 5768
Ram R. S., Brooke J. S. A., Western C. M., Bernath P. F., 2014, \jqsrt, 138, 107
Rasmussen K. C., et al., 2023, A Non-Detection of Iron in the First High-Resolution Emission Study of the Lava Planet 55 Cnc e, https://arxiv.org/abs/2308.10378v3
Regt S. d., et al., 2024, Astronomy & Astrophysics, 688, A116
Rivlin T., Lodi L., Yurchenko S. N., Tennyson J., Le Roy R. J., 2015, \mnras, 451, 634
Rogers L. A., Seager S., 2010, The Astrophysical Journal, 712, 974
Rothman L. S., et al., 2010, \jqsrt, 111, 2139
Ryabchikova T., Piskunov N., Kurucz R. L., Stempels H. C., Heiter U., Pakhomov Y., Barklem P. S., 2015, Physica Scripta, 90, 054005
Santos N. C., et al., 2017, Astronomy & Astrophysics, 608, A94

Schaefer L., Elkins-Tanton L. T., 2018, Philosophical Transactions of the Royal Society A: Mathematical, Physical and Engineering Sciences, 376, 20180109
Schaefer L., Fegley B., 2007, p. 22
Schaefer L., Fegley B., 2009, The Astrophysical Journal Letters, 703, L113
Schaefer L., Fegley Jr. B., 2004, Icarus, 169, 216
Schaefer L., Lodders K., Fegley B., 2012, The Astrophysical Journal, 755, 41
Schuster A., 1905, The Astrophysical Journal, 21, 197
Seidler F. L., Sossi P. A., Grimm S. L., 2024, Astronomy & Astrophysics, 691, A159
Semenov M., Clark N., Yurchenko S. N., Kim G.-S., Tennyson J., 2022, \mnras, 516, 1158
Smith G. R., Hunten D. M., 1990, Reviews of Geophysics, 28, 117
Smith A. M. S., et al., 2018, Monthly Notices of the Royal Astronomical Society, 474, 5523
Sossi P. A., Fegley B., 2018, Reviews in Mineralogy and Geochemistry, 84, 393
Sossi P. A., Tollan P. M., Badro J., Bower D. J., 2023, Earth and Planetary Science Letters, 601, 117894
Sousa-Silva C., Al-Refaie A. F., Tennyson J., Yurchenko S. N., 2015, \mnras, 446, 2337
Steenstra E. S., Berndt J., Klemme S., Fei Y., van Westrenen W., 2020, Earth and Planetary Science Letters, 538, 116222
Stock J. W., Kitzmann D., Patzer A. B. C., Sedlmayr E., 2018, Monthly Notices of the Royal Astronomical Society
Stock J. W., Kitzmann D., Patzer A. B. C., 2022, Monthly Notices of the Royal Astronomical Society, 517, 4070
Sudarsky D., Burrows A., Hubeny I., 2003, The Astrophysical Journal, 588, 1121
Swift D. C., et al., 2011, The Astrophysical Journal, 744, 59
Syme A.-M., McKemmish L. K., 2021, \mnras, 505, 4383
Underwood D. S., Tennyson J., Yurchenko S. N., Huang X., Schwenke D. W., Lee T. J., Clausen S., Fateev A., 2016a, \mnras, 459, 3890
Underwood D. S., Yurchenko S. N., Tennyson J., Al-Refaie A. F., Clausen S., Fateev A., 2016b, \mnras, 462, 4300
Upadhyay A., Conway E. K., Tennyson J., Yurchenko S. N., 2018, \mnras, 477, 1520
Vanderburg A., et al., 2020, Nature, 585, 363
Visscher C., Fegley J., 2013, The Astrophysical Journal, 767, L12
Wang H. S., Liu F., Ireland T. R., Brasser R., Yong D., Lineweaver C. H., 2019, Monthly Notices of the Royal Astronomical Society, 482, 2222
Wang H. S., Quanz S. P., Yong D., Liu F., Seidler F., Acuña L., Mojzsis S. J., 2022, arXiv:2204.09558 [astro-ph]
Weisberg M. K., Prinz M., Nehru C. E., 1990, Meteoritics, 25, 269
Weisberg M. K., Prinz M., Clayton R. N., Mayeda T. K., Sugiura N., Zashu S., Ebihara M., 2001, Meteoritics & Planetary Science, 36, 401

Western C. M., Carter-Blatchford L., Crozet P., Ross A. J., Morville J., Tokaryk D. W., 2018, \jqsrt, 219, 127
Whittaker E. A., et al., 2022, The Astronomical Journal, 164, 258
Wiik H. B., 1956, Geochimica et Cosmochimica Acta, 9, 279
Wildt R., 1939, The Astrophysical Journal, 90, 611
Wishart A. W., 1979, Monthly Notices of the Royal Astronomical Society, 187, 59P
Wittenmyer R. A., Tinney C. G., O'Toole S. J., Jones H. R. A., Butler R. P., Carter B. D., Bailey J., 2011a, The Astrophysical Journal, 727, 102
Wittenmyer R. A., Tinney C. G., Butler R. P., O'Toole S. J., Jones H. R. A., Carter B. D., Bailey J., Horner J., 2011b, The Astrophysical Journal, 738, 81
Wolf A. S., Jäggi N., Sossi P. A., Bower D. J., 2023, The Astrophysical Journal, 947, 64
Wolszczan A., 1994, Science, 264, 538
Wolszczan A., Frail D. A., 1992, Nature, 355, 145
Wong A., Yurchenko S. N., Bernath P., Müller H. S. P., McConkey S., Tennyson J., 2017, \mnras, 470, 882
Wright J. T., Marcy G. W., Howard A. W., Johnson J. A., Morton T. D., Fischer D. A., 2012, The Astrophysical Journal, 753, 160
Xu S., Bonsor A., 2021, arXiv:2108.08384 [astro-ph]
Yorke L., Yurchenko S. N., Lodi L., Tennyson J., 2014, \mnras, 445, 1383
Youngblood A., et al., 2016, The Astrophysical Journal, 824, 101
Yurchenko S. N., Blissett A., Asari U., Vasilios M., Hill C., Tennyson J., 2016, Monthly Notices of the Royal Astronomical Society, 456, 4524
Yurchenko S. N., Amundsen D. S., Tennyson J., Waldmann I. P., 2017, åp, 605, A95
Yurchenko S. N., Sinden F., Lodi L., Hill C., Gorman M. N., Tennyson J., 2018a, \mnras, 473, 5324
Yurchenko S. N., Bond W., Gorman M. N., Lodi L., McKemmish L. K., Nunn W., Shah R., Tennyson J., 2018b, \mnras, 478, 270
Yurchenko S. N., Williams H., Leyland P. C., Lodi L., Tennyson J., 2018c, \mnras, 479, 1401
Yurchenko S. N., Tennyson J., Miller S., Melnikov V. V., O'Donoghue J., Moore L., 2020, \mnras, 497, 2340
Yurchenko S. N., et al., 2022, Monthly Notices of the Royal Astronomical Society, 510, 903
Zhang J., Herzberg C., 1994, Journal of Geophysical Research: Solid Earth, 99, 17729
Zhang Y., et al., 2024a, The Astronomical Journal, 168, 246
Zhang M., et al., 2024b, The Astrophysical Journal Letters, 961, L44
Zieba S., et al., 2022, Astronomy & Astrophysics, 664, A79
Zieba S., et al., 2023, Nature, 620, 746

Zilinskas M., Miguel Y., Mollière P., Tsai S.-M., 2020, Monthly Notices of the Royal Astronomical Society, 494, 1490

Zilinskas M., Miguel Y., Lyu Y., Bax M., 2021, Monthly Notices of the Royal Astronomical Society, 500, 2197

Zilinskas M., van Buchem C. P. A., Miguel Y., Louca A., Lupu R., Zieba S., van Westrenen W., 2022, Astronomy & Astrophysics, 661, A126

Zilinskas M., Miguel Y., Buchem C. P. A. v., Snellen I. a. G., 2023, Astronomy & Astrophysics, 671, A138

de Maria G., Balducci G., Guido M., Piacente V., 1971, Lunar and Planetary Science Conference Proceedings, 2, 1367

van Buchem C. P. A., Miguel Y., Zilinskas M., van Westrenen W., 2023, Meteoritics & Planetary Science, 58, 1149

van Buchem C. P. A., Zilinskas M., Miguel Y., van Westrenen W., 2024, LavAtmos 2.0: Incorporating Volatiles Species in Vaporization Models, doi:10.48550/arXiv.2408.10863, http://arxiv.org/abs/2408.10863

English summary

In the past 30 years, exoplanet science has evolved exponentially. Since the discovery of the first exoplanets in the 1990s, we have progressed from mere detection to the physical and chemical characterization of these distant worlds through observations of their spectra. The niche of "hot rocky exoplanets" (HREs) is promising the potential of offering a unique window into rocky planet compositions atmosphere and interior compositions. Potentially providing valuable new information for developing our understanding of planetary formation, differentiation, and atmospheric evolution.

HREs are short-period rocky planets with dayside equilibrium temperatures in excess of 1500 K, high enough to melt rock and to support oceans of lava on their daysides, and potentially also their nightsides. These lava oceans create a direct interface between a planet's interior and atmosphere, allowing for the possibility of probing the interior composition of these planets remotely, by interpreting the spectral features shaped by chemical exchange between the melt and the atmosphere. Unlocking this potential demands comprehensive modelling approaches that account for the diverse physical and chemical processes operating within these planets. One these processes in particular is that of the vaporisation of the lava on the surface of a planet and how changing its composition affects the atmospheric composition of the planet and hence its spectral signature.

The primary goal of this thesis is to develop such models, enabling the simulation of vapor atmospheres above magma oceans under a wide range of physical and chemical conditions. To this end, I developed LavAtmos, an open-source code that calculates the equilibrium chemical composition of the vapor above a silicate melt at given temperatures, pressure, and melt composition. When we include this code within a broader modelling framework that includes atmospheric chemistry and radiative transfer calculations, it allows for the generation of self-consistent synthetic spectra for hot rocky exoplanets. The work presented in this thesis focuses on the development of LavAtmos, its implementation in the broader modelling framework, and the resulting implications for HRE science.

Chapter 2 of this thesis introduces the development and validation of the LavAtmos code in its first form, focusing on "dry" systems - those that exclude volatile-bearing species. LavAtmos calculates the chemical equilibrium between a melt and its vapor phase by combining thermodynamic data from MELTS with and internally consistent calculation of O_2 partial pressure, constrained by both the law of mass action and mass conservation. This approach allows us to determine the gas-phase abundances of over 50 chemical species, given an input silicate melt composition and thermodynamic state. LavAtmos is validated through comparison with the (relatively sparse) available experimental data as well as with other published vaporisation models.

In Chapter 3, we implement LavAtmos in the broader physical and chemical framework so as to enable us to explore how variations in bulk composition

of the magma ocean influence the observable emission spectra of HREs. This is a key question to answer for interpreting data gathered using the recently launched JWST, which has, and will continue to, target many of these worlds in its observation cycles. This study focuses specifically on how the abundances of major oxides in the melt - such as TiO_2, SiO_2, Na_2O, and K_2O - affect atmospheric chemistry and radiative properties. The modelling framework includes an equilibrium gas-chemistry code and a radiative transfer code to self-consistently compute atmospheric temperature-pressure profiles and emission spectra.

We find that although many melt composition changes have relatively minor spectral consequences, a few compositions stand out. High TiO_2 content in the melt increases atmospheric TiO abundances, which, due to its strong short-wave opacity, has a strong influence on the surface temperature and the emission spectra of HREs. This creates a degeneracy with heat-redistribution efficiency, which may potentially be broken by observing the optical TiO emission feature. SiO_2 also exhibits noticeable effects on the atmospheric spectrum, particularly in enhancing the SiO and SiO_2 features. The alkali oxides (Na_2O, K_2O) primarily influence surface pressure and secondary gas-phase abundances but have less direct spectral impact.

While Chapters 2 and 3 focus on volatile-free ("dry") modelling, Chapter 4 acknowledges a limitation of that approach. Recent observations and theoretical studies suggest that HREs, despite their high temperatures, may be able to host volatile-bearing atmospheres containing elements such as hydrogen, carbon, nitrogen, sulphur, and phosphorus. To address this, we developed LavAtmos 2, and upgraded version of the original code that includes volatiles species in the melt-vapor equilibrium calculations. Again using the dual constraints of mass action and mass conservation to constrain the O_2 partial pressure, we calculate the composition of the vapor above a melt in a system containing both melt species and volatile elements. Incorporating an existing gas-chemical equilibrium code named FastChem allowed us to expand the number of considered gas phases to 523.

Using this model, we investigated idealized atmospheres containing only a single volatile element, more realistic "complex" volatile atmospheres containing all five tested volatile elements, and two different potential atmospheric volatile compositions for 55-Cnc e. The inclusion of volatiles was found to significantly increase the partial pressure of major gas species such as SiO, SiO_2, Na, and K when compared to dry cases. It also lead to a much higher abundances of Oxygen in the atmosphere, which in turn enhanced the abundance of key volatile species such as CO_2 and H_2O. These changes have direct implications for observable spectra and could serve as diagnostic signatures for the presence of volatiles and potentially even surface lava oceans.

In the final chapter of this thesis, we treat the radiative consequences of including volatile species - particularly hydrogen - in HRE atmospheres. One of the most important opacity sources in high-temperature, hydrogen-bearing

atmospheres is the H^- ion. Known to dominate the continuum opacity in stars and hot gas giants, H^- can significantly reshape the thermal emission spectrum of a planet if free electrons are abundant. Through the application of the modelling framework from Chapter 4, we investigated the impact of H^- opacity in HREs with varying atmospheric H abundances.

We show that even at H volume mixing ratios as low as 10^{-5}, planets with surface temperatures above 2500 K exhibit strong H^- continuum absorption, sufficient to dominate over molecular features such as those from H_2O and SiO. This happens thanks to the ionisation of alkali metals at high temperatures which supplies the free electrons needed for H^- absorption to occur. The result is a suppression of spectral lines and a smoother, more blackbody-like emission spectrum. This effect makes atmospheric retrieval more difficult, as it weakens or erases the distinct molecular features typically used for compositional analysis. However, the presence of a strong H^- continuum itself may be a clue: its strength implies a high abundance of free electrons, which in turn may point to the existence of a hot, molten, metal-rich surface interacting with a hydrogen-bearing atmosphere.

In summary, this thesis provides a comprehensive framework for understanding the chemical and radiative behaviour of hot rocky exoplanets, from the fundamental processes of lava vaporization to the observational signatures potentially detectable with modern space telescopes. By developing and applying LavAtmos, both in dry and volatile-including atmosphere, this work offers new insights into how surface and atmospheric compositions are linked, and how these links manifest in planetary spectra. These models can be used for interpreting forthcoming data from JWST and future missions, and offer a roadmap for inferring interior properties of rocky exoplanets through remote atmospheric characterization. As observations continue to improve, the tools and findings developed here will hopefully be off use in unravelling the complex processes that shape some of the most extreme terrestrial planets in the galaxy.

Nederlandse samenvatting

In de afgelopen 30 jaar is de exoplaneetwetenschap exponentieel gegroeid. Sinds de ontdekking van de eerste exoplaneten in de jaren '90 van de vorige eeuw, zijn we geëvolueerd van louter detectie naar het karateriseren van de fysische en chemische eigenschappen van deze verre werelden via observaties van hun spectra. Een veelbelovende niche binnen dit veld is die van "hete rotsachtige exoplaneten"(HREs), die mogelijk een unieke inkijk kunnen bieden op de inwendige samenstelling van rotsachtige planeten. Dankzij dit gegeven, kunnen deze planeten mogelijk waardevolle nieuwe informatie verschaffen over planeetvorming, interne differentiatie en de evolutie van atmosferen.

HREs zijn planeten met korte omlooptijden en een evenwichtstemperatuur op de dagzijde van meer dan 1500 K - warm genoeg voor het smelten van steen en het vormen van lava-oceanen, niet alleen op de dagzijde maar mogelijk ook op de nachtzijde. Deze lava-oceanen vormen een directe verbinding tussen het inwendige en de atmosfeer van de planeet, waardoor het in principe mogelijk wordt om de inwendige samenstelling van de planeet op afstand te achterhalen door de spectrale kenmerken van de atmosfeer te interpreteren die gevormd worden door chemische uitwisseling met het gesmolten oppervlak. Om dit potentieel te benutten zijn uitgebreide modelleringsbenaderingen nodig die de diverse fysische en chemische processen die binnen deze planeten plaatsvinden in detail nabootsen. Eén van die processen is de verdamping van lava aan het oppervlak en de invloed van veranderingen in de lavasamenstelling op de samenstelling van de atmosfeer, en dus ook op het spectrum van de planeet.

Het hoofddoel van dit proefschrift is het ontwikkelen van modellen die dit proces nabootsen om de dampatmosferen boven magma-ocean en onder verschillende fysisch-chemische omstandigheden te simuleren. Dit heefd geleid tot de ontwikkeling van LavAtmos, een open-source code die de chemische evenwichtssamenstelling van de damp boven een silicaatsmelt berekend bij een gegeven temperatuur, druk en samenstelling. Het combineren van deze code met een reeks andere codes die de atmosferische chemie en de emissie van straling berekenen, stelt ons in staat om zelf-consistente synthetische specra van hete rotsachtige planeten te genereren. Het werk in dit proefschrift richt zich op de ontwikkeling van LavAtmos, de implementatie ervan in het bredere modelleringskader, en de implicaties daarvan voor HRE onderzoek.

Hoofdstuk 2 beschrijft de intwikkeling en validatie van de eerste versie van LavAtmos, met de focus op "droge"systemen - dat wil zeggen systemen waarin gesmolten stenen verdampen zonder vluchtige elementen. LavAtmos berekent het chemisch evenwicht tussen een smelt en de dampkringfase door thermodynamische gegevens van de code MELTS te combineren met een intern consistente berekening van de partiële zuurstofdruk (P_{O2}), met de wet van massawerking en massabehoud als randvoorwaarden. Deze aanpak stelt ons in staat om op basis van een invoersamenstelling van de smelt en de thermodynamische toestand de gasfase-abundantie van meer dan 50 chemische soorten te bepalen. LavAtmos wordt gevalideerd door output te vergelijken met de (beperkte)

beschikbare experimentele gegevens en andere gepubliceerde verdampingsmodellen.

In Hoofdstuk 3 wordt LavAtmos geïntegreerd in een breder fysisch-chemisch modelleringskader, waarmee we kunnen onderzoeken hoe variaties in de bulksamenstelling van de magma-oceaan de waarneembare emissiespectra van HREs beïnvloeden. Dit is een cruciale stap voor de interpretatie van gegevens die verzameld worden met de recent gelanceerde James Webb Space Telescope (JWST), die actief bezig is met het observeren van deze werelden. In dit onderzoek kijken we specifiek hoe de concentraties van belangrijke oxiden in de smelt - zoals TiO_2, SiO_2, Na_2O, en K_2O - invloed hebben op de atmosferische chemie en stralingseigenschappen. Het modelkader omvat een gaschemisch evenwichtsmodel en een stralingstransportcode die gezamelijk de temperatuurdrukprofielen en emissiespectra van de atmosfeer berekenen.

We vinden dat veel veranderingen in de smeltsamenstelling slechts beperkte spectrale gevolgen hebben met enkele opvallende uitzonderingen. Een hoog TiO_2-gehalte in de smelt verhoogt de TiO-concentratie in de atmosfeer, wat vanwege zijn sterke kortegolfopaciteit grote invloed heeft op zowel de oppervlaktetemperatuur als het emissiespectrum. Dit creëert een degeneratie met de efficiëntie van warmtetransport, die mogelijk doorbroken kan worden door het waarnemen van een optisch TiO-emissiekenmerk. Een toename van het SiO_2 gehalte in de lava laat ook duidelijk effecten zien, vooral door het versterken van de SiO- en SiO_2-spectrale lijnen. Concentraties van de alkalioxiden (Na_2O en K_2O) beïnvloeden voornamelijke de oppervlaktedruk en secundaire gasfasen, maar hebben minder directe spectrale invloed.

Terwijl hoofdstuk 2 en 3 zich richten op modellering zonder vluchtige elementen, erkent Hoofdstuk 4 een belangrijke beperking van deze aanpak. Recente waarnemingen en theoretisch onderzoek wijzen er op dat HREs, ondanks hun hoge temperaturen, atmosferen kunnen bezitten die vluchtige elementen bevatten zoals waterstof, koolstof, stikstof, zwavel, en fosfor. Om hierop in te spelen, hebben we LavAtmos 2 ontwikkeld - een verbeterde versie van de oorspronkelijke code waarin deze vluchtige componenten worden meegenomen in de damp-smelt-evenwichtsberekening. Wederom gebruiken we de duale randvoorwaarden van massawerking en massabehoud om de partiële zuurstofdruk (P_{O2}) te bepalen in systemen die zowel smeltspecies als vluchtige elementen bevatten. Dankzij de integratie van de bestaande chemisch-evenwichtscode FastChem konden we het aantal beschouwde gasfasen uitbreiden tot 523.

Met dit uitgebreide model onderzochten we geïdealiseerde atmosferen met één enkele vluchtig element, meer realistische complexe atmosferen met alle vijf vluchtige elementen, en twee mogelijke atmosferische samenstellingen voor 55 Cancri e. We concludeerden dat het meenemen van vluchtige elementen in onze berekeningen leidt tot een aanzienlijke verhoging van de partiële drukken van belangrijke gassoorten zoals SiO, SiO_2, Na, en K ten opzichte van droge modellen. Ook neemt de zuurstofconcentratie in de atmosfeer sterk toe, wat op zijn beurt de abundantie verhoogt van belangrijke moleculen zoals CO_2 en H_2O.

Deze veranderingen hebben directe gevolgen voor het waargenomen spectrum en kunnen dienen als diagnostische aanwijzingen voor de aanwezigheid van vluchtige stoffen en mogelijk zelfs een lava-ocean aan het oppervlak.

In het laatste hoofdstuk van dit proefschrift behandelen we de stralingstechnische gevolgen van het opnemen van vluchtige elementen - met name waterstof - in de atmosferen van HREs. Eén van de belangrijkste bronnen van opaciteit in hete, waterstofrijke atmosferen is het H^--ion. Dit ion domineert de continuümopaciteit in sterren en hete gasreuzen, en kan ook het thermische emissiespectrum van planeten ingrijpend veranderen wanneer vrije elektronen in voldoende mate aanwezig zijn. Met behulp van het modelkader uit Hoofstuk 4, onderzochten we het effect van H^--opaciteit in HREs bij verschillende atmosferische waterstofconcentraties.

We tonen aan dat zelfs bij waterstofvolumeverhoudingen van slechts 10^{-5} planeten met oppervlaktetemperaturen boven 2500 K sterke H^--continuümabsorptie vertonen. Dit is voldoende om de spectrale kenmerken van moleculen zoals H_2O en SiO te onderdrukken. Dit gebeurt doordat alkalimetalen bij hoge temperaturen ioniseren en zo de vrije elektronen leveren die nodig zijn voor H^--vorming. Het gevolg is een spectrum met verzwakte of zelfs afwezige moleculaire lijnen, en een meer blackbody-achtig emissieprofiel. Deze verzwakking maakt het moeilijker om de samenstelling van de atmosfeer spectroscopisch te achterhalen. Toch kan een sterk H^--continuüm zelf als aanwijzing dienen: de aanwezigheid ervan wijst op een overvloed aan vrije elektronen, wat op zijn beurt kan wijzen op een heet, gesmolten, metaalrijk oppervlak dat in contact staat met een waterstofhoudende atmosfeer.

Samenvattend biedt dit proefschrift een uitgebreid kader voor het begrijpen van het chemische en stralingstechnische gedrag van hete rotsachtige exoplaneten, van de fundamentele processen van lava-verdamping tot de observationele kenmerken die mogelijk detecteerbaar zijn met moderne ruimtetelescopen. Door de ontwikkeling en toepassing van LavAtmos — zowel voor droge atmosferen als voor atmosferen die vluchtige elementen bevattende — biedt dit werk nieuwe inzichten in hoe de samenstelling van het oppervlak en de atmosfeer met elkaar verbonden zijn, en hoe deze verbindingen zich uiten in het planetaire emissie spectrum. Deze modellen kunnen worden ingezet voor de interpretatie van aankomende gegevens van JWST en toekomstige missies, en bieden een routekaart om de inwendige eigenschappen van rotsachtige exoplaneten af te leiden via atmosferische karakterisering op afstand. Naarmate observaties steeds geavanceerder worden, zullen de hier ontwikkelde methodes en inzichten hopelijk van nut zijn bij het ontrafelen van de complexe processen die enkele van de meest extreme rotsachtige planeten in ons sterrenstelsel vormgeven.

Publications

First author:

1. **C.P.A. van Buchem**, M. Zilinskas, L.J. Janssen, Y. Miguel, and W. van Westrenen *The effect of H^- continuum on Lava Planet Emission Spectra*, to be submitted

2. **C.P.A. van Buchem**, R. Buddhacharya, M. Zilinskas, Y. Miguel, W. van Westrenen, and S. Zieba *Sensitivity of Dry Lava Planet Atmospheric Emission Spectra to Changes in Lava Compositions*, Monthly Notices of the Royal Astronomical Society, In Rev.

3. **C.P.A. van Buchem**, M. Zilinskas, Y. Miguel, and W. van Westrenen, *LavAtmos 2.0: Incorporating volatile species in vaporisation models*, Astronomy & Astrophysics, Vol 695, A157 (2025)

4. **C.P.A. van Buchem**, Y. Miguel, M. Zilinskas, and W. van Westrenen, *LavAtmos: An open-source chemical equilibrium vaporization code for lava worlds*, Meteoritics & Planetary Science, 58(8):1149-1161, (2023)

Contributing author:

1. M. Zilinskas, **C.P.A. van Buchem**, S. Zieba, Y. Miguel, E. Sandford, R. Hu, J.A. Patel, A. Bello-Arufe, L.J. Janssen, S.-M. Tsai, D. Dragomir, and M. Zhang, *Characterising the atmosphere of 55 Cancri e: 1D forward model grid for current and future JWST observations*, Astronomy & Astrophysics, Vol 697, A34 (2025)

2. H.L.F. Huybrighs, **C.P.A. van Buchem**, A. Blöcker, V. Dols, C.F. Bowers, C.M. Jackman, *Energetic Proton Losses Reveal Io's Extended and Longitudinally Asymmetrical Atmosphere*, Journal of Geophysical Research: Space Physics, Vol 129, Issue 7 (2024)

3. R. Hu, A. Bello-Arufe, M. Zhang, K. Paragas, M. Zilinskas, **C.P.A. van Buchem**, M. Bess, J. Patel, Y. Ito, M. Damiano, et al., *A secondary atmosphehre on the rocky exoplanet 55 cancri e*, Nature, 630, 609-612 (2024)

4. H.L.F. Huybrighs, A. Blöcker, E. Roussos, **C.P.A. van Buchem**, Y. Futaana, M.K.G. Holmberg, C. Goetz, O. Witasse, *Europa's Perturbed Fields and Induced Dipole Affect Energetic Proton Depletions During Distant Alfvén Wing Flybys*, Journal of Geophysical Research: Space Physics, Vol 128, Issue 9 (2023)

5. K.C. Rasmussen, M.H. Currie, C. Hagee, **C.P.A. van Buchem**, M. Malik, A.B. Savel, M. Brogi, E. Rauscher, V. Meadows, M. Mansfield, *A Nondetection of Iron in the First High-resolution Emission Study of the Lava Planet 55 Cnc e*, The Astronomical Journal, 166, 155, (2023)

6. M. Zilinskas, Y. Miguel, **C.P.A. van Buchem**, and I.A.G. Snellen, *Observability of silicates in volatile atmospheres of super-Earths and sub-Neptunes: Exploring the edge of the evaporation desert*, Astronomy & Astrophysics, Vol 671, A138 (2023)

7. M. Zilinskas, **C.P.A. van Buchem**, Y. Miguel, A. Louca, R. Lupu, S. Zieba, and W. van Westrenen *Observability of evaporating lava worlds*, Astronomy & Astrophysics, Vol. 661, A126 (2022)

Curriculum Vitae

I was born on a hot summer day (or so I am told) in Paris, on the 5th of July 1995. Although I started out with my parents all to myself, I soon gained not one, not two, but three younger brothers. Each welcome addition to the family brought a move to a house progressively farther from the French capital, into the countryside of Les Yvelines, eventually ending up in the town of Thoiry. These early years are filled with memories of running through the fields with my brothers and our dog, watching TV by the fireplace with our cats on our laps, and going on adventurous bike rides with my friends. It was also in these years that my interest for astronomy first reared its head.

The first thing to trigger my fascination with space was the hand-drawn images from the children's book "L'imagery de l'espace". I then read through everything the local public school library had to offer on the subject, finally convincing my parents to subscribe to a weekly space magazine, the bundled collection of which I still have in my bookcase today. In my 11th summer, my parents decided to take it a step further and show me the true scale of a planet, so we went to live on (what felt like) the other side of the world: Doha, Qatar.

We were enrolled at the American School of Doha, giving me the surreal experience of being in a classroom where I did not understand the language being spoken (mentally preparing me for future university calculus courses). Luckily this only lasted a little while, and we adjusted well to expat life. It was there that I got my first taste of "scientific" experimentation by taking part in the 5th grade science fair with two classmates - and taking home first place. It was also in Qatar that my mind was truly opened to music, discovering that there was more than Sean Paul and French rap. I picked up the guitar and quickly became convinced my goal in life was to become a rock star.

Eventually, we moved back to Europe, settling in Hellerup, Denmark, a town on the outskirts of Copenhagen. Coming from the very limited freedom of compound life in Qatar, being free to roam through Copenhagen was very well timed for my 15 year old self. It was during these years that I went through a lot of personal development (as I guess most teenagers do). I was also becoming more aware of the fact that I had had a very privileged childhood, and thought that I should capitalise on that by doing something in which I felt I could really contribute something to the world. At the time, I was convinced that space travel was the solution to all of humanity's problems. This, coupled with my ever-lingering fascination with space, led me to decide that I wanted to study astronomy. And so, after finishing high school in the summer of 2014, I moved to Leiden.

I only later found out that Leiden is a very good place to study astronomy. My first reason for moving there was the convenience of starting my stay in the Netherlands by moving in with my aunt and uncle for the first half year. The three years of my bachelor's were mainly characterised by the precarious balancing act of spending almost all of my free time at my student society (Quintus) while still doing enough work to pass all my courses. Somehow I

managed and after three years I had my bachelor's diploma in the pocket, although my extracurricular activities might have been reflected in my grade point average. It was these same extracurricular activities though, that led to me being asked to be the head of the full-time board of my student society for a year, which I accepted. This kicked off a very tumultuous year that tested me in many different ways, but also gave me some of the most memorable moments of my life - and of course, led to me meeting Marleen.

The next goal was to get my master's degree. After a few months of readjusting to going back to lectures and re-learning how to use my brain, I realised that if I wanted to continue in astronomy, I had to put a lot more time and effort into my masters than I had during my bachelor's. The extra work paid off and for my second research project I was selected to do a project at ESA/ESTEC. Walking past actual spaceships while on my way to my office was a dream come true (even if my office was located in the break room). Sadly however, the in-office experience was cut short by the pandemic.

Luckily, the interview rounds for a PhD position at Leiden had already taken place when (to quote one of the professors at the time) COVID-19 was still a "far-off Chinese disease", and I was accepted for the PhD position that led to the writing of this thesis. Although it was tough to start these years during the lockdowns, I was lucky enough to have many good friends and family living nearby. Once the restrictions were lifted and conferences started up again, a whole new world opened up for me - finally making me feel like I was truly part of a scientific community. I am very grateful for the large number of places that I was able to visit and the amazing people I was able to meet from all over the world. All in all, my PhD was a very positive experience. However, towards the end I found myself to be increasingly distracted by many of the more acute issues that our society is facing today. For this reason, for the moment being, I have decided to leave the academic world for a job as a scientific software engineer in the space industry - still keeping to my initial ideals, but now more practically oriented.

I am ever grateful for my life thus far and I look forward to seeing what the future holds.

Acknowledgements

As with most things in life, what on the surface appears to be the result of a single person's efforts, would never have been possible without the support of the communities surrounding that person. Of course, this project would never have existed in the first place if it weren't for Yamila and Wim.

Yamila, I was very lucky to have you as a supervisor. I don't think I've ever met someone who is as committed to putting people first as you are. First you take care of the people in your team, then you take care of the science. By taking such good care of the social and mental well-being of your students and postdocs you create a very safe and scientifically productive environment. Any time that I felt stuck or demotivated about my work, having a meeting with you always got me out of my rut. Thank you so much for all the support and trust you've given me over these years.

Wim, although the pandemic meant we couldn't see each other as much as originally planned, you were always as supportive as possible from a distance. Always making the time whenever needed to help fill the gaps in my geology knowledge and giving fast, highly detailed feedback on all my writing. Even during times when you had a lot of other things on your mind as well. Thank you.

The wholesome atmosphere in our research group was in a large part also thanks to all my scientific siblings. Mantas, my scientific big brother, you've taught me more than you probably realise, both on a scientific and a personal level. Amy, my scientific twin, it has been a joy to have been able to share the whole PhD journey alongside each other. Of course, we cannot forget our Austrian cousin Sebastian who was always able to show us the way to the nearest karaoke bar and free drinks at whichever conference we were attending. Rojita, as the only master student that I supervised, I don't think I could have asked for a better student. Your view of the world is inspiring and I hope that you never lose your optimism and sense of wonder. Then, of course, there is everyone who strengthened our group later on as well: Emily, Esther, Keren, Leonie, Louis, Solene, and Vanesa. I'm glad to have met you guys and I hope that you pass on the good vibes of our group to whoever joins in the future.

In the 9 years and 6 months that I've either studied or worked at the observatory, I have met a huge number of people who have made my time better. Aaron, Alessia, Andrew, Anniek, Anthony, Aurora, Ben, Billy, Chloe, Colin, Christian, Dag, Dario, Dilovan, Elia, Elina, Frits, Gijs, Hans, Ignas, Ivana, Jeger, Jeroen, Joe, Josh, Joshiwa, Jurjen, Katia, Kevin, Kiki, Kutay, Lucie, Lukas, Luuk, Maite, Mariana, Martijn, Martje, Marta, Matt, Michiel, Naadiyah, Naor, Nico, Osmar, Orin, Piyush, Pranjal, Rico, Richelle, Rob, Roi, Roland, Sam, Saeid, Shun-Sheng, Sid, Silvia, Stefano, Syl, Thijs, Thomas, Timo, Veronica, Victorine, Willeke, William, Yapeng, Yuan, Yuze, Zephyr, Zorry... and I am bound to forget some people but please know that I will never forget the many shared lunch breaks, the bizarre topics discussed during endless coffee breaks, the making and/or destroying of puzzles, taking part in

suicidal eating challenges, racing each other in office chairs, seeing who can climb up all of the Huygens stairs the fastest, the boozy borrels, the many defense parties, board game nights, PhD activities, pandemic zoom hangouts, Sinterklaas, the barbecues, PhSkii, and making music. It's honestly impressive that we had any time left for work at all. The STRW is a truly unique place and even though many people may come and go, I hope that the welcoming atmosphere always remains.

I'm convinced that I would never have made it as far as I did in astronomy without the "Len is een Bierspons" boys. Auke, Couzy, Erik, Jelle, Joey, Jonah, and Len — it was often the fear of disappointing you guys that motivated me to drag myself to classes even on mornings after particularly rowdy nights. I've truly enjoyed eating lunch together basically every day for years, our lengthy study sessions interrupted by a few games of Hearthstone, and eventually also our hiking trips. I'm grateful to have you as a friend group.

Then, of course, there are all my friends from outside of astronomy. Max, from the shared Data Science bachelor minor all the way up to finishing our PhDs, we were always able to level with each other about whatever we had on our minds. As we've said many times before, talking to each other is like talking to a different version of yourself. Special shout-out to the boys from the Moddermanstraat 59 for motivating each other to keep working throughout the pandemic lockdowns. Thank you, Tim and Just, for being my steady home base during our first 5 years in Leiden. DV14: Ik heb jullie nooit gemogen en ook nooit op jullie gestemd. Lief Bestuur, BDF (you guys are insane), the Wrath and Glory crew, Hot Rod, and all my other friends — you've made it possible for me to keep a healthy perspective on my life even during the rougher moments.

Of the many privileges I have in my life, a big one is how closely knit my family is. Lieve grootmama en grootpapa, jullie enthousiasme voor alles wat ik ondernam in de sterrenkunde was erg motiverend. Ik ben dankbaar dat jullie nog de eerste jaren van m'n PhD mee hebben kunnen maken. Mark en Claartje, jullie ontvangst van mij in Leiden en het feit dat ik bij jullie altijd een soort tweede ouderlijk huis erbij had, waardeer ik enorm. Ik heb helaas niet genoeg woorden om ook alle neven en nichten te bedanken, maar jullie weten hoe erg ik jullie waardeer.

Hugo, Reinier, and Thibault — I've been very happy to see you all move to the Netherlands over the past years and to witness you all finding your own way in the world. Love you guys. Mom and Dad, I very literally would not have been able to do any of this if it weren't for you two. But besides the literal sense, I think the confidence you've always had in me and your unconditional love have played a very large role in getting me where I am today.

Marleen, thank you for being my personal cheerleader, partner in crime, and best friend. You never cease to impress me. I love you.

“Tout est vrai, et rien n’est vrai!”

"Everything is true, and nothing is true!”

– *L’Étranger*, Albert Camus